LIFETIME, CRITICAL NUCLEUS SIZE, AND LAPLACE PRESSURE OF INDIVIDUAL ELECTROCHEMICALLY GENERATED NANOBUBBLES

by

Sean R. German

A dissertation submitted to the faculty of
The University of Utah
in partial fulfillment of the requirements for the degree of

Doctor of Philosophy

Department of Chemistry

The University of Utah

August 2017

The University of Utah Graduate School

STATEMENT OF DISSERTATION APPROVAL

The dissertation of **Sean R. German**

has been approved by the following supervisory committee members:

Henry S. White	, Chair	**Feb. 27, 2017** Date Approved
Shelley D. Minteer	, Member	**Feb. 27, 2017** Date Approved
Joel M. Harris	, Member	**Feb. 27, 2017** Date Approved
Valeria Molinero	, Member	**Feb. 27, 2017** Date Approved
Mikhail Skliar	, Member	**Feb. 27, 2017** Date Approved

and by **Cynthia J. Burrows** , Chair/Dean of

the Department/College/School of **Chemistry**

and by David B. Kieda, Dean of The Graduate School.

ABSTRACT

This dissertation presents experimental and computational studies of individual nanobubbles electrochemically generated at platinum nanoelectrodes. Chapter 1 provides an overview of the physics governing bubble dynamics and a brief summary of the literature regarding nanobubbles.

Chapter 2 describes a fast scan voltammetric method for measurement of nanobubble dissolution rates. After a nanobubble is nucleated from gas generated via an electrode reaction, the electrode potential is rapidly stepped to a value where the bubble is unstable and begins to dissolve. The electrode potential is immediately scanned back to values where the bubble was initially stable. Depending on the rate of this second voltammetric scan, the initial bubble may or may not have time to dissolve. The fastest scan rate at which the bubble dissolves is used to determine the bubble's lifetime. The results indicate that dissolution of a H_2 or N_2 nanobubble is, in part, limited by the transfer of molecules across the gas/water interface.

Chapter 3 presents electrochemical measurements of the dissolved gas concentration, at the instant prior to nucleation of a nanobubble of H_2, N_2, or O_2 at a Pt nanodisk electrode. The results are analyzed using classical thermodynamic relationships to provide an estimate of the size of the critical gas nucleus that grows into a stable bubble. This critical nucleus size is independent of the radius of the Pt nanodisk employed and

weakly dependent on the nature of the gas.

Chapter 4 reports electrochemical measurements of Laplace pressures within single H_2 bubbles between 7 and 200 nm radius (corresponding, respectively, to between 200 and 7 atmospheres). The current, associated with H_2 gas generation, supporting a steady-state nanobubble is modulated by application of external pressure. The slope of the current-pressure response allows extrapolation of the bubble's curvature-dependent internal pressure. The results demonstrate a linear relationship between a bubble's Laplace pressure and its reciprocal radius, verifying the classical thermodynamic description of H_2 nanobubbles as small as ~10 nm.

Chapter 5 summarizes these results and places them in the context of current research. Future directions for further studies are suggested.

TABLE OF CONTENTS

LIST OF FIGURES

Figures Page

ACKNOWLEDGEMENTS

I would like to thank all the people who have contributed in different ways to the research described in this dissertation. First, I thank my academic advisor, Henry White, for allowing me intellectual freedom in my work, engaging me in new ideas, and demanding a high quality of work. I am also grateful for my committee members, Shelley Minteer, Joel Harris, Valeria Molinero, and Mikhail Skliar – their genuine interest in my work and willingness to give their time is admirable.

Every result in this dissertation was accomplished with the help of fellow group members and collaborators. Thank you to Martin Edwards without whose keen scientific insight I would have spent even more time confused, to Qianjin Chen who helped me hit the ground running when I first arrived, to Long Luo for beginning this avenue of nanobubble research, and to Kim McKelvey, Hang Ren, Yulun Zhang, Cherie Tan, Donald Robinson, Cameron Cheyne, and Dolan Pritchett for bringing a bit of light to the basement.

I must give credit to friends made through Revalesio for helping turn me into a scientist: to Tony Mega for being a mentor and counterbalance; to Richard Watson for putting his confidence in me; to Tony Wood for encouraging creativity.

And for everything else that is good in my life, I thank Emily, Eloise, and Henry. Because they always understood.

CHAPTER 1

INTRODUCTION

1.1 The Physics of Bubbles

1.1.1 Laplace pressure

A child with a glass of milk and a straw knows what it takes to make a bubble. And yet, despite being an everyday experience, bubbles continue to pose new scientific questions. As relatively simple systems with ideal composition and geometry, bubbles serve as a test bed for our understanding of thermodynamics and surface forces. The blowing of a bubble through a straw is an experiment that occupied Erwin Schrödinger during his first foray into science.[1] The distension of the liquid surface requires a pressure, an input of energy, to overcome the liquid's cohesive forces and create more surface area. This energy cost is the surface tension of the liquid and is the reason small bubbles take on a spherical shape to minimize surface area. Surface tension is essentially a measure of the preference of liquid molecules to bond with one another completely surrounded in the bulk as opposed to residing at the air/liquid interface with, on average, half the number of cohesive bonds. For bubbles, another avenue to reduce surface area is to shrink and squeeze the gas within. Compression of the entrapped gas will find an equilibrium where the pressure within the bubble presses back equally against the force of surface tension. The

increased pressure within a bubble, P_{bubble}, in comparison with its surroundings, $P_{external}$, is described by the 200-year-old Young-Laplace equation which, for a sphere, is given by,

$$P_{bubble} - P_{external} = 2\gamma/r \quad (1.1)$$

where γ is the surface tension and r is the bubble's radius. The inverse dependence on r means that very small bubbles are expected to have surprisingly high internal pressures, e.g., the air within a 10 nanometer bubble in pure water should compressed to ~150 atmospheres.

Schrödinger was the first to work out the correct formulation still commonly used for calculating surface tension via the maximum bubble pressure.[1] Figure 1.1 illustrates the method in which a bubble is inflated into a liquid through capillary of known radius while a sensor records the pressure within it. Initially, in part a, the curvature of the air/liquid interface corresponds to a very large radius and the pressure is low. As the bubble inflates, the interface becomes more curved and more pressure is required to inflate the bubble further. The pressure sensor will record a maximum when the bubble is a hemisphere with radius equal to that of the capillary, R_c, indicated in part b of Figure 1.1. With the pressure and radius of the bubble known, the surface tension can be calculated. Chapter 4 of this dissertation presents electrochemical measurements of the internal pressure of nanobubbles allowing calculation of their surface tension. It has been predicted for very high curvature interfaces (whose radius is no longer exceedingly large in comparison to the thickness of the interfacial density gradient from gas to liquid) that the surface tension should be different from the macroscopic value due to structural effects on water's hydrogen bonding network. The length scale at which this effect becomes important is under debate, although this presented work demonstrates surface tension to remain constant for bubbles as small

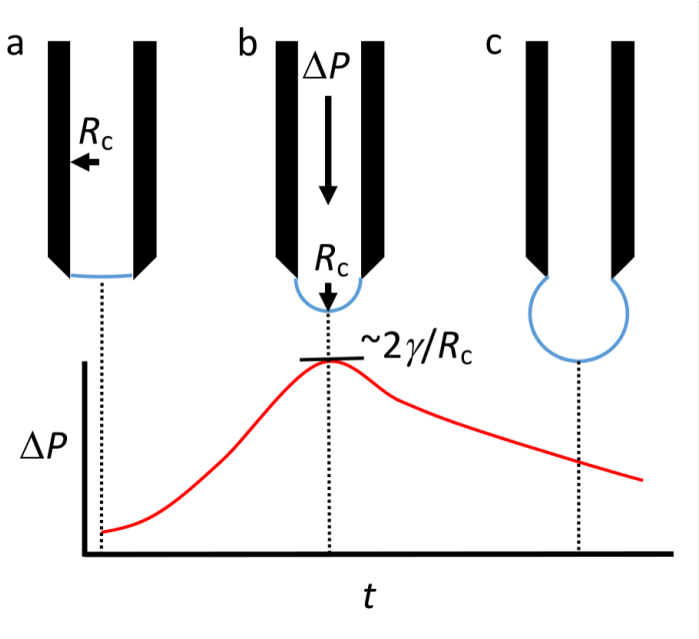

Figure 1.1. Illustration of the maximum bubble pressure method for measurement of surface tension. With no pressure applied in (a), the air/liquid interface indicated in blue has very low curvature. As air is forced through the capillary, the radius of curvature of the air/liquid interface decreases and the pressure required to inflate the bubble reaches a maximum at (b) where the radius of the bubble is equal to that of the capillary, R_c.

as ~10 nm radius.

1.1.2 Bubble lifetimes

The high-pressure gas is not statically trapped within the bubble, because the air/liquid interface is permeable. The gas within is constantly colliding with the surface and is free to exchange from the gas phase into the solution and vice versa. For any given gas pressure, P_{gas}, there is an equilibrium dissolved gas concentration, C_{eq}, approximated by Henry's Law,

$$P_{gas} K_H = C_{eq} \tag{1.2}$$

where K_H is Henry's constant, an empirically measured value for every temperature, gas type, and solvent, implying a linear relationship between gas solubility and pressure. Equilibrium, in the case of a glass of water sitting open to atmosphere, is a dynamic process meaning the dissolved gas concentration is constant because an equal amount of gas is exiting solution across the interface as is entering.

For a bubble in that glass of water, though, there can never be a stable equilibrium considering the above equations. The bubble's internal pressure will always be higher than the ambient pressure according to equation 1.1, resulting in a higher gas solubility in the liquid immediately surrounding the bubble according to equation 1.2. Consequently, the gas from within the bubble will dissolve into solution, driving a higher concentration at the bubble interface than the bulk solution. The dissolved gas will then diffuse away down the concentration gradient to be replaced at the interface by more gas from the bubble until it is emptied. This dissolution process is only limited by diffusion and considers the gas transfer across the interface to be infinitely fast, always maintaining the equilibrium

concentration at the bubble surface according to Henry's Law. For large bubbles, dissolution occurs very slowly as their internal pressures are small and because diffusion is slow over long distances. There is a positive feedback during dissolution; as the bubble shrinks, both its internal pressure increases and the diffusive lengths become shorter. In 1950, Epstein and Plesset worked out the kinetics of the diffusion-limited dissolution process.[2] Assuming a stationary, solitary, spherical bubble in a gas-saturated solution, bubbles of 10 μm, 1 μm, and 100 nm radius were predicted to dissolve in 1 s, 10 ms, and 100 μs, respectively.

An alternative fate of a bubble is annihilation through growth until buoyant forces carry it to the liquid surface where it will "pop." This involves the reverse process of what was described above. Gas from the aqueous phase will flow into the bubble if the concentration of dissolved gas is higher than the concentration corresponding to the bubble's internal pressure and Henry's constant. This will occur if the solution had been previously saturated at a high pressure followed by a lowering of the pressure to give a supersaturated solution. The supersaturation, σ, is defined by how many fold higher the dissolved gas concentration is above the equilibrium concentration at ambient conditions such that:

$$(C_{sol} - C_{eq}) / C_{eq} = \sigma \qquad (1.3)$$

Because Henry's Law is a linear relation, the bubble's additional pressure arising from curvature and the supersaturation value at which the flow of gas switches from out of to into the bubble are interchangeable. Simply put, the gas within a 100 nm radius bubble is compressed to 14 atm above atmospheric pressure and would be metastable if the solution where supersaturated to 14 times higher than the equilibrium concentration. Figure 1.2

plots the relationship of bubble radius and the σ at which it is metastable. This is only a metastable equilibrium, however, because a miniscule fluctuation in size, temperature, or concentration will tip the bubble toward growth or dissolution. Chapter 2 of this dissertation demonstrates a method for measurement of nanobubble dissolution rates between 100 and 1000 times longer than diffusion limited predictions. To explain the discrepancy, we propose a kinetic limitation in the transfer of gas across the interface.

1.1.3 Bubble nucleation

The spontaneous formation of bubbles that occurs when a carbonated beverage is opened is the means by which the supersaturated solution returns to equilibrium. Nucleation is the stochastic process by which nanoscale clusters form from dissolved gas, thereby creating an interface where there was none to begin with. From Figure 1.2, it is not apparent how these clusters can form and grow into a bubble. Because the bubble pressure increases indefinitely with decreasing radius, a bubble cannot form by continuous growth through infinitesimal radii in a homogeneous medium. Instead, nucleation is driven by fluctuations in local density and composition that occur in proportion to the amount of thermal energy available at ambient conditions. For a bubble to form from these nuclei at a given supersaturation, the critical size at the line in Figure 1.2 must be reached for dissolved gas to flow into the bubble. At low supersaturations, it is exceedingly improbable that a bubble will form because the nuclei that form are typically too small and rapidly dissolve. The fluctuational appearance of a 100 nm radius nucleus is so unlikely to occur that a bubble is essentially never expected to grow from a solution supersaturated with a partial pressure of 14 atm. With increasing supersaturation, however, the probability of

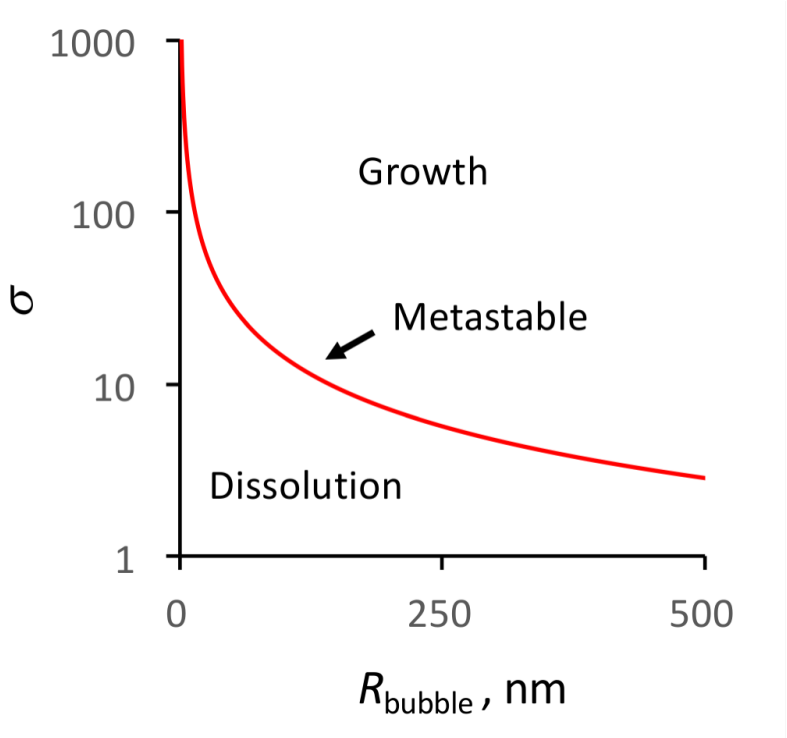

Figure 1.2. Plot of the supersaturation values, σ, providing metastability vs bubble radius, R_{bubble}. A bubble of a given radius will dissolve in a solution with a value of σ lower than the red line and will grow if σ is higher than the red line.

forming a critical nucleus increases exponentially. Therefore, nucleation is a threshold phenomenon where the rate of bubble formation transitions from immeasurably slow to extremely fast over a small range of supersaturation. Chapter 3 of this dissertation presents a measure of the dissolved gas concentration at which nucleation occurs quickly in comparison with the timescale of the experiment. We report that this critical concentration is dependent upon gas type and relate the concentration to the critical size of gas nuclei.

1.2 Nanobubble Literature

1.2.1 Interfacial nanobubbles

In context of the dynamics explained above, the first reports of stable, nanoscale bubbles 20 years ago were greeted with skepticism. Soft, sphere caps 10s of nanometers high and 100s of nanometers wide were observed on hydrophobic surfaces by atomic force microscopy to remain stable for hours in air-saturated water.[3,4] These structures were not present if solutions were degassed prior, and thus were concluded to be nanobubbles. A preponderance of experimental evidence produced over the last decade has supported both the gaseous composition and surprising longevity of interfacial nanobubbles.[5-10] The most widely accepted explanation for their stability involves the pinning of the bubble edges at defects on the surface.[5,11,12] With their contact line fixed, dissolution of the bubble serves to reduce the bubble's height, interfacial curvature, and consequently, the internal pressure. The hydrophobic surface then provides the means for a negative feedback by which the bubble can dissolve by shrinking only in height and find an equilibrium curvature provided there is a slight supersaturation of dissolved gas. Several reviews have covered the topic of interfacial nanobubbles thoroughly.[12-15]

1.2.2 Technological relevance

Much of the initial work studying surface forces was plagued by confounding "long-range forces," eventually leading to the discovery of nanobubbles as the main culprit.[16,17] Attraction between hydrophobic surfaces[18] and thin film stability[19] are two such cases where nanobubbles would be either a boon or a hindrance depending upon the application. Progress in gaining control of when and where or whether nanobubbles appear will ultimately determine their usefulness in technological applications.

Nanobubbles have important implications for the efficiency of separation processes that rely on particle-particle and particle-bubble interactions such as mineral flotation, oil extraction, and wastewater treatment.[20-24] Microbubbles revolutionized these industries, and it remains an intriguing possibility whether nanobubbles will offer further improvement through enhanced aggregation and flotation of nanoscale particulates.

There is a large body of literature surrounding the effect of surface nanobubbles on hydrodynamic slip.[25-28] Classical hydrodynamics typically assumes a "no slip" condition, or zero fluid velocity at solid walls. Certainly, the presence of nanobubbles will alter the slip condition and reduction of drag from the gaseous interface has been suggested theoretically.[29] Such a finding could be important for applications in microfluidics on up to marine cargo transportation.

Clever new uses for nanobubbles continue to be reported. An interesting method of desalinization was demonstrated employing a nanobubble-based membrane to allow vapor transfer while blocking solute transport.[30] Bubbles are also central to "nanomotors" that catalyze gas evolving reactions and form bubbles that propel them through liquid.[31] It has been shown that nanobubbles can be utilized to prevent surface fouling.[32] Hollow

nanoparticles with interesting plasmonic properties have been fabricated employing H_2 nanobubbles as both the substrate and reducing agent for their synthesis.[33] The formation of nanobubbles has been implicated in the "poisoning" of electrocatalytic nanoparticles.[34]

1.2.3 Electrochemically generated nanobubbles

In 2013, our laboratory published the first demonstration that individual nanobubbles can be nucleated by gas evolving electrochemical reactions at nanoelectrodes. Nanoelectrochemistry provides an avenue for precise and wide-ranging control over reaction rates, allowing systems to be taken far from equilibrium. The inspiration for the experiment was simply to see if a phase transition was observable when an immense amount of gas was forced into a small volume of liquid. Under voltage control, Luo et al. reported a precipitous drop in the current associated with H^+ reduction to form H_2 at Pt electrodes smaller than 50 nm radius.[35] The phenomenon was attributed to a significant decrease in the electroactive area of the electrode due to formation of a nanobubble blocking transport of H^+. The peak current, or dissolved H_2 concentration, at which a bubble formed was found to be highly reproducible and essentially independent of scan rate (i.e., a threshold phenomenon). Furthermore, it was hypothesized that the low current following bubble formation represented a steady-state nanobubble for which the ongoing electrogeneration of H_2 at the Pt left exposed to solution was limited by the rate of bubble dissolution. These experiments could be performed reproducibly on a given electrode, suggesting that the bubble dissolved between subsequent experiments. This foundational work and the many questions it raises regarding the process of bubble nucleation, steady-state dynamics, and lifetime after gas supply is removed are the basis for this dissertation.

1.2.4 Publications not included in this dissertation

During my graduate studies, I was an author on a number of other publications that are not included in this dissertation except to be listed here.

1. German, S. R.; Hurd, T. S.; White, H. S.; Mega, T. L. Sizing Individual Au Nanoparticles in Solution with Sub-Nanometer Resolution. *ACS Nano* **2015**, *9*, 7186–7194.

2. Chen, Q.; Wiedenroth, H. S.; German, S. R.; White, H. S. Electrochemical Nucleation of Stable N_2 Nanobubbles at Pt Nanoelectrodes. *J. Am. Chem. Soc* **2015**, *137*, 12064–12069.

3. Edwards, M. A.; German, S. R.; Dick, J. E.; Bard, A. J.; White, H. S. High-Speed Multipass Coulter Counter with Ultrahigh Resolution. *ACS Nano* **2015**, *9*, 12274–12282.

4. Zhang, Y.; Edwards, M. A.; German, S. R.; White, H. S. Multipass Resistive-Pulse Observations of the Rotational Tumbling of Individual Nanorods. *J. Phys. Chem. C* **2016**.

5. Liu, Y.; Edwards, M. A.; German, S. R.; Chen, Q.; White, H. S. The Dynamic Steady State of an Electrochemically Generated Nanobubble *Langmuir* Just Accepted Manuscript DOI: 10.1021/acs.langmuir.6b04607

1.3 References

(1) Schrödinger, E. , Notiz über den Kapillardruck in Gasblasen. *Ann. Phys.*, **1915**, 351, 413–418.

(2) Epstein, P. S.; Plesset, M. S. On the Stability of Gas Bubbles in Liquid-Gas Solutions. *J. Chem. Phys.* **1950**, *18*, 1505–1509.

(3) Lou, S.-T.; Ouyang, Z.-Q.; Zhang, Y.; Li, X.-J.; Hu, J.; Li, M.-Q.; Yang, F.-J. Nanobubbles on Solid Surface Imaged by Atomic Force Microscopy. *J. Vac. Sci. Technol. B* **2000**, *18*, 2573–2575.

(4) Tyrrell, J. W.; Attard, P. Images of Nanobubbles on Hydrophobic Surfaces and Their Interactions. *Phys. Rev. Lett.* **2001**, *87*, 176104.

(5) German, S. R.; Wu, X.; An, H.; Craig, V. S. J.; Mega, T. L.; Zhang, X. Interfacial Nanobubbles Are Leaky: Permeability of the Gas/Water Interface. *ACS Nano* **2014**, *8*, 6193–6201.

(6) Seo, D.; German, S. R.; Mega, T. L.; Ducker, W. A. Phase State of Interfacial Nanobubbles. *J. Phys. Chem. C* **2015**, 119, 14262-14266.

(7) Zhang, X.; Khan, A.; Ducker, W. A Nanoscale Gas State. *Phys. Rev. Lett.* **2007**, *98*, 136101.

(8) Borkent, B.; Dammer, S.; Schönherr, H. Superstability of Surface Nanobubbles. *Phys. Rev. Lett.* **2007**, *98*, 204502.

(9) Zhang, X.; Quinn, A.; Ducker, W. Nanobubbles at the Interface Between Water and a Hydrophobic Solid. *Langmuir* **2008**, *24*, 4756–4764.

(10) Zhang, X. Quartz Crystal Microbalance Study of the Interfacial Nanobubbles. *Phys. Chem. Chem. Phys.* **2008**, *10*, 6842-6848.

(11) Lohse, D.; Zhang, X. Pinning and Gas Oversaturation Imply Stable Single Surface Nanobubbles. *Phys. Rev. E* **2015**, *91*, 031003-031005.

(12) Lohse, D.; Zhang, X. Surface Nanobubbles and Nanodroplets. *Rev. Mod. Phys.* **2015**, *87*, 1–59.

(13) Craig, V. S. J. Very Small Bubbles at Surfaces—the Nanobubble Puzzle. *Soft Matter* **2011**, *7*, 40–48.

(14) Alheshibri, M.; Qian, J.; Jehannin, M.; Craig, V. S. J. A History of Nanobubbles. *Langmuir* **2016**, *32*, 11086–11100.

(15) Hampton, M.; Nguyen, A. Nanobubbles and the Nanobubble Bridging Capillary Force. *Adv. Colloid Interface Sci.* **2010**, *154*, 30–55.

(16) Parker, J. L.; Claesson, P. M.; Attard, P. Bubbles, Cavities, and the Long-Ranged Attraction Between Hydrophobic Surfaces. *J. Phys. Chem.* **1994**, *98*, 8468–8480.

(17) Carambassis, A.; Jonker, L.; Attard, P.; Rutland, M. Forces Measured Between Hydrophobic Surfaces Due to a Submicroscopic Bridging Bubble. *Phys. Rev. Lett.* **1998**, *80*, 5357–5360.

(18) Faghihnejad, A.; Zeng, H. Interaction Mechanism Between Hydrophobic and Hydrophilic Surfaces: Using Polystyrene and Mica as a Model System. *Langmuir* **2013**, *29*, 12443–12451.

(19) Stockelhuber, K.; Radoev, B.; Wenger, A.; Schulze, H. Rupture of Wetting Films Caused by Nanobubbles. *Langmuir* **2004**, *20*, 164–168.

(20) Calgaroto, S.; Wilberg, K. Q.; Rubio, J. Minerals Engineering. *Minerals Engineering* **2014**, *60*, 33–40.

(21) Albijanic, B.; Ozdemir, O.; Nguyen, A. V.; Bradshaw, D. A Review of Induction and Attachment Times of Wetting Thin Films Between Air Bubbles and Particles and Its Relevance in the Separation of Particles by Flotation. *Adv. Colloid and Interface Sci.* **2010**, *159*, 1–21.

(22) Min, Q.; Duan, Y.-Y.; Peng, X.-F.; Mujumdar, A. S.; Hsu, C.; Lee, D.-J. Froth Flotation of Mineral Particles: Mechanism. *Dry Technol.* **2008**, *26*, 985–995.

(23) Fan, M.; Tao, D.; Honaker, R.; Luo, Z. Nanobubble Generation and Its Application in Froth Flotation (Part I): Nanobubble Generation and Its Effects on Properties of Microbubble and Millimeter Scale Bubble Solutions. *Mining Sci. and Technol.* **2010**, *20*, 0001–0019.

(24) Verrelli, D. I.; Koh, P. T. L.; Nguyen, A. V. Chemical Engineering Science. *Chem. Eng. Sci.* **2011**, *66*, 5910–5921.

(25) Barrat, J.; Bocquet, L. Large Slip Effect at a Nonwetting Fluid-Solid Interface. *Phys. Rev. Lett.* **1999**, *82*, 4671–4674.

(26) Bocquet, L.; Charlaix, E. Nanofluidics, From Bulk to Interfaces. *Chem. Soc. Rev.* **2010**, *39*, 1073.

(27) Rothstein, J. P. Slip on Superhydrophobic Surfaces. *Annu. Rev. Fluid Mech.* **2010**, *42*, 89–109.

(28) Wang, Y.; Bhushan, B. Boundary Slip and Nanobubble Study in Micro/Nanofluidics Using Atomic Force Microscopy. *Soft Matter* **2010**, *6*, 29–66.

(29) de Gennes, P. G. On Fluid/Wall Slippage. *Langmuir* **2002**, *18*, 3413–3414.

(30) Lee, J.; Laoui, T.; Karnik, R. Nanofluidic Transport Governed by Theliquid/Vapour Interface. **2014**, 1–7.

(31) Paxton, W. F.; Kistler, K. C.; Olmeda, C. C.; Sen, A.; St Angelo, S. K.; Cao, Y.; Mallouk, T. E.; Lammert, P. E.; Crespi, V. H. Catalytic Nanomotors: Autonomous Movement of Striped Nanorods. *J. Am. Chem. Soc* **2004**, *126*, 13424–13431.

(32) Liu, G.; Wu, Z.; Craig, V. S. Cleaning of Protein-Coated Surfaces Using Nanobubbles: an Investigation Using a Quartz Crystal Microbalance. *J. Phys. Chem. C* **2008**, *112*, 16748–16753.

(33) Huang, C.; Jiang, J.; Lu, M.; Sun, L.; Meletis, E.; Hao, Y. Capturing Electrochemically Evolved Nanobubbles by Electroless Deposition. a Facile Route to the Synthesis of Hollow Nanoparticles. *Nano Letters* **2009**, *9*, 4297–4301.

(34) Jung, A. R.; Lee, S.; Joo, J. W.; Shin, C.; Bae, H.; Moon, S. G.; Kwon, S. J. Potential-Controlled Current Responses From Staircase to Blip in Single Pt

Nanoparticle Collisions on a Ni Ultramicroelectrode. *J. Am. Chem. Soc.* **2015**, *137*, 1762–1765.

(35) Luo, L.; White, H. S. Electrogeneration of Single Nanobubbles at Sub-50-Nm-Radius Platinum Nanodisk Electrodes. *Langmuir* **2013**, *29*, 11169–11175.

CHAPTER 2

ELECTROCHEMICAL MEASUREMENT OF HYDROGEN AND NITROGEN NANOBUBBLE LIFETIMES AT PT NANOELECTRODES

German, S. R.; Chen, Q.; Edwards; M. A. White, H. S.

J. Electrochem. Soc. 2016, 163, H3160-H3166

2.1 Introduction

The lifetimes of *individual* H_2 and N_2 nanobubbles, electrochemically generated at Pt nanoelectrodes (7-85nm-radius), have been measured using a fast-scan electrochemical technique. To measure lifetime, a stable single H_2 or N_2 bubble is first generated by reducing protons or oxidizing hydrazine, respectively, at the Pt nanoelectrode. The electrode potential is then rapidly stepped (<100μs) to a value where the bubble is unstable and begins to dissolve by gas molecule transfer across the gas/water interface and diffusion. The electrode potential is immediately scanned back to values where the bubble was initially stable. Depending on the rate of this second voltammetric scan, the initial bubble may or may not have time to dissolve, as is readily determined by the characteristic

voltammetric signature corresponding to the nucleation of a new bubble. The transition between these regimes is used to determine the bubble's lifetime. The results indicate that dissolution of a H_2 or N_2 nanobubble is, in part, limited by the transfer of molecules across the gas/water interface. A theoretical expression describing mixed diffusion/kinetic control is presented and fit to the experimental data to obtain an interfacial gas transfer rate of $\sim 10^{-9}$ mol N^{-1} s^{-1}.

Interfacial nanobubbles are gaseous, nanoscale spherical caps on a solid substrate immersed in a gas-saturated solution. They were first proposed to explain the long-range attractive interactions between hydrophobic surfaces.[1-3] Initially their existence was contentiously debated,[4,5] but their existence, composition and stability has since been documented in numerous experiments.[6-10] The argument against their existence is due to the lack of a theoretical understanding of their peculiar longevity, often measured in days.[11]

It is well understood that a spherical bubble suspended in a gas-saturated liquid should be intrinsically unstable. The internal pressure within a bubble of radius R exceeds that of its surroundings by the Laplace pressure, $2\gamma/R$, where γ is the liquid's surface tension. The gas within the bubble therefore has a higher chemical potential than the dissolved gas and must reach equilibrium by dissolution into the liquid and transport away from the bubble. While this process is quite slow for macroscopic bubbles, the rate of dissolution increases by orders of magnitude for nanoscopic bubbles, due to the increase in Laplace pressure and decreased diffusion lengths. Epstein and Plesset[12] first detailed a theoretical framework for growing and shrinking bubbles and later Ljunggren and Eriksson[13] explicitly extended the theory to the nanoscale. Both mathematical approaches predict isolated, spherical bubbles smaller than 100 nm radius to dissolve in less than 100

microseconds. Experimentally, and as noted above, nanobubbles are observed to persist for much longer periods, often for several days.[11]

Several different mechanisms have been proposed to explain the persistence of nanobubbles on surfaces: a transport barrier and lowering of the surface tension by contaminants with an affinity for the gas/water interface,[14] a dynamic equilibrium afforded by a recirculating flow above nanobubbles that keeps dissolved gas localized,[15] and a thin layer of gas adsorbed to the substrate that feeds into the bubble's contact line.[16,17] Another theory gaining acceptance arises from the experimental observation that the contact radius of a nanobubble may be pinned to the substrate and only the bubble's height decreases as the bubble dissolves.[18] Pinning provides a negative feedback for dissolution, as the Laplace pressure reduces as the bubble shrinks in height and increases its radius of curvature. Mathematical treatment of this model has been presented that suggests pinned bubbles can be stable under a modest gas supersaturation, but will dissolve quite quickly at any level equal to or below saturation. [19,20] Indeed, it has been demonstrated that interfacial nanobubbles will dissolve if the solution is degassed,[21,22] although experimental measurements of dissolution rates in this situation are lacking. Dissolution rates of micron-sized bubbles in bulk solution have been measured and agree well with the theory of Epstein and Plesset.[23,24] However, recent studies of very high curvature nanobubbles by transmission electron microscopy (TEM), where 10 nm radius bubbles were observed to be stable over many seconds, may suggest very different dissolution rates for nanobubbles.[25]

Electrochemistry provides an interesting avenue for the study of both the nucleation and stability of nanobubbles. Gas producing reactions create large supersaturations near an

electrode surface leading to heterogeneous nucleation of bubbles. The resulting ensembles of bubbles decorating electrode surfaces have been imaged by optical microscopy and AFM. [26-28] As depicted in Scheme 2.1, our lab has utilized Pt nanodisk electrodes to generate *individual* nanobubbles whose size is determined by the size of the electrode. We have reported the generation of individual H_2 bubbles by reduction of protons[29,30] ($2H^+ + 2e^- \rightarrow H_2$), O_2 nanobubbles by oxidation of water ($H_2O \rightarrow O_2 + 4H^+ + 4e^-$),[31] and N_2 bubbles by oxidation of hydrazine ($N_2H_4 + 4OH^- \rightarrow N_2 + 4H_2O + 4e^-$).[32] We have demonstrated that the nucleation of a bubble occurs when a critical gas supersaturation (310 times saturation for H_2 (0.25 M) and 160 times saturation for N_2 (0.11 M)) is generated at the electrode surface. Once formed, these nanobubbles quickly grow across the electrode surface and reach a dynamic equilibrium, where the diffusive flux of gas out of the bubble is balanced by the electrogeneration of hydrogen, oxygen or nitrogen that enters the bubble, resulting in a stable nanobubble, as shown in Scheme 2.1.

In this work, we utilize the high temporal resolution of nanoelectrodes to experimentally measure the lifetime of electrochemically generated nanobubbles using a new fast-scan voltammetric method. These experiments represent a crucial test for existing theories regarding the mechanism of nanobubble stability.

2.2 Experimental Methods

2.2.1 Chemicals

Sulfuric acid (Mallinckrodt, 96.2%, ACS grade) and N_2H_4 (Aldrich, 35 wt% in water, stored under N_2), were used as received.

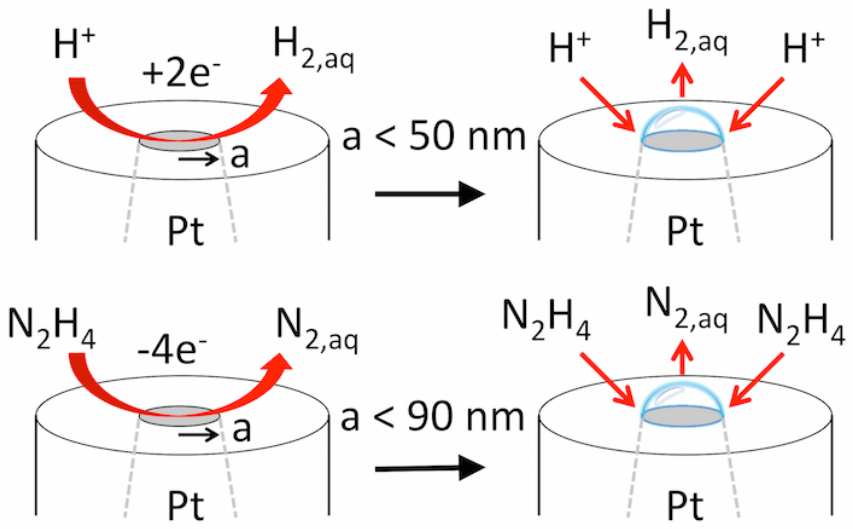

Scheme 2.1. Schematic drawing of the electrochemical formation of single H_2 and N_2 bubbles from H^+ electroreduction and N_2H_4 electrooxidation at Pt nanodisk electrodes with radii less than 100 nm.

2.2.2 Nanoelectrode fabrication and characterization

Pt nanodisk electrodes were fabricated according to previously reported procedures from our laboratory.[33] The radii of the nanodisk electrodes, *a*, were determined from the voltammetric steady-state diffusion-limited current, i_{lim}, for the oxidation of ferrocene ($Fc \rightarrow Fc^+ + e^-$) dissolved in acetonitrile (CH_3CN) containing 0.10 M tetrabutylammonium hexafluorophosphate ($TBAPF_6$). The radii were calculated using the equation

$$i_{lim} = 4naFD_{Fc}C^*_{Fc} \quad (2.1)$$

where D_{Fc} (2.4×10^{-5} cm^2/s)[34] and C^*_{Fc} (3.25 mM) are the diffusion coefficient and the bulk concentration of Fc, respectively, *n* is the number of electrons transferred per molecule (= 1 for Fc oxidation) and *F* = 96485 C/mol is Faraday's constant.

2.2.3 Cell configuration and data acquisition

A HEKA EPC10-USB patch clamp amplifier was used for lifetime measurements with current sampling at 100 kHz and a 10 kHz filter. A Ag/AgCl (3 M NaCl) electrode or a saturated calomel electrode (SCE) was used as the counter/reference electrode in a two-electrode cell configuration.

2.3 Results and Discussion

2.3.1 Nucleation of a single nanobubble

As previously reported, the formation of a single H_2 or N_2 gas nanobubble at a Pt nanodisk electrode (as in Scheme 2.1) can be observed during the reduction of H^+ and oxidation of N_2H_4, respectively. Figure 2.1(a) shows a typical cyclic voltammogram recorded at a 27 nm radius Pt nanodisk electrode immersed in 0.5 M H_2SO_4. As the

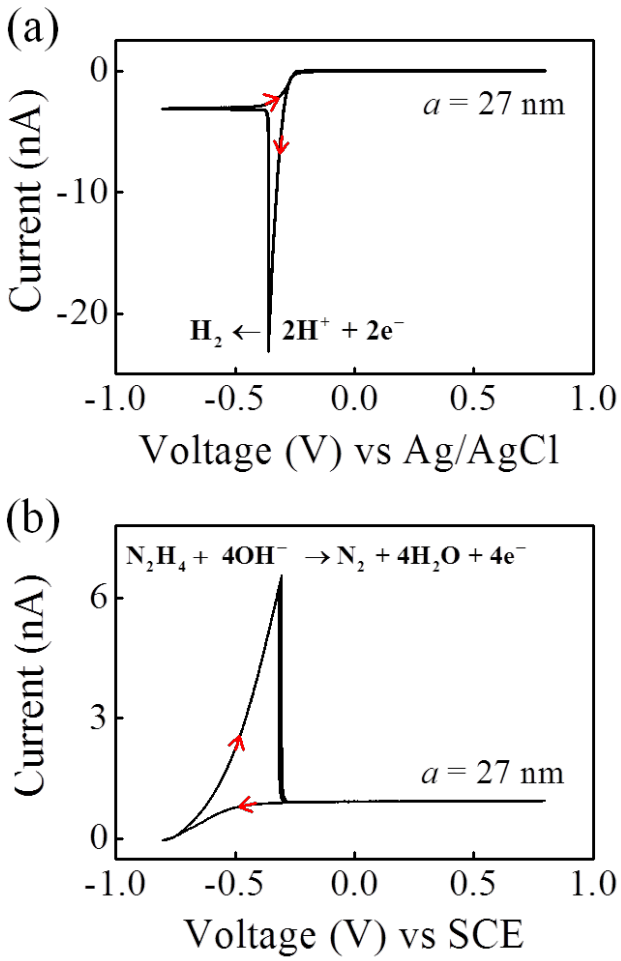

Figure 2.1. *i-V* responses of (a) a 27 nm radius Pt nanoelectrode immersed in 0.5 M H_2SO_4 for H_2 nanobubble formation, and (b) the same Pt nanoelectrode immersed in 1.0 M N_2H_4 for N_2 nanobubble formation at a scan rate of 200 mV/s. The voltammograms shown are for two cycles each to demonstrate the reproducibility of bubble formation, as well as bubble dissolution at slow voltammetric scan rates.

voltage is scanned to negative potentials, the current associated with H^+ reduction (i.e., H_2 electrogeneration, beginning at ~-0.2V vs Ag/AgCl) increases rapidly until reaching a peak current, i_{nb}^{p}, at 23 nA and then suddenly drops to a low residual current. Figure 2.1(b) shows a similar peak-shaped cyclic voltammogram for the same 27 nm radius Pt nanodisk electrode immersed in 1.0 M N_2H_4, where the oxidation of N_2H_4, beginning at ~-0.7 V, leads to N_2 nanobubble nucleation when the current reaches a value, i_{nb}^{p}, of 6.5 nA. This characteristic waveshape is due to the formation of a single gas nanobubble at the electrode surface. After formation of a H_2 or N_2 nanobubble, the current decreases to a small residual current, i_{nb}^{r}, which is very stable at potentials negative or positive of the peak potentials for H_2 or for N_2, respectively. As previously reported and detailed,[29,32] i_{nb}^{r} corresponds to the rate of H_2 and N_2 electrogeneration at the 3-phase interface (gas/water/Pt, see Scheme 2.1) that is required to balance the H_2 and N_2 diffusive outflux from the bubble into the bulk solution. H_2 and N_2 nanobubbles are only stable when the electron-transfer reactions are occurring to regenerate the gas lost by dissolution. The low value of i_{nb}^{r} also indicates that the bubble covers almost the entirety of the electrode. In this work, the radius of the electrode is used to approximate the radius of the bubble at this steady state.

On the voltammetric timescales used in recording the data shown in Figure 2.1, the bubbles rapidly disappear when the potential is scanned to positive values at the electrode covered by the H_2 bubble, or to negative values for the electrode covered by the N_2 bubble. This is evident by the observations that H_2 oxidation is not visible on the positive-going scan and that the nucleation wave is observed on consecutive voltammetric scans (the high reproducibility of the two consecutive cycles makes it difficult to distinguish them). The

peak-shaped waves in Figure 2.1 would not be observed on the second scans if the bubble persisted on the electrode after electrogeneration of H_2 and N_2 ceased, demonstrating that the bubble fully dissolves during each cycle when the experiment is performed at a scan rate of 200 mV/s.

2.3.2 Kinetics of H_2 and N_2 bubble formation

Prior to describing voltammetric experiments aimed at measuring nanobubble dissolution rates, we performed a preliminary semi-quantitative investigation of the range of scan rates where nanobubble formation can be observed. Previously, we showed that both the bubble formation and dynamic equilibrium stages are in a steady-state condition as evidenced by the voltammetric waveshape being insensitive to the scan rate for scan rates less than 2 V/s.[29,32] At higher scan rates, some distortion of cyclic voltammograms occurs from capacitive currents and sluggish electron-transfer kinetics. However, it is anticipated that insufficient gas generation and/or the finite rate of bubble nucleation are expected to prevent bubble formation at sufficiently high scan rates. This is born out in the voltammetric data presented in Figure 2.2, which shows the voltammetric response on the initial forward scan as a function of potential sweep rate. We observe bubble formation at scan rates up to 500 V/s for H^+ reduction and 200 V/s for N_2H_4 oxidation, as evident by the sharp current drop indicating the formation of the gas phase. The increasing overpotential and larger peak currents required for bubble formation suggest that the nucleation step is a relatively slow process, but extracting the kinetics of the phase transformation is complicated by kinetic limitations due to slow electron transfer

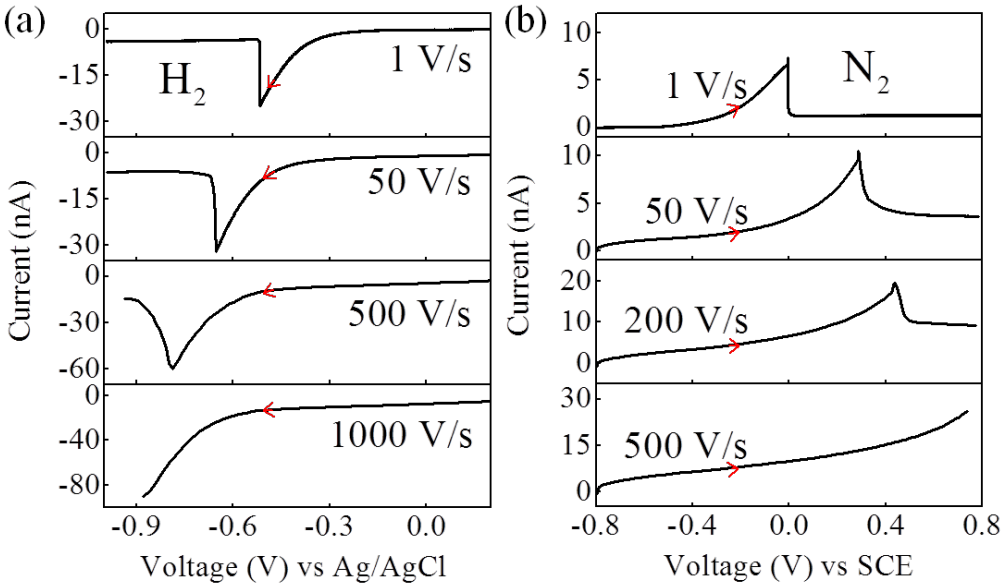

Figure 2.2. *i-V* responses for both H_2 and N_2 bubble producing reactions as a function of scan rate at a 32 nm radius nanoelectrode immersed in (a) 0.5 M H_2SO_4, and (b) 1.0 M N_2H_4. Bubble formation is observed at scan rates up to 500 V/s for H^+ reduction and 200 V/s for N_2H_4 oxidation.

(especially for N_2H_4 oxidation). While nanobubble formation cannot be observed at scan rates above 500 V/s for H_2 and 200 V/s for N_2, the kinetics for bubble electrogeneration are sufficiently fast to design experiments to measure nanobubble dissolution (vide infra).

2.3.3 Bubble dissolution rates

Figure 2.3 shows the general strategy and voltammetric waveform used to measure the lifetime of a H_2 nanobubble (an analogous strategy is employed for investigation of N_2 bubble lifetime). A single H_2 bubble is nucleated (i) by scanning the voltage to negative potentials at a moderate rate (1 V/s), reaching the dynamic steady state (ii) after bubble formation. The voltage is then rapidly stepped (< 0.1 ms) to 0 V (iii) and immediately scanned negatively at varying scan rates ranging between 2-500 V/s (iv). There are two experimental outcomes, which can be discriminated by the voltammetric response, and which depend upon the scan rate employed in step (iv). At a sufficiently fast scan rate (iv-b) the H_2 bubble does not completely dissolve, nor is it reoxidized (i.e., $H_2 \rightarrow 2H^+ + 2e^-$) before hydrogen generation restores the bubble to its steady state at step (v). Conversely, at a sufficiently lower scan rate (iv-a) the H_2 nanobubble has sufficient time to dissolve, or be oxidized, and a new bubble is nucleated on the second forward scan, as the current reestablishes the supersaturation of H_2. As shown in the preceding section, nucleation of a H_2 nanobubble is observed up to 500 V/s. Thus, if the bubble dissolves following the step to the positive potential, the nucleation of a new bubble can be observed on the fast negative-going potential scan.

Figures 2.4(a) and 2.4(c) shows representative *i-t* traces resulting from the voltammetric experiment schematically depicted in Figure 2.3, corresponding to the

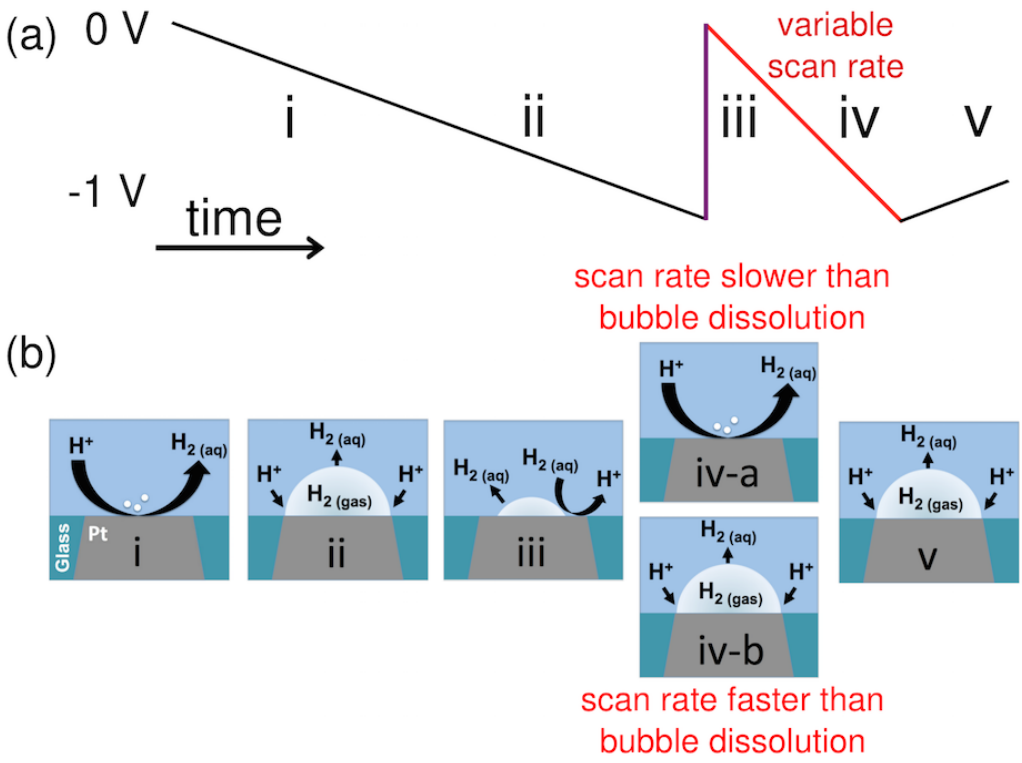

Figure 2.3. (a) Schematic of the voltammetric experiment used to measure the lifetime of a H_2 nanobubble . The voltage is initially scanned towards negative potentials at 1 V/s resulting in the electrogeneration of H_2 and nucleation (i) of a nanobubble that grows and reaches a dynamic equilibrium (ii). Steps (i) and (ii) result in a voltammetric wave in which the current drops suddenly upon nanobubble formation, as previously shown in Figure 2.1. At the end of the potential scan (-1V), the electrode potential is stepped back to 0.0 V (iii), a potential at which H_2 is no longer generated, and the H_2 within the bubble is either oxidized to H^+ or diffuses into the bulk solution. A second scan to negative potentials is initiated immediately after the potential step (iv). If the scan rate of this second forward scan is sufficiently slow, the nanobubble has time to completely dissolve, resulting in the nucleation and growth of a new nanobubble on the negative scan (iv-a), which is readily discerned by appearance of the characteristic voltammetric peak for nanobubble formation. Conversely, if the scan rate is sufficiently fast, the preexisting nanobubble does not have time to dissolve. In this case, the characteristic voltammetric peak is not observed (iv-b), while still restoring the residual current at step (v). By varying the voltammetric scan rate of the second potential scan (step iv) in repeated experiments, the lifetime of the bubble can be determined. An analogous voltage waveform is used to measure the lifetime of N_2 nanobubbles.

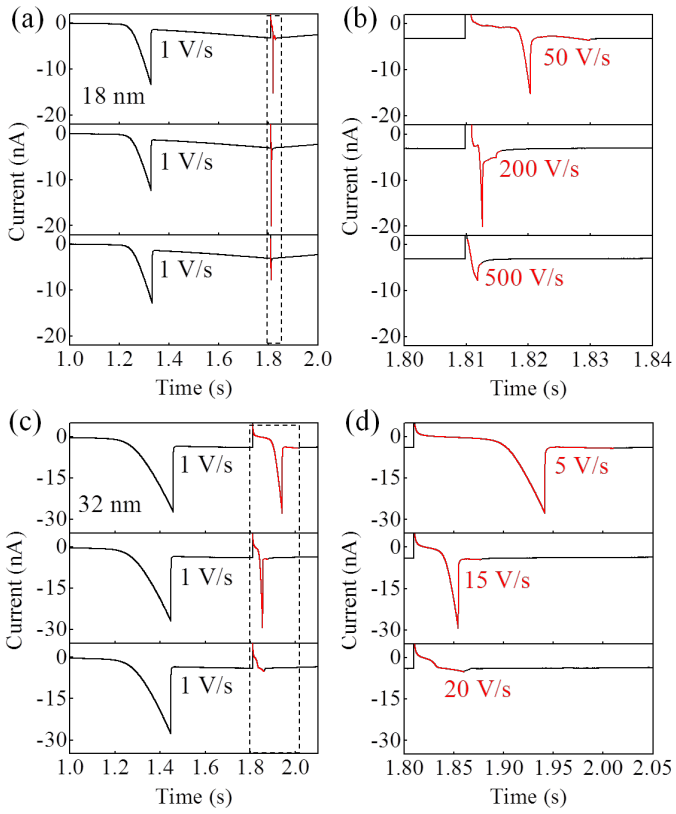

Figure 2.4. *i-t* traces illustrating the measurement of the lifetimes of H_2 bubbles generated at Pt electrodes of (a/b) 18 and (c/d) 32 nm radius, following the description of the experimental method depicted in Figure 2.3. The reduction of H^+ by scanning the voltage at 1 V/s, to -1 V generates a stable single hydrogen bubble as indicated by the drop in current at ~1.4 s in (a) and (c). The characteristic lifetime of the bubbles are determined by stepping the voltage back to 0.0 V at 1.81 s where the bubble begins to dissolve, and then immediately scanning the voltage from 0 to -1 V, again at a fast scan rate. The currents resulting from the fast scan are highlighted in red and are shown on an expanded time scale in parts (b) and (d). There are two possible outcomes during the fast potential scan: at sufficiently fast scan rates the bubble will not completely dissolve and the formation of a new bubble is not observed; and at sufficiently slow scan rates the original bubble will dissolve and a new bubble will form as indicated by the signature waveshape of a nucleating bubble. From the data in (a,b), the 18 nm radius bubble completely dissolves between a voltage scan rate of 200 and 500 V/s. For the 32 nm radius bubble in (c,d), the bubble dissolves at scan rates between 15 and 20 V/s.

electrogeneration and dissolution of H_2 nanobubbles at (a) 18 and (c) 32 nm radius Pt nanodisk electrodes. An expanded view of the high-speed section of the voltammetric scan is presented in Figures 2.4(b) and 2.4(d) for each. For a given electrode, three different scan rates are shown: two rates slow enough that the bubble dissolves and a faster rate under which the bubble survives. The series of *i-t* traces in Figure 2.4(a) all show the i_{nb}^{p} ~13 nA peak current at ~1.3 s, denoting the formation of the initial 18 nm radius bubble as the voltage is scanned at 1 V/s to -1 V. At 1.81 s, the potential is stepped back to 0.0 V, and scanned to negative potentials again, using different scan rates to determine if the bubble persists or dissolves.

Figure 2.4(b) shows expanded regions of the fast-scan region used to estimate the lifetime of the bubble at the 18 nm Pt electrode. The anodic current response to the potential step at 1.81 s results from a combination of capacitive current and hydrogen oxidation at a gas/water/Pt interface that is changing dynamically while the bubble shrinks. Immediately following this transient current, the potential is scanned in the negative direction to probe the lifetime of the bubble. At slower scan rates (50 and 200 V/s), the *i-t* response shows the characteristic nucleation peak corresponding to the formation of a new H_2 bubble, unequivocally demonstrating that the bubble dissolves on the time scale of these scans. At the faster scan rate, 500 V/s, only a small cathodic current is observed, which we believe corresponds to cathodic charging current or a small amount of H_2 generation that goes into "reinflating" the original, but partially dissolved, bubble still persisting on the electrode. Figures 2.4(c) and (d) show example *i-t* traces recorded at a larger 32 nm radius Pt electrode. As expected, the persistence of the bubble is longer for the larger bubble, as indicated by the lack of the peak current for nucleation occurring at

lower scan rates (20 V/s).

In a completely analogous set of experiments, Figure 2.5 demonstrates the lifetimes of N_2 bubbles can also be measured. The data in Figure 2.5 were recorded using the same 32 nm Pt electrode used to generate the H_2 nanobubbles shown in Figure 2.4(c) and (d), and show that the N_2 nanobubble does not dissolve at scan rates at ~10 V/s and above. Note, in contrast to the H_2 bubble and chemically reversible reduction of H^+, the oxidation of N_2H_4 is not chemically reversible, i.e., $N_2 + 4H_2O + 4e^- \rightarrow N_2H_4 + 4OH^-$ does not occur. Thus, the N_2 bubble disappears only by physical dissolution.

Cyclic voltammetry is frequently used to study short-lived chemical species. The characteristic time, τ, of a voltammetric measurement is related to the scan rate, ν, and the difference in potential, ΔE, by the relationship, $\tau = \Delta E/ \nu$, or simply the time elapsed.[35] In practice, a reactive intermediate is observable when τ is of the order of magnitude of the intermediate's lifetime of which a dissolving bubble is a specific example. Here, the fastest scan rate at which the bubble dissolves and is reformed is used to calculate the lifetime of the nanobubble prior to its dissolution with a ΔE of 0.4 V (for both H_2 and N_2) corresponding to the difference between the starting potential of the second forward scan and the typical voltage at which bubble nucleation occurs (as in Figure 2.1). (Exact choice of ΔE will have small effects on lifetimes.) In addition, the consumption (H_2 only)/generation of gas during the second forward scan will shorten/extend these lifetimes slightly, but does not change the conclusions of this work. From the data in Figures 2.4 and 2.5, the lifetimes of the H_2 nanobubbles at the 18 and 32 nm radius Pt electrodes are 2 (ν = 200 V/s) and 27 ms (ν = 15 V/s), while the lifetime of the N_2 at the 32 nm radius Pt electrode is 67 ms (ν = 6 V/s).

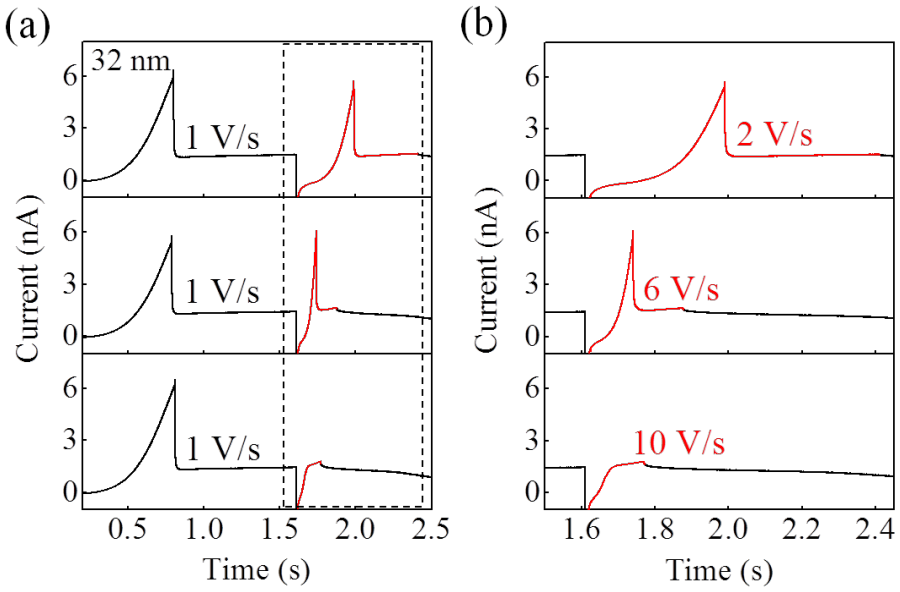

Figure 2.5. *i-t* traces illustrating the measurement of the lifetime of a N_2 bubble formed at a 32 nm radius Pt electrode. The principle of the measurement is the same as for H_2 bubbles (see captions of Figures 2.3 and 2.4). The N_2 bubble is generated by oxidation of N_2H_4 while scanning the potential from -0.8 to +0.8 V. The potential is stepped from +0.8 V back to -0.8 V at 1.6 s, and the voltage is scanned back towards positive potentials at variable scan rates to probe the lifetime of the N_2 nanobubble. For this 32 nm radius Pt electrode, N_2 bubble reformation is observed at 2 and 6 V/s, but not at 10 V/s.

Figure 2.6 shows our experimentally measured lifetimes as a function of the nanoelectrode/initial bubble radius (points) alongside predictions of bubble dissolution rates from theoretical models (lines). It is clear that our experimentally measured lifetimes are 2 to 3 orders of magnitude longer than predicted by theory from the literature (solid and dotted lines). Theoretical values were computed both for bubbles that maintain a hemispherical shape during dissolution (as in Epstein and Plesset,[12] dotted lines), and for bubbles that are initially hemispherical but whose contact line is pinned at the circumference of the initial bubble (as in Zhang and Lohse,[19] solid lines). (Mathematical details of these models are given in the Appendix.) In the latter case, the bubble radius of curvature increases and, consequently, its internal pressure decreases as it shrinks in height. Both theoretical models assume that bubble dissolution is limited by diffusion and that the dissolved gas concentration at the bubble interface is always at equilibrium with the bubble's internal pressure (determined by its time-dependent radius of curvature) as described by Henry's Law. Assuming a mass balance during bubble dissolution, where the number of gas molecules leaving the bubble to maintain the surface concentration is compensated by a concomitant change in bubble radius or height by the ideal gas law, allows calculation of the time for the bubble's volume to reach zero. The difference in the assumptions of the two theories yields a prediction of approximately a factor of two slower dissolution for the "negative feedback" model of a pinned bubble relative to the "positive feedback" model of a hemispherical bubble. Both models predict that N_2 bubbles will have lifetimes ~3 times longer than a H_2 bubble of the same size based upon the difference in dissolved gas diffusion coefficients

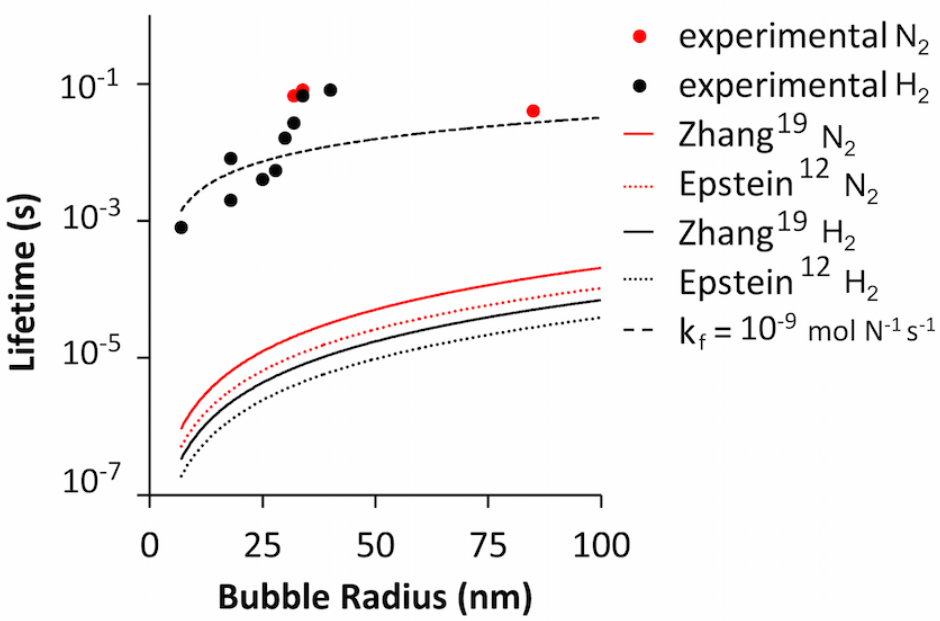

Figure 2.6 Bubble lifetime versus initial hemispherical bubble radius. Black components correspond to H_2 bubbles and red components to N_2. Circles are data points from electrochemical lifetime experiments as detailed in Figures 2.3-5. Dotted lines are theoretical calculations based upon the model in Epstein and Plesset[12] in which bubbles maintain a hemispherical shape as they shrink. Solid lines are theoretical calculations based upon the model in Zhang and Lohse[19] in which only the bubble's height shrinks as it dissolves, because its contact line is pinned to the surface. The dashed line incorporates a kinetic rate constant for transfer of H_2 across the gas/water interface (Equation 2.2) to allow a fit to experimental data.

(1.9×10^{-5} cm^2/s and 4.5×10^{-5} cm^2/s for N_2 and H_2, respectively)[36,37] and difference in gas solubility (0.69 mM/atm and 0.8 mM/atm for N_2 and H_2, respectively).

2.3.4 Kinetic limitations

Previous studies of dissolution of suspended spherical microbubbles[23,24] (5-50 μm) correspond well with the diffusion-controlled predictions of Epstein and Plesset theory within a factor of 2. However, the dissolution of the electrogenerated nanobubbles might not be expected to be diffusion limited. The flux of dissolved gas away from a nanoscale bubble is several orders of magnitude faster than the micron-sized bubbles, and the high internal pressures further increase the outflux. Our measured slower dissolution rates may indicate that a dissolving nanobubble is limited by the transfer of molecules across the gas/water interface. To assess this hypothesis, we modified Zhang and Lohse's dissolution model of a pinned bubble by adding a first order rate constant for gas/water interfacial transfer, k_f, as the sole free parameter (see Appendix for derivation). The resulting expression for bubble height, h, as a function of time, t, is governed by

$$\frac{dh}{dt} = -4DRT\left(\left(\left(P_{Ext} + \frac{4h\gamma}{a^2+h^2}\right)k_H + \frac{4Dc_b a k_H \Phi(\theta)}{\pi\left(a^2+h^2\right)k_f}\right)\Big/\left(1 + \frac{4Dak_H\Phi(\theta)}{\pi\left(a^2+h^2\right)k_f}\right) - c_b\right)a\Phi(\theta)$$

$$\left(\frac{\pi}{6}h\left(3a^2+h^2\right)\frac{4\gamma\left(h^2-a^2\right)}{\left(a^2+h^2\right)^2} + \left(P_{Ext}\left(a^2+h^2\right) + 4h\gamma\right)\frac{\pi}{2}\right)^{-1} \qquad (2.2)$$

which can be solved numerically to give bubble lifetimes (i.e., $h = 0$). P_{Ext} is the external pressure, k_H is Henry's constant, D is the diffusion coefficient, R is the gas constant, T is temperature, c_b is the gas concentration in bulk solution far from the bubble, a is the

bubble's lateral radius, and $\Phi(\theta)$ is a geometric factor for mass transport at a spherical cap ($1 \leq \Phi(\theta) \leq \pi/2$) where θ is the contact angle.[38] With this model. a value of $k_f = 1 \times 10^{-9}$ mol N^{-1} s^{-1} provides the best fit to our experimentally determined lifetimes of H_2 bubbles (dashed line, Figure 2.6). The magnitude of this kinetic constant would only have small effects on microbubble dissolution rates, because of the reduction in diffusional fluxes at large size bubbles. While the kinetic fit is not particularly compelling likely due to uncertainties in the experimental system, our results are an intriguing first estimate of interfacial gas transfer limitations at bubbles of nanometer dimensions. To the best of our knowledge, these experiments provide the first direct evaluation of interfacial gas transfer kinetic rates for bubbles less than 100 nm in size.

2.4 Conclusions

We have demonstrated a new electrochemical method for the measurement of bubble lifetimes. Studies of H_2 and N_2 nanobubbles show dissolution rates that are ~1000 times slower than predictions from extant theories assuming a diffusion-limited process. These experiments represent an extreme test case where the rate of gas transfer across an interface may not be able to maintain the high equilibrium surface concentration due to the exceedingly fast diffusion of dissolved gas away from the bubble's nanometric gas/water interface. Our results are in closer agreement to these theories than previous observations of interfacial nanobubbles via AFM and TEM. Characterization of the bubble and/or electrode sizes with other imaging techniques may bring our lifetime values in closer agreement with theoretical expectations, or will provide stronger evidence for the development and testing of new theories.

2.5 Appendix

2.5.1 Derivations of analytical expressions for bubble lifetimes

The following are descriptions of the derivations of expressions used to fit the data in Figure 2.6 of the main text, as well as the model including interfacial transfer kinetics, Equation 2.2, described in the discussion of this figure. The assumptions made in deriving these expressions are explicitly stated.

All derivations are founded upon a few similar descriptions. The bubble on a surface is assumed to take the shape of a spherical cap, and can be described by a number of different geometric parameters as is shown schematically in Figure 2.7. Elementary geometry/trigonometry gives the following interdependencies:

$$\sin(\theta) = \frac{a}{R} \tag{2.3}$$

$$R = \frac{a^2 + h^2}{2h} \tag{2.4}$$

The volume of the spherical cap, V, and surface area of the gas/liquid interface, A, are defined by

$$V = \frac{\pi}{6} h\left(3a^2 + h^2\right) \tag{2.5}$$

$$A = \pi\left(a^2 + h^2\right) \tag{2.6}$$

The pressure, P, may be described by the Laplace equation (Equation 2.7), where Equation 2.4 may be substituted in for the radius of curvature of the bubble, R,

$$P = \frac{2\gamma}{R} + P_{Ext} = \frac{4h\gamma}{a^2 + h^2} + P_{Ext} \tag{2.7}$$

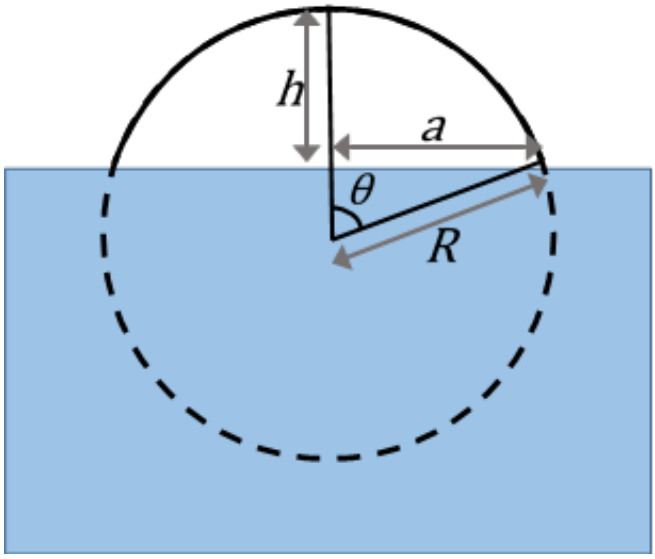

Figure 2.7. Schematic showing the geometric parameters describing the geometry of a bubble pinned on a surface.

P_{Ext} is the externally applied pressure (1 atm = 101,325 Pa) and γ is the liquid-gas surface tension (0.072 J/m^2).

The ideal gas law relates pressure, volume and temperature (T=298 K in this work) to the amount, n (moles), where R=8.31 J/(K mol).

$$PV = nRT \tag{2.8}$$

2.5.2 Zhang and Lohse model

Assumptions: We make the assumption that the bubble is pinned, i.e., a is a constant for all time. We assume that the kinetics of interfacial transfer are fast, and thus, that Henry's Law is appropriate to describe the concentration at the gas/liquid interface. Finally, we make the assumption that mass transport in solution, which we assume to be governed by diffusion only, always attains a steady-state distribution.

Derivation. For a pinned bubble, a is a constant and we can write the rate of change of amount in the bubble with time by combining Equations 2.5, 2.7 and 2.8 and using the rules of differentiation:

$$\frac{dn}{dt} = \frac{d}{dt}\left(\frac{PV}{RT}\right) = \frac{1}{RT}\left(V\frac{dP}{dt} + P\frac{dV}{dt}\right)$$

$$= \frac{1}{RT}\left(\frac{\pi}{6}h\left(3a^2+h^2\right)\frac{d}{dt}\left(\frac{4h\gamma}{a^2+h^2}+P_{Ext}\right)+\left(\frac{4h\gamma}{a^2+h^2}+P_{Ext}\right)\frac{d}{dt}\left(\frac{\pi}{6}h\left(3a^2+h^2\right)\right)\right)$$

$$\frac{dn}{dt} = \frac{dh}{dt}\frac{1}{RT}\left(\frac{\pi}{6}h\left(3a^2+h^2\right)\frac{4\gamma\left(h^2-a^2\right)}{\left(a^2+h^2\right)^2}+\left(\frac{4h\gamma}{a^2+h^2}+P_{Ext}\right)\frac{\pi}{2}\left(a^2+h^2\right)\right) \tag{2.9}$$

The bubble surface concentration, k_{surf}, may be defined by Henry's law

$$c_{surf} = k_H P \tag{2.10}$$

The flux away from the bubble is analogous to the limiting current, I, to a sphere-cap

microelectrode; a situation that was considered by Alfred and Oldham.[38] They give

$$I = 4naFDc_b\Phi(\theta) \tag{2.11}$$

$$\text{where } \Phi(\theta) = \int_0^\infty 1 - \tanh(u)\tanh\left(\frac{u(\pi-\theta)}{\pi}\right)du$$

where n is the number of electrons transferred, F Faraday's constant, c_b the bulk concentration of the species and D the diffusion coefficient (NB: variable names and the definition of angle have been adjusted to keep them consistent with this work). Dividing through by nF and replacing c_b with c_{surf} - c_b gives an expression for flux out of the bubble which, after a change of sign, can be equated with Equation 2.9 and rearranged to give:

$$\frac{dh}{dt} = -4DRT\left(k_H\left(\frac{4h\gamma}{a^2+h^2}+P_{Ext}\right)-c_b\right)a\Phi(\theta)\left(\frac{\pi}{6}h\left(3a^2+h^2\right)\frac{4\gamma\left(h^2-a^2\right)}{\left(a^2+h^2\right)^2}+\left(\frac{4h\gamma}{a^2+h^2}+P_{Ext}\right)\frac{\pi}{2}\left(a^2+h^2\right)\right)^{-1} \tag{2.12}$$

Equation 2.12 can be solved numerically – in this work we assumed the bubble to initially be hemispherical, ($h(0) = a$) and that the concentration of the gas in bulk solution is $c_b = 0$ mM for H_2 and $c_b = 0.55$ mM for N_2. Note: this result is numerically equivalent to that of Zhang and Lohse, although the constituent equations and derivation are somewhat different.

2.5.3 Modified Zhang and Lohse model

Assumptions: This derivation makes the same assumptions as the previous derivation (Zhang and Lohse) with the exceptions that interfacial (gas/liquid) transport is no longer assumed to be fast, but instead is described by a rate expression (Equation 2.13).

Derivation: The transfer at the gas-liquid interface may be described by a kinetic

expression, which necessarily should agree with Henry's law (Equation 2.10) when at equilibrium. Assuming first order kinetics, which is reasonable as we are considering a unimolecular reaction, we have, J, the flux out of the bubble at every point as

$$J = Pk_f - k_b c_{surf} \tag{2.13}$$

At equilibrium J=0 and Henry's law (Equation 2.10) holds, which gives that $k_b=k_f/k_H$. We make the assumption that the flux is uniform over the entire surface of the bubble. Equating fluxes by combining Equations 2.11 and 2.12 we get

$$Pk_f - k_b c_{surf} = 4D\left(c_{surf} - c_b\right)a\Phi(\theta)/A \tag{2.14}$$

Which we may rearrange to give the surface concentration

$$c_{surf} = \left(Pk_H + \frac{4Dc_b a k_H \Phi(\theta)}{Ak_f}\right) \Bigg/ \left(1 + \frac{4Da k_H \Phi(\theta)}{Ak_f}\right) \tag{2.15}$$

As expected, reduces to Henry's law (Equation 2.10) for large values of k_f, as the second terms in both the numerator and denominator tend to zero.

We substitute the surface concentration from Equation 2.14 into Equation 2.11 and, as with the previous derivation, equate with Equation 2.9, to give the differential equation describing the growth/dissolution of the bubble

$$\frac{dh}{dt} = -4DRT\left(\left(\left(P_{Ext} + \frac{4h\gamma}{a^2+h^2}\right)k_H + \frac{4Dc_b a k_H \Phi(\theta)}{\pi\left(a^2+h^2\right)k_f}\right) \Bigg/ \left(1 + \frac{4Da k_H \Phi(\theta)}{\pi\left(a^2+h^2\right)k_f}\right) - c_b\right)a\Phi(\theta)$$

$$\left(\frac{\pi}{6}h\left(3a^2+h^2\right)\frac{4\gamma\left(h^2-a^2\right)}{\left(a^2+h^2\right)^2} + \left(P_{Ext}\left(a^2+h^2\right) + 4h\gamma\right)\frac{\pi}{2}\right)^{-1} \tag{2.16}$$

which can be solved numerically using the initial conditions/parameter values as for the initial model.

2.5.4 Epstein-Plesset for a hemispherical bubble

Assumptions: We assume that the bubble always maintains a hemispherical shape, that is h=a=R, during the entire period of dissolution. We assume that the surface concentration is defined by Henry's law (Equation 2.10).

We make the observation that the situation described is no different to that of an isolated (spherical) stationary bubble in solution; as in both cases there is no flux across an equatorial plane. The dissolution/growth of an isolated bubble in solution has previously been addressed by Epstein and Plesset[12] and also Ljunggren and Eriksson.[13] The latter derived the equation

$$a^2(t) = a^2(0) - 3RTDt/k_H \tag{2.16}$$

to describe the bubble radius as a function of time, which gives a zero bubble radius at

$$t^* = a^2(0)k_H/3RTD \tag{2.17}$$

2.6 References

(1) Parker, J. L.; Claesson, P. M.; Attard, P. Bubbles, Cavities, and the Long-Ranged Attraction Between Hydrophobic Surfaces. *J Phys Chem*, *98*, 8468–8480, (1994).

(2) Carambassis, A.; Jonker, L.; Attard, P.; Rutland, M. Forces Measured Between Hydrophobic Surfaces Due to a Submicroscopic Bridging Bubble. *Phys Rev Lett*, *80*, 5357–5360, (1998).

(3) Poynor, A.; Hong, L.; Robinson, I.; Granick, S.; Zhang, Z.; Fenter, P. How Water Meets a Hydrophobic Surface. *Phys Rev Lett*, *97*, 266101, (2006).

(4) Doshi, D. A.; Watkins, E. B.; Israelachvili, J. N.; Majewski, J. Reduced Water Density at Hydrophobic Surfaces: Effect of Dissolved Gases. *Proc Natl Acad Sci U.S.A.*, *102*, 9458–9462, (2005).

(5) Meyer, E. E.; Rosenberg, K. J.; Israelachvili, J. Recent Progress in Understanding Hydrophobic Interactions. *Proc Natl Acad Sci U.S.A.*, *103*, 15739–15746, (2006).

(6) German, S. R.; Wu, X.; An, H.; Craig, V. S. J.; Mega, T. L.; Zhang, X. Interfacial

Nanobubbles Are Leaky: Permeability of the Gas/Water Interface. *ACS Nano*, *8*, 6193–6201, (2014).

(7) Zhang, X.; Khan, A.; Ducker, W. A Nanoscale Gas State. *Phys Rev Lett*, *98*, 136101, (2007).

(8) Seo, D.; German, S. R.; Mega, T. L. Phase State of Interfacial Nanobubbles. *J Phys Chem C*, 119, 14262–14266, (2015).

(9) Zhang, X. Quartz Crystal Microbalance Study of the Interfacial Nanobubbles. *Phys. Chem. Chem. Phys.*, *10*, 6842–6848, (2008).

(10) Borkent, B.; Dammer, S.; Schönherr, H. Superstability of Surface Nanobubbles. *Phys Rev Lett*, *98*, 204502, (2007).

(11) Zhang, X. H.; Quinn, A.; Ducker, W. A. Nanobubbles at the Interface Between Water and a Hydrophobic Solid. *Langmuir*, *24*, 4756–4764, (2008).

(12) Epstein, P. S.; Plesset, M. S. On the Stability of Gas Bubbles in Liquid-Gas Solutions. *J Chem Phys*, *18*, 1505–1509, (1950).

(13) Ljunggren, S.; Eriksson, J. C. The Lifetime of a Colloid-Sized Gas Bubble in Water and the Cause of the Hydrophobic Attraction. *Colloid Surf A*, *129-130*, 151–155, (1997).

(14) Ducker, W. Contact Angle and Stability of Interfacial Nanobubbles. *Langmuir*, *25*, 8907, (2009).

(15) Seddon, J. R. T.; Zandvliet, H. J. W.; Lohse, D. Knudsen Gas Provides Nanobubble Stability. *Phys Rev Lett*, *107*, 116101, (2011).

(16) Peng, H.; Hampton, M. A.; Nguyen, A. V. Nanobubbles Do Not Sit Alone at the Solid–Liquid Interface. *Langmuir*, *29*, 6123–6130, (2013).

(17) Lu, Y.-H.; Yang, C.-W.; Hwang, I.-S. Molecular Layer of Gaslike Domains at a Hydrophobic-Water Interface Observed by Frequency-Modulation Atomic Force Microscopy. *Langmuir*, *28*, 12691–12695, (2012).

(18) Zhang, X.; Chan, D. Y. C.; Wang, D.; Maeda, N. Stability of Interfacial Nanobubbles. *Langmuir*, *29*, 1017–1023, (2013).

(19) Lohse, D.; Zhang, X. Pinning and Gas Oversaturation Imply Stable Single Surface Nanobubbles. *Phys Rev E,* (2015).

(20) Liu, Y.; Zhang, X. A Unified Mechanism for the Stability of Surface Nanobubbles: Contact Line Pinning and Supersaturation. *J Chem Phys*, *141*, 134702, (2014).

(21) Zhang, X. H.; Li, G.; Maeda, N.; Hu, J. Removal of Induced Nanobubbles From Water/Graphite Interfaces by Partial Degassing. *Langmuir*, *22*, 9238–9243, (2006).

(22) Zhang, X.; Zhang, X.; Lou, S.; Zhang, Z.; Sun, J.; Hu, J. Degassing and Temperature Effects on the Formation of Nanobubbles at the Mica/Water Interface. *Langmuir*, *20*, 3813–3815, (2004).

(23) Duncan, P. B.; Needham, D. Test of the Epstein−Plesset Model for Gas Microparticle Dissolution in Aqueous Media: Effect of Surface Tension and Gas Undersaturation in Solution. *Langmuir*, *20*, 2567–2578, (2004).

(24) Berge, L. I. Dissolution of Air Bubbles by the Resistive Pulse and the Pressure Reversal Technique. *J Colloid Interface Sci*, *134*, 548–562, (1990).

(25) Shin, D.; Park, J. B.; Kim, Y.-J.; Kim, S. J.; Kang, J. H.; Lee, B.; Cho, S.-P.; Hong, B. H.; Novoselov, K. S. Growth Dynamics and Gas Transport Mechanism of Nanobubbles in Graphene Liquid Cells. *Nature Communications*, *6*, 1–6, (2015).

(26) Zhang, L.; Zhang, Y.; Zhang, X.; Li, Z.; Shen, G.; Ye, M.; Fan, C.; Fang, H.; Hu, J. Electrochemically Controlled Formation and Growth of Hydrogen Nanobubbles. *Langmuir*, *22*, 8109–8113, (2006).

(27) Dapkus, K. V.; Sides, P. J. Nucleation of Electrolytically Evolved Hydrogen at an Ideally Smooth Electrode. *J Colloid Interface Sci*, *111*, 133–151, (1986).

(28) Fernández, D.; Maurer, P.; Martine, M.; Coey, J. M. D.; Möbius, M. E. Bubble Formation at a Gas-Evolving Microelectrode. *Langmuir*, 30, 13065-74, (2014).

(29) Luo, L.; White, H. S. Electrogeneration of Single Nanobubbles at Sub-50-Nm-Radius Platinum Nanodisk Electrodes. *Langmuir*, *29*, 11169–11175, (2013).

(30) Chen, Q.; Luo, L.; Faraji, H.; Feldberg, S. W.; White, H. S. Electrochemical Measurements of Single H_2 Nanobubble Nucleation and Stability at Pt Nanoelectrodes. *J Phys Chem Lett*, *5*, 3539–3544, (2014).

(31) Chen, Q.; Luo, L.; White, H. S. Electrochemical Generation of a Hydrogen Bubble at a Recessed Platinum Nanopore Electrode. *Langmuir*, *31*, 4573–4581, (2015).

(32) Chen, Q.; Wiedenroth, H. S.; German, S. R.; White, H. S. Electrochemical Nucleation of Stable N_2 Nanobubbles at Pt Nanoelectrodes. *J Am Chem Soc*, *137*, 12064–12069, (2015).

(33) Zhang, B.; Galusha, J.; Shiozawa, P. G.; Wang, G.; Bergren, A. J.; Jones, R. M.; White, R. J.; Ervin, E. N.; Cauley, C. C.; White, H. S. Bench-Top Method for Fabricating Glass-Sealed Nanodisk Electrodes, Glass Nanopore Electrodes, and Glass Nanopore Membranes of Controlled Size. *Anal Chem*, *79*, 4778–4787, (2007).

(34) Kuwana, T.; Bublitz, D. E.; Hoh, G. Chronopotentiometric Studies on the Oxidation of Ferrocene, Ruthenocene, Osmocene and Some of Their Derivatives. *J Am Chem Soc*, 82, 5811-5817, (1960).

(35) Amatore, C. "Basic Concepts." *Organic Electrochemistry, Fifth Edition* CRC Press, **2015.**

(36) Mazarei, A. F.; Sandall, O. C. Diffusion Coefficients for Helium, Hydrogen, and Carbon Dioxide in Water at 25°C. AIChE J., 26, 154−157, (1980).

(37) Cussler, E. L. *Diffusion: Mass Transfer in Fluid Systems*; 2nd ed.;Cambridge University Press: New York, (1997).

(38) Alfred, L.; Oldham, K. B. Steady-State Currents at Sphere-Cap Microelectrodes and Electrodes of Related Geometry. *J Phys Chem* (1996).

CHAPTER 3

ESTIMATING THE CRITICAL SIZE OF BUBBLE-FORMING NUCLEI FOR GAS-EVOLVING ELECTRODE REACTIONS

Reproduced with permission from

German, S. R.; Edwards, M.A.; Chen, Q.; Liu, Y.; Luo, L.; White, H. S.

Faraday Discuss. 2016, 193, 223-240.

3.1 Introduction

In this chapter, a fundamental question is addressed: "What is the critical size of a single cluster of gas molecules that grows and becomes a stable (or continuously growing) gas bubble during gas evolving reactions?" Electrochemical reactions that produce dissolved gas molecules are ubiquitous in electrochemical technologies, *e.g.*, water electrolysis, photoelectrochemistry, chlorine production, corrosion, and often lead to the formation of gaseous bubbles. Herein, we demonstrate that electrochemical measurements of the dissolved gas concentration, at the instant prior to nucleation of an individual nanobubble of H_2, N_2, or O_2 at a Pt nanodisk electrode, can be analyzed using classical thermodynamic relationships (Henry's Law and the Young-Laplace equation – including

non-ideality) to provide an estimate of the size of the gas bubble nucleus that grows into a stable bubble. We further demonstrate that this critical nucleus size is independent of the radius of the Pt nanodisk employed (< 100 nm radius), and weakly dependent on the nature of the gas. For example, the measured critical surface concentration of H_2 of ~0.23 M *at the instant of bubble formation* corresponds to a critical H_2 nucleus that has a radius of ~3.6 nm, an internal pressure of ~350 atm, and contains ~1,700 H_2 molecules. The data are consistent with stochastic fluctuations in the density of dissolved gas, at or near the Pt/solution interface, controlling the rate of bubble nucleation. We discuss the growth of the nucleus as a diffusion-limited process and how that process is affected by proximity to an electrode producing ~10^{11} gas molecules per second. Our study demonstrates the advantages of studying a single-entity, *i.e.*, an individual nanobubble, in understanding and quantifying complex physicochemical phenomena.

The spontaneous phase transformation required to initiate bubble formation is a highly activated process requiring extreme conditions to proceed. Classical nucleation theory (CNT) describes this activation barrier to create a bubble nucleus in terms of the cohesive force of the liquid, while assuming a critical nucleus is large enough that it can be described by bulk thermodynamics.[1-4] CNT applies equally to single component systems, where a vapor bubble is generated by single component boiling,[5,6] as well as binary mixtures, where a dissolved gas phase separates into a bubble;[7-10] these two systems differ predominantly in their growth/dissolution dynamics. Vapor bubbles in single component systems are at all instances surrounded by their comprising material and are often violent in their dynamics, such as with cavitation.[5] Diffusional gradients control the growth of bubbles formed from dissolved gas. In this work we report on nucleation of

single gas bubbles from a supersaturated binary mixture induced by electrogeneration of dissolved gas at a nanoelectrode.

The free energy of formation of a gas bubble nucleus in solution, $\Delta G_{tot,}$ is the sum of the energy cost of creating the new interface and that gained through liberation of dissolved gas into the bubble volume. Figure 3.1 (top) schematically presents the classic description of ΔG_{tot} as a function of the bubble's radius, r_{nb}. The free energy attributable to the gas/solution interface, $\Delta G_{surf} = 4\pi\gamma r_{nb}^2$ (dashed line, where γ is surface energy of the gas/solution interface), is proportional to the area of the bubble's interface. The bulk component term, ΔG_{bulk}, (dotted line, $4\pi/3\ \Delta G_V r_{nb}^3$) is proportional to the volume of the bubble and $\Delta G_{V,}$ the energy difference between the dissolved and gaseous state of the molecules in that volume. ΔG_{tot} is the sum of these two components,

$$\Delta G_{tot} = 4\pi\gamma r_{nb}^2 + 4\pi/3\ \Delta G_V r_{nb}^3 \qquad (3.1)$$

From Eqn (3.1), ΔG_{tot} initially increases as a function of r_{nb} before reaching a maximum, E_a, at a critical radius, r_{crit}. The implication of this free energy maximum is that a bubble of radius greater than r_{crit} is energetically favored to continue to grow, whereas bubbles with radii less than r_{crit} are inclined to shrink. However, since bubbles of critical size necessarily arise from the growth of sub-critical nuclei, their formation relies upon relatively improbable fluctuations along the free energy barrier.

A bubble of critical radius is both in mechanical and chemical equilibrium with the dissolved gas. The Young-Laplace equation (eqn (3.2)) describes the pressure difference across the gas/solution interface, $\Delta P_{Y\text{-}L} = P_{internal} - P_{ambient}$, where $P_{internal}$ and $P_{ambient}$ are the total pressure within the bubble and the ambient pressure, respectively. For a bubble of radius r_{crit}

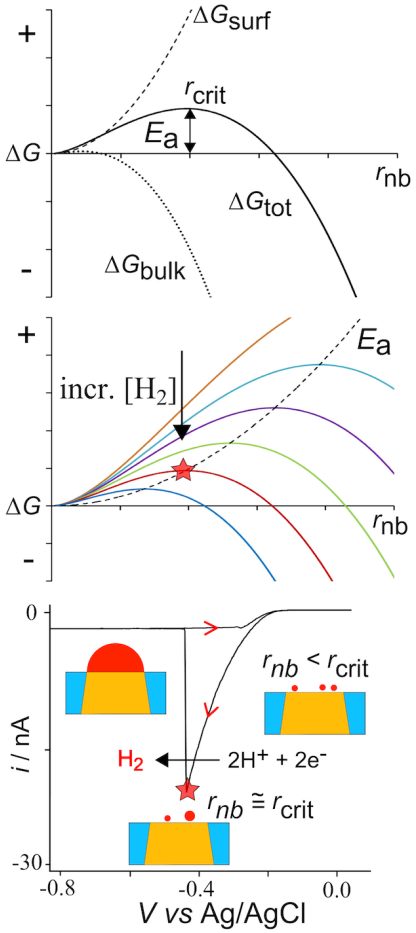

Figure 3.1. *Top*. Plot of total free energy of formation of a gas bubble nucleus, $\Delta G_{tot} = \Delta G_{surf} + \Delta G_{bulk}$, *vs.* the radius of the nanobubble, r_{nb}. The maximum in ΔG_{tot} corresponds to the critical nanobubble radius, r_{crit}, with an activation energy barrier of E_a. For a bubble nucleus of radius greater than r_{crit}, the continued growth of the nucleus into a stable bubble is energetically favorable. *Middle*. Plots of ΔG_{tot} vs r_{nb} at different concentrations of dissolved H_2 (*i.e.* different supersaturations). Lower values of $[H_2]$ are associated with higher values of E_a, (indicated by the dashed line), reducing the probability of bubble formation. Increasing $[H_2]$ decreases the activation energy such that thermal fluctuations may nucleate a bubble of critical radius, as depicted by the red star for an arbitrary H_2 concentration. *Bottom*. Cyclic voltammogram for H^+ reduction in 0.5 M H_2SO_4 at a 33 nm radius Pt nanodisk electrode (500 mV/s). The peak (red star) corresponds to a phase change as a nucleus grows into a stable nanobubble covering the electrode. Inlaid schematics show the spontaneous formation of nuclei near the surface of the electrode. At sufficiently high H_2 supersaturation, a nucleus of critical size exists, which grows into a bubble covering the electrode. Note: while the schematic shows nucleation as a homogenous process occurring just above the electrode, we also consider the possibility of heterogeneous nucleation on the electrode surface (see discussion).

$$\Delta P_{Y\text{-}L} = 2\gamma / r_{crit} \,. \qquad (3.2)$$

Large positive values of $\Delta P_{Y\text{-}L}$ tend to drive gas molecules out of sub-critical bubbles into the solution, resulting in bubble shrinkage. The bubble's internal hydrostatic pressure ($\Delta P_{Y\text{-}L} + P_{ambient}$) can be countered when the partial pressure of the dissolved gas, P_{gas}, is equal to the bubble's internal pressure. For any specific supersaturation of dissolved gas, $P_{gas} - P_{ambient}$, there is a corresponding E_a that is required for formation of a continuously growing bubble. As shown in the middle plot of Figure 3.1, a critical bubble size is associated uniquely with a specific E_a and supersaturation. At low supersaturations, the value of E_a is sufficiently large such that nuclei are unlikely to reach r_{crit} and grow into stable bubbles. Conversely, large supersaturations serve to lower r_{crit} such that thermal fluctuations of the magnitude of E_a may occur at an appreciable rate.

We recently reported on the formation of single bubbles of H_2, N_2, and O_2 at the surface of Pt nanoelectrodes that are created by electrogeneration of large gas supersaturations at the electrode/electrolyte interface.[11-15] The lower frame of Figure 3.1 shows an example cyclic voltammogram for the formation of a single H_2 bubble. In this experiment, H^+ reduction at a 33 nm radius Pt nanoelectrode in 0.5 M H_2SO_4 is used to drive H_2 production. On the initial sweep of the *i-E* curve, the current for H_2 electrogeneration increases when the electrode potential, *E*, is scanned to potentials negative of the formal potential for H^+ reduction ($E^0_{H+/H2}$ = -0.23 *V* vs Ag/AgCl). As the potential is scanned to more negative values, the current and rate of H_2 electrogeneration continue to increase nearly exponentially until there is an abrupt drop in the current to a non-zero residual current that is nearly independent of *E*. The abrupt drop defines the peak current, i^p_{nb}, that coincides with the formation of a stable nanobubble on the surface of the

electrode.[12] The bubble, which covers the electrode surface, significantly diminishes the rate of H^+ reduction of at the electrode, the latter occurring along the circumference of the bubble at the Pt/gas/electrolyte interface.[11] In this specific voltammogram, the formation of a single bubble occurs at ~-0.4 V as indicated by the sudden drop in current magnitude from i_{nb}^{p} ~20 nA to ~3 nA. The bubble is only stable as long as the potential is held sufficiently negative of ~-0.3 V, such that the constant production of H_2 at the electrode replenishes the H_2 that dissolves from the bubble into solution. As the potential is swept back towards positive potentials, the current for H^+ reduction decays and the bubble rapidly dissolves.[15] Note, throughout this work, our analysis does not require knowledge of the precise mechanism of the gas evolving electrode reactions, only that such reactions produce gas as described by well-known stoichiometric reactions, *e.g.*, $2H^+ + 2e^- \rightarrow H_2$.

At the foot of the voltammetric wave, the rate of H_2 generation is low, and thus the amount of dissolved H_2 is also correspondingly low. Based on the above description, we expect that the transient H_2 bubble nuclei, schematically shown in the insets of Figure 3.1, are smaller than the corresponding r_{crit}, and thus are unstable and dissolve rapidly. As the current is swept to more negative potentials, the concentration (*i.e.*, supersaturation) of dissolved H_2 in the vicinity of the electrode increases and r_{crit} decreases until the probability of a nucleus of radius approaching or exceeding r_{crit} becomes sufficiently large. At this electrode potential, continued growth of a nucleus leading to a stable bubble is thermodynamically favorable. This critical point coincides with the red star on each of the graphs. While the thermodynamics suggest that the bubble will continue to grow *ad infinitum,* its growth is self-limited at the Pt disk edges, which acts as the source of H_2 for its growth.[11] A stable bubble is established in a dynamic equilibrium when the rate of H_2

dissolution and electrogeneration are equal.

Herein, we show that the value of the peak current recorded at the instant prior to formation of a single, stable bubble is proportional to the electrode size, with a constant of proportionality that depends on the identity of the gas. For H_2, N_2, and O_2, the current corresponds to a critical supersaturation of dissolved gas, above which a phase transformation immediately proceeds. Our voltammetric results indicate a sharp threshold from immeasurably slow to extremely fast nucleation rates. The critical supersaturation is a direct measure of the chemical potential of gas within the critical bubble nucleus, allowing calculation of the critical nucleus pressure and radius, as well as the number of constituent gas molecules contained within the nucleus.

3.2 Experimental Methods

3.2.1 Nanoelectrode fabrication and characterization

Nanoelectrodes were fabricated as previously reported.[16] Briefly, the end of a 25 μm Pt wire was sharpened by etching in 6 M sodium cyanide, the wire attached to a tungsten rod, and the sharp end sealed in a glass capillary in a H_2/air flame. The glass was then polished on silicon carbide sandpaper (400/1200 grit Buehler) until a Pt nanodisk was exposed, as indicated by an electronic feedback circuit. The electrochemically-apparent electrode radius , a, was determined by measurement of the steady-state diffusion-limited current for ferrocene oxidation in an acetonitrile solution containing 0.1 M tetrabutylammonium hexafluorophosphate ($TBAPF_6$). Radii were calculated using[17]

$$i_{\text{lim}} = 4nFD_{\text{Fc}}C^{*}a \tag{3.3}$$

where n is the number of electrons transferred (=1 for Fc), F is Faraday's constant (=96485

C/mol), D_{Fc} (2.5 x 10^5 cm^2/s)[18] and C^* are the diffusion coefficient and bulk concentration of ferrocene (5 mM), respectively.

3.2.2 Materials and data acquisition

Sulfuric acid, hydrazine, and CTAB (Sigma Aldrich) were used as received. Ferrocene was purified by sublimation. A Dagan Cornerstone Chem-Clamp and a Pine RDE4 (used as a waveform generator) were interfaced with a PCI data acquisition card (National Instruments) to perform voltammetry.

3.3 Results and Discussion

3.3.1 Critical concentration

Figure 3.2 shows typical voltammograms for electrochemical reactions at Pt nanoelectrodes that correspond to the formation of stable individual nanobubbles of H_2, N_2, and O_2. Each voltammogram displays a similar shape to that for H_2 nanobubble formation shown in Figure 3.1; however, the values of potentials and currents are different for the different gases. In each case we expect the bubble to form from a critically sized nucleus, although the critical radius for each gas will differ due to the distinct chemical properties of the gases. The peak current i_{nb}^{p} just prior to bubble formation is labeled on each voltammogram. In all cases, i_{nb}^{p} is *reproducible between cycles* and is nearly *independent of the scan rate* up to ~10 V/s.

The reproducibility of i_{nb}^{p} and insensitivity to scan rate suggests a very sharp threshold over which the probability of a nucleus having radius greater than r_{crit} changes

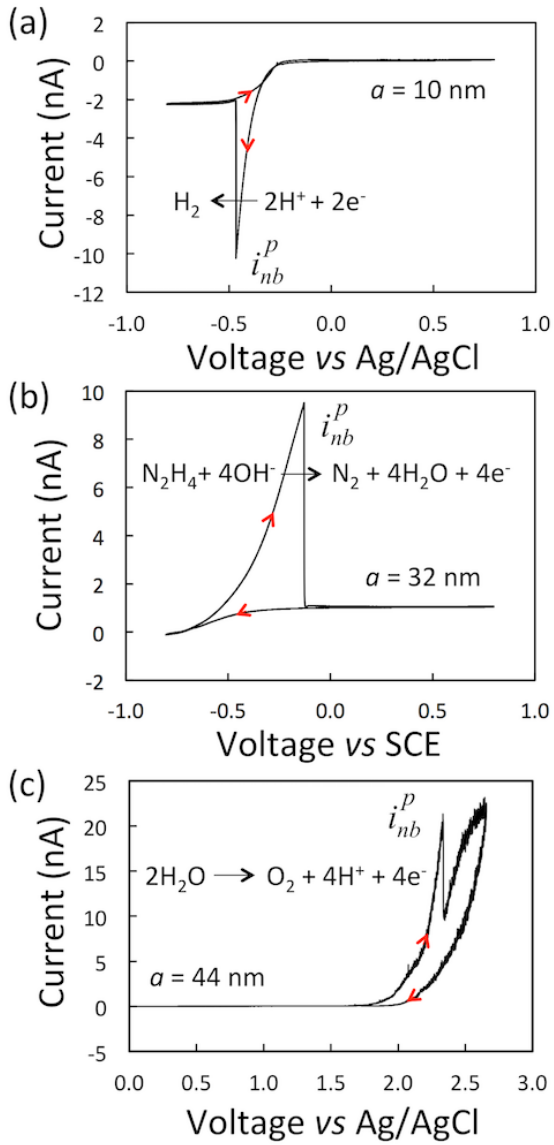

Figure 3.2. Voltammograms corresponding to H_2, N_2, and O_2 bubble formation at Pt nanoelectrodes. The gas-evolving electrode reactions are displayed on the figure. The electrode radii, *a,* indicated on each plot were determined from the steady-state diffusion-limited current of ferrocene oxidation in acetonitrile. The aqueous solutions contained: (a) 0.5 M H_2SO_4, (b) 1 M N_2H_4, and (c) 0.25 M H_2SO_4.

from essentially zero to unity, and bubble formation immediately proceeds. If the threshold were more gradual, one would expect variability in i_{nb}^{p}. Similarly, if the formation of a bubble nucleus were a slow event on the voltammetric timescale, one might expect an increase in the peak current at increasing scan rates.

The rate of critical bubble formation is a function of the activation energy (indicated in Figure 3.1) by the Arrhenius equation $J = Z \exp(-E_a/kT)$. For homogeneous nucleation, J has been shown to be a steep function of γ and supersaturation $(P_{gas} - P_{ambient})$[7]

$$J = Z \exp\left(\frac{-16\pi\gamma^3}{3kT(P_{gas} - P_{ambient})^2}\right) \tag{3.4}$$

where J (m^{-3} s^{-1}) is the rate of critical bubble formation, the exponential prefactor, Z, can be treated as a constant, k is Boltzmann's constant, and T is temperature. For nucleation of bubbles from dissolved gas in solution, in general, there is wide disagreement between experiment and theory, with nucleation often occurring at supersaturation levels that are orders of magnitude lower than predicted by eqn (3.4). [10,19-22] A large body of literature presents a variety of explanations for the observed discrepancy, ranging from new thermodynamic interpretations of surface tension of small nuclei, [6,23] to impinging cosmic rays,[24] to pre-existing stable nuclei.[19] Our current data does not allow speculation about nucleation rates aside from the observation that the rate appears to vary from extremely slow to very fast over a small voltage range (~5 mV), corresponding to a small change in the dissolved gas concentration.

The majority of studies of nucleation in the literature similarly report a supersaturation value at which J is appreciably fast. There are three types of approach that have been employed to measure the critical supersaturation at which bubble formation is

observed: homogenous gas-producing chemical reaction in bulk solution,[21,23,25,26] release of pressure after equilibrium is reached at elevated pressure[27,28] and electrochemical gas generation.[20,29] Lubetkin has compiled the results of a large number of these reports and points out that these measurements often reflect kinetic limitations and not true thermodynamic values.[30]

In the context of nucleation rates, i_{nb}^{p} represents a point in the *J vs.* supersaturation curve where bubble formation occurs quickly relative to the rate of change in gas supersaturation. For instance, at a 1 V/s scan rate, bubble nucleation reproducibly occurs within an ~5 mV range. The voltage range, ΔV, is related to the characteristic time of a physicochemical process to the scan rate, ν, by $\tau = \Delta V/\nu$, meaning at least one critical bubble forms at that dissolved gas supersaturation in the volume near the electrode *at least* every ~5 ms, corresponding to a minimum nucleation frequency of 200 s^{-1}.

Figure 3.3 shows the dependence of i_{nb}^{p} for N_2 bubble formation on the radius of the Pt nanodisk, *a*. The upper part of the figure shows voltammograms recorded in aqueous 1 M N_2H_4 at Pt nanoelectrodes of 10, 23, 47, and 80 nm radius, and at a scan rate of 200 mV/s. It is apparent from these plots that i_{nb}^{p} increases as a function of the electrode size. The lower part of Figure 3.3 shows that i_{nb}^{p} is a linear function of *a* for the nucleation of H_2, N_2 and O_2 bubbles ($R^2 > 0.97$ in all cases). The solid lines in this plot represent least squares fits to the data that pass through the origin with slopes of 0.81 ± 0.02 nA/nm, 0.48 ± 0.03 nA/nm and 0.31 ± 0.01 nA/nm for H_2, O_2 and N_2, respectively.

The steady-state current at a nanodisk electrode, while typically written in terms of the bulk concentration of the reactants, can also be written as a function of the surface concentration of electrogenerated dissolved gas, C_{surf}. Assuming zero concentration of this

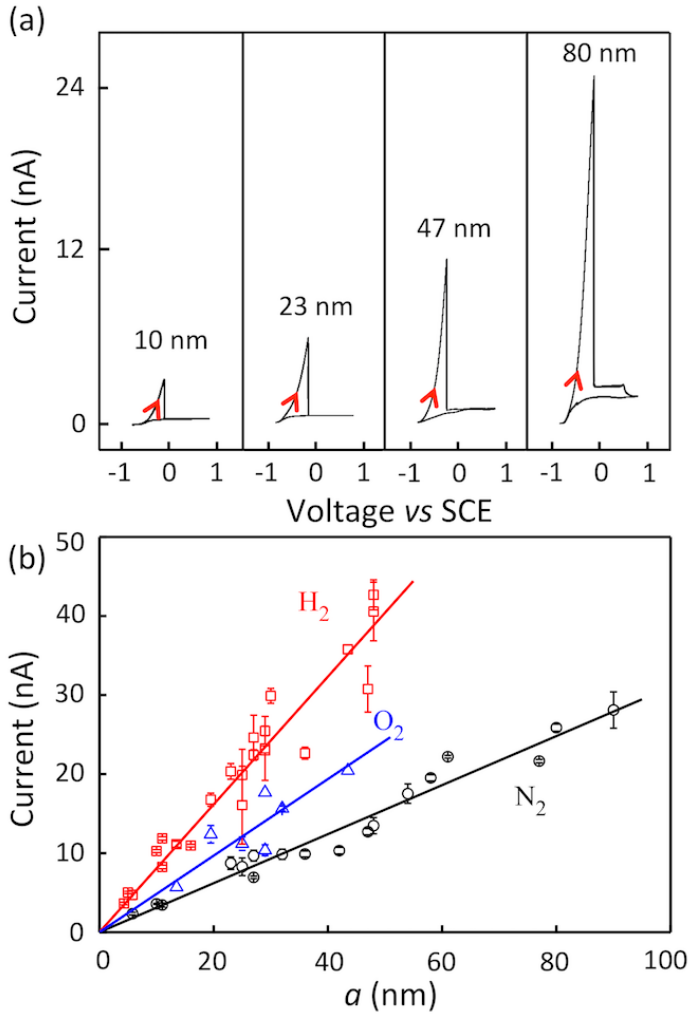

Figure 3.3. Top: Voltammetry corresponding to the formation of stable N_2 bubbles at different sizes of Pt nanoelectrodes (labeled) in 1 M N_2H_4. Bottom: Plot of the i_{nb}^{p} as a function of the electrode radius, a, for H_2, N_2, and O_2. Lines are least squares best fits to the average i_{nb}^{p} of each electrode with the intercept fixed at zero. Similar data were originally presented in ref. 12-14.

gas in bulk solution, the relation between current and C_{surf} is given by:[17]

$$i = 4naFDC_{surf} \tag{3.5}$$

where D is the diffusion coefficient of the gas in solution and n the number of electrons transferred in the reaction (n = 2 for H_2, 4 for N_2, and 4 for O_2). Rearranging this equation, and setting i to i_{nb}^{p} allows one to obtain the critical concentration of dissolved gas at the electrode surface at the moment that a dynamically stable bubble is nucleated.

$$C_{crit} = i_{nb}^{p} / 4naFD \tag{3.6}$$

Because the plots of i_{nb}^{p} *vs.* a in Figure 3.3 are linear, we conclude that C_{crit} is independent of the electrode size and can be calculated from eqn (3.6). Values of C_{crit} for H_2, N_2 and O_2 are tabulated in Table 3.1, with errors determined from the variance in linear fits and uncertainty in the value of D (see Appendix for details). From the value of $C_{crit,}$ we are able to derive a number of properties of the critical nucleus, which are also listed in Table 3.1, and which are discussed below.

3.3.2 Critical nucleus parameters

The Laplace pressure of a critical nucleus is directly related to C_{crit} by the partial pressure of the dissolved gas ($P_{gas} = \Delta P_{Y\text{-}L} + P_{ambient}$). This relationship is given in a rudimentary way using Henry's Law ($K_H P_{gas} = C$),

$$\Delta P_{Y\text{-}L} = (C_{crit}/K_H) - P_{ambient} \tag{3.7}$$

where K_H is 0.78 mM/atm for H_2 in pure water at 25 °C.[32] For the measured C_{crit} = 0.23 M, eqn (3.7) yields $\Delta P_{Y\text{-}L}$ = 290 atm. The Laplace pressure is a thermodynamic quantity, which is related, through the surface tension, γ, to the bubble radius of curvature, *i.e.*, the critical bubble radius, by eqn (3.2). Using the macroscopic surface tension of 0.5 M H_2SO_4 at

Table 3.1. Parameters describing the critical nuclei for H_2, N_2, and O_2 bubble generation.

	H_2		**H_2 + surfactant**		**N_2**		**O_2**	
C_{crit} (M)	0.23 ± 0 .02		0.14 ± 0.02		0.09 ± 0.02		0.14 ± 0.01	
	Ideal	**Corrected**	**Ideal**	**Corrected**	**Ideal**	**Corrected**	**Ideal**	**Corrected**
$\Delta P_{Y\text{-}L}$ (atm)	290 ± 30[a]	350 ± 30[b]	180 ± 30	210 ± 30	140 ± 30	160 ± 40	100 ± 10	120 ± 10
r_{crit} (nm)	4.9 ± 0.6[c]	3.6 ± 0.3[d]	4.1 ± 0.8	3.5 ± 0.6[e]	10 ± 3	7.9 ± 1.6	14 ± 2	10 ± 1
n_{crit}[f]	3500 ± 900	1700 ± 300	1300 ± 500	900 ± 300	15000 ± 9000	8100 ± 2500	28000 ± 9000	12000 ± 3000

(*a*) Pressure difference calculated directly from Henry's Law at 25°C and 1 atm in pure water ($\Delta P_{Y\text{-}L} = C_{crit}/K_H$ -1)
(*b*) Pressure difference corrected using experimental gas solubility at high pressure in pure water and accounting for electrolyte reduction of solubility, see Appendix, eqn (3.14)
(*c*) Calculated using the ideal $\Delta P_{Y\text{-}L}$ and surface tension of the air/solution interface at 1 atm
(*d*) Calculated using corrected $\Delta P_{Y\text{-}L}$ and modification of the surface tension by surface adsorption of gas at high pressures, see Appendix
(*e*) Calculated using the surface tension of the air/solution interface at 1 atm, see Appendix
(*f*) Calculated from in-column r_{crit} and $\Delta P_{Y\text{-}L}$ and the ideal gas law (eqn (3.8)) for a spherical bubble. *Recent measurements of nucleation rates unpublished at the time of submission of this dissertation indicate a heterogeneous mechanism for nucleation of H_2 bubbles. The low contact angle for the nucleus (as measured through the bubble) reduces the volume to ~1/100 that of a sphere and reduces the calculated n accordingly. The calculated r_{crit} is independent of mechanism.*

ambient temperature and pressure (0.072 N/m)[33] as a simple estimation of γ, we calculate the value of $r_{crit} = 4.9$ nm. From this we compute the number of molecules, n, in the critical nucleus using the ideal gas law, assuming a spherical nucleus of volume $4/3\pi r_{crit}^3$.

$$n = (\Delta P_{Y\text{-}L} + P_{ambient})\, 4\pi\, r_{crit}^3/3RT \qquad (3.8)$$

For the 4.9 nm radius critical H_2 nucleus, formed at 1 atm and 298K, the total internal pressure is 291 atm, and the critical nucleus contains ~3,500 H_2 molecules.

The thermodynamic relations used above provide a straightforward means to estimate parameters describing the critical bubble nucleus and are listed as ideal values in Table 3.1. Better estimates of $\Delta P_{Y\text{-}L}$, r_{crit}, and n can be obtained by consideration of known non-idealities at high pressures. The corrected values in Table 3.1 are based on reported measurements of gas solubility in pure water at high pressure, the reduction of gas solubility by electrolyte at ambient pressures (*i.e.*, 'salting out'), and reduction of surface tension by gas adsorption at high pressure. These corrections are detailed in the Appendix. Another consideration is that the surface tension is a function of the interfacial radius of curvature for very small bubbles.[34] The size at which the effect becomes important is highly debated. However, experimental studies of capillary condensation have shown the surface tension of water and cyclohexane droplets as small as ~5 nm to be very nearly that of the bulk.[35,36] Thus, the possible dependence of γ on bubble radius is ignored here. It is expected from classical nucleation theory that a solution/gas interface with lower surface tension will have a significantly lower value of ΔG_{surf} and hence a lower value of E_a for the spontaneous formation of a critical nucleus, Figure 3.1. However, both Rubin *et al.* [21] and Hemmingsen[27] observed only marginally lower critical values for nitrogen supersaturation induced by a chemical reaction and argon supersaturation induced by pressure release,

respectively, in the presence of surfactant, and argued that the surfactant concentration in the bulk was too low to affect homogeneous nucleation. To test this idea, we investigated the effect of surfactant on the H_2 system. Figure 3.4 demonstrates the influence of adding CTAB to the solution on the value of i_{nb}^{p}. The voltammograms show the formation of a H_2 bubble in 0.5 M H_2SO_4, recorded at the same 22 nm radius electrode with and without 0.2 mg/mL CTAB (cetyltrimethylammonium bromide) surfactant. We observe an ~40% reduction of i_{nb}^{p} in the presence of surfactant that is reproducible with different electrodes indicating that nucleation proceeds at a lower critical supersaturation of H_2. This finding is consistent with a critical bubble in the presence of CTAB having a lower internal pressure. The results suggest that the lifetime of a sub-critical radius nucleus, as it grows to critical size, is long enough for surfactant to adsorb to its surface. While both gas and surfactant adsorption reduce surface tension, it has been shown that the two components are not additive. Rather, the two components are in competition for available surface area.[37] Thus, for the CTAB data, in contrast to the other experiments, we do not account for gas adsorption in the corrected value of r_{crit} reported in Table 3.1.

3.3.3 Effect of proximity to an electrode

The supersaturation pressure values corresponding to a nucleation event at our Pt electrodes range between 100 and 350 atm and are dependent upon gas type. These values are as high as the highest reported values listed by Lubetkin[30] and the magnitude of supersaturation and ordering by gas type $O_2 < N_2$ (H_2 not studied) agrees approximately with Hemmingsen,[27] who visually observed bubble formation after release of pressure to ambient conditions. In comparison to the decompression method, our results are more

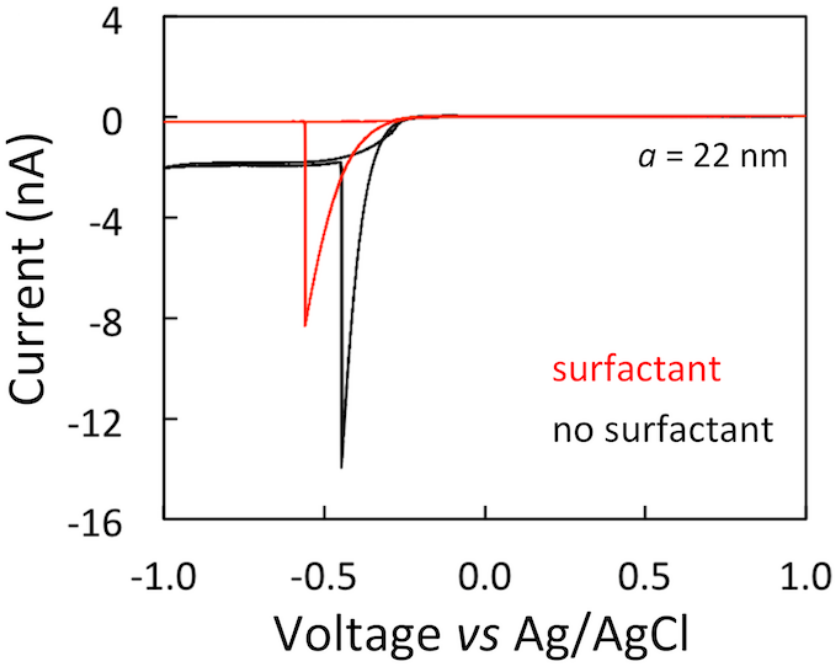

Figure 3.4. *i-V* responses from a 22 nm radius Pt electrode in 0.5 M H_2SO_4 with (red) and without 0.2 mg/mL CTAB surfactant (black). Scan rate 100 mV/s.

quantitative and the electrochemical method is less cumbersome. Our measured critical supersaturation values are an order of magnitude higher than other reports of electrochemically induced supersaturation. Dapkus and Sides[20] attributed the relative ease of nucleation in their electrochemical system to a reduction of surface tension by the large electric field within the double layer at the electrode surface. Here we do not speculate on electric field effects; however, in the following section, we do consider how bubble nucleation might be influenced by proximity to a gas-evolving surface.

The results presented in Table 3.1 indicate at least a few thousand molecules need to spontaneously assemble to form a critical bubble with r_{crit} between ~4 and ~10 nm. In the case of H_2, this process occurs at a C_{crit} of ~0.23 M. If we consider a homogeneous solution containing 0.23 M H_2, the requisite number of molecules to form a critical bubble (n = 1,700) is found within a spherical volume of solution having a radius of 14 nm. A bubble nucleus will deplete the surrounding solution of dissolved gas as it grows, relying upon diffusion of H_2 to the growing bubble. Random diffusion of thousands of molecules to a growing bubble within this volume is an unlikely event. However, in our experiment, the Pt nanoelectrodes can support an immense rate of H_2 generation due to the high catalytic rate for H^+ reduction at Pt, as well as the high convergent flux of H^+ to the nanoscale electrode. For instance, a typical 16 nA peak current at a 20 nm radius electrode corresponds to the production of ~10^{11} H_2/s and represents the generation of the 10^3 molecules to create a bubble of critical nucleus size every ~3 nanoseconds. Thus a growing sub-critical bubble nucleus near the Pt nanoelectrode will not deplete the local concentration of dissolved gas, and its growth will thus not likely be transport limited.

We performed steady-state finite element simulations to gain further insight into

the flux and concentration distributions of H_2 around a bubble nucleus at an electrode. Mass transport of H_2 in solution and its exchange at the bubble-solution interface were modeled in these simulations (detailed description in Appendix). The results are shown in Figure 3.5 for three bubble nuclei of radius that are, respectively, smaller, larger and nearly equal to the value of r_{crit} = 4.9 nm reported in Table 3.1. In each simulation, the bubble is situated 1 nm above a 20 nm radius electrode that generates a uniform surface flux of H_2 equivalent to the current experimentally observed at i_{nb}^{o} (16.2 nA). The concentration of H_2 is represented by color (red = high concentration, blue = low concentration); its value at the surface of the bubble is fixed to that given by Henry's Law and the bubble's internal pressure (eqn (3.7)). The streamlines represent H_2 flux, from which we can observe that H_2 generated at the electrode underneath the bubble flows into the bubble, whereas the H_2 generated at the electrode far from the bubble diffuses into bulk solution. The arrows at the bubble-solution interface represent H_2 flux vectors across the interface; the results in Figure 3.5 indicate that H_2 enters the bottom of the bubble that is close to the electrode surface, and exits through the top surface of the bubble. The magnitudes of these fluxes are quite different for the different sized nuclei. The smallest bubble nucleus (r_{nb} = 4 nm), which has the highest internal pressure, has larger H_2 fluxes out of the top of the nucleus and smaller fluxes into its lower side, due to the higher surface concentration. Overall, this gives a net outward flow of H_2, and hence this nucleus will tend to shrink. In contrast, for the largest bubble (r_{nb} = 7 nm), the lower internal pressure generates a lower surface concentration and the net flux of H_2 is into the bubble; *i.e.,* this is a growing bubble. The net inward flux (7.1 fmol/s integrated over the bubble surface) is such that enough gas enters the bubble to grow it to a hemisphere the size of the electrode in only 7.1 μs. The 5.6 nm bubble

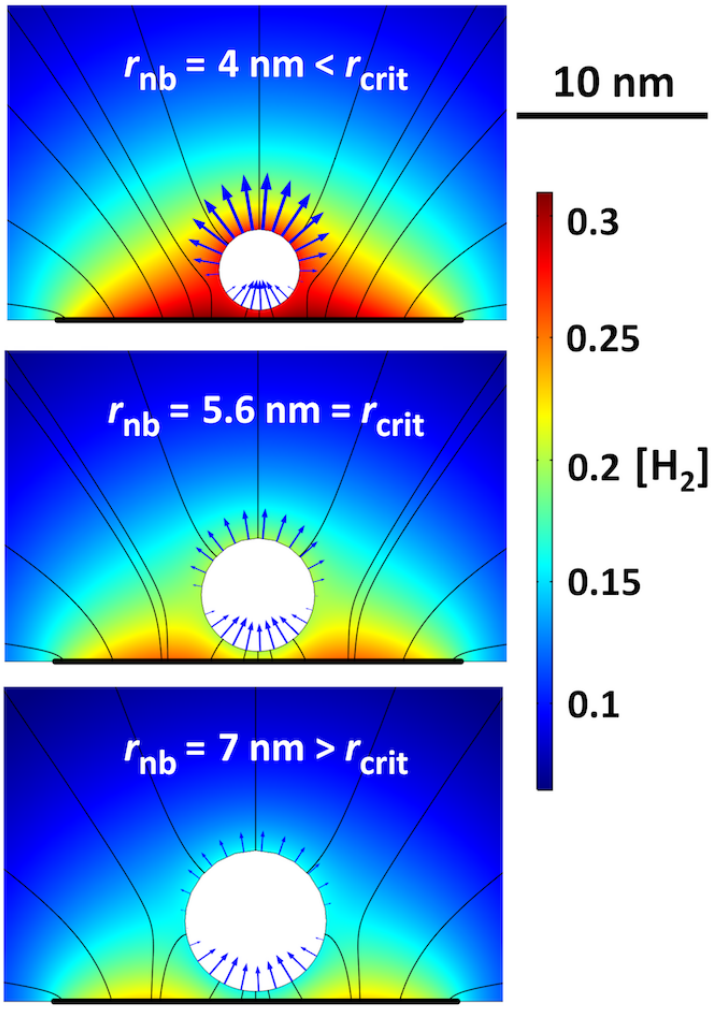

Figure 3.5. Finite element simulations of bubble nuclei one nanometer above a 20 nm radius Pt electrode. 4, 5.6, and 7 nm radius are simulated under conditions in which 5.6 nm is the critical radius. Streamlines represent H_2 flow away from the electrode and vectors show the flux across the bubble surface.

corresponds to a size where the H_2 fluxes into and out of the bubble, through the lower and upper surfaces, are nearly perfectly balanced; however, any perturbation would cause it to either grow or shrink. Note that this size bubble is slightly larger than $r_{crit} = 4.9$ nm reported in Table 3.1.

For simplicity, the nucleus was fixed 1 nm from the electrode center in the simulations; however, moving the nucleus horizontally or vertically only subtly affects the calculated values and not the qualitative conclusion that the proximity of the electrode provides a sufficient supply of the gas to support the rapid growth of the bubble. Moreover, simulations with the different gases show similar flux distributions, although the exact concentrations/critical sizes depend on the gas. As the simulations were performed at steady state, they do not capture the time dependence; however, they do reflect the expected location of fluxes. (NB: the use of steady-state simulations accounts for the anomalously high concentration observed around the 4 nm bubble, which, rather than constantly generating H_2 while maintaining its size, would actually be shrinking.)

The mechanisms described above consider homogeneous nucleation occurring in bulk solution in the sense that the volume to surface area relationship of the bubble nuclei is fixed by the radius. However, nucleation might be a pseudo-homogeneous process in that bubble growth is a surface mediated process whereby the constituent gas is delivered over a short diffusive distance. Heterogeneous nucleation could of course be involved, in which a sphere cap nucleus is formed on a portion of the electrode. Our derivation of r_{crit}, which began with the experimentally measured C_{crit}, does not require the bubble being a complete sphere. Hence the critical radius for nucleation we calculate is independent of mechanism. In addition, the critical radius is unaffected by the kinetic limitation of gas

transfer discussed in Chapter 2, because Henry's Law still determines the equilibrium relation. Measuring a rate for k_f simply defines a k_b that satisfies Henry's Law constant. However, for heterogeneous nucleation, the surface area to volume relationship becomes defined by the contact angle of the sphere cap on the Pt surface. The barrier for heterogeneous nucleation is lower compared to homogeneous nucleation because fewer molecules are required and the surface energy cost is lower. If heterogeneous nucleation is occurring in our system, surface adsorption of the bubble nucleus to the electrode would likely need to be directed by hydrophobic surface contaminants. Surface roughness would also be variable from electrode to electrode and consequently the critical concentration would be expected to be less reproducible between electrodes than our results perhaps suggest. However, we cannot discount this possibility.

Recent measurements of nucleation rates as a function of H_2 supersaturation, unpublished at the time of submission of this dissertation, indicate a heterogeneous mechanism for nucleation. Low contact angles for bubble nuclei significantly reduce the critical number of gas molecules. As such, the dependence upon gas type could further be explained by the electrode/gas/liquid surface energies that affect the contact angle of bubble nuclei. Moreover, the electrode surface is in different states at the voltages where bubble formation occurs in the different reactions (i.e., PtH for H_2 and varying proportions of Pt/PtO for both N_2 and O_2), which also affects the nucleus contact angle. Further studies of nucleation rates for other gas types may reveal different contact angles for different bubble nuclei of different composition.

3.4 Conclusions

In this report, we have demonstrated that the study of single gas bubbles at nanodisk electrodes allows precise quantitative evaluation of key parameters describing bubble nucleation. Specifically, analysis of the voltammetric peak currents at the instant preceding stable bubble formation provide the size, internal pressure, and number of gas molecules of the critical size nucleus that grows into a stable bubble. For H_2, O_2 and N_2, we find that the critical nuclei have a radius between 4 and 10 nm, a pressure of 100 to 350 atm, and contain between 2000 and 10,000 molecules, with the variation arising from a number of physiochemical parameters of the gas (*e.g.*, diffusion coefficient, gas solubility, surface tension, etc.). The origin of the largest uncertainty in these values arises from the uncertainty in the gas diffusivity in electrolyte solution, as well as potential unknown limitations of applying thermodynamic relationships at nanoscale length scales for single entities (*i.e.*, individual gas nanobubbles).

Our current investigations do not shed significant insight into the frequency of transient bubble formation and collapse prior to the formation of a nucleus with radius > r_{crit} that grows into a dynamically stable bubble. The voltammetric data place a lower bound of ~200 s^{-1} for nuclei generation when the electrode is held at a potential in immediate vicinity of the nucleation potential. We are currently exploring measurements on single bubble experiments to estimate nucleation rates for gas bubbles, and these studies will be communicated in a future report.

3.5 Appendix

3.5.1 Description of finite element simulations

The concentrations and fluxes of H_2 presented in Figure 3.5 were calculated by numerically solving the equations describing diffusion of H_2 and its transfer at the bubble-solution interface. Boundary conditions were chosen to match those of experiments with a 20 nm radius electrode in 0.5 M H_2SO_4 at the experimentally determined i_{nb}^{p} (= 16.2 nA) and for a range of bubble nuclei sizes. The lower edge of the bubble was placed 1 nm above the nanoelectrode center, as shown in Figure 3.6.

Mass transfer was described by the steady-state diffusion equation (eqn (3.9)) within the axially symmetric domain shown in Figure 3.6.

$$0 = D_{H_2} \nabla^2 c \tag{3.9}$$

Here, D_{H2} (=4.5x10^{-5} cm^2/s)[38] and c are the diffusion coefficient and concentration of H_2, respectively. The concentration at the bulk boundary was taken to match that of the experimental conditions, that is

$$c_{H_2} = 0\, M \tag{3.10}$$

There is no flux of H_2 into, or out of, the glass surround of the nanoelectrode, as described by

$$0 = D_{H_2} \nabla c \cdot \vec{n} \tag{3.11}$$

where $\vec{n}$ is the inward pointing unit normal to the surface.

On the surface of the bubble, we assume that the gas transfer kinetics are infinitely fast, *i.e.*, always at equilibrium. We use the Young-Laplace equation (eqn (3.6)) to describe the internal pressure and Henry's Law to determine its equilibrium concentration. The bubble surface concentration of H_2 is thus described by:

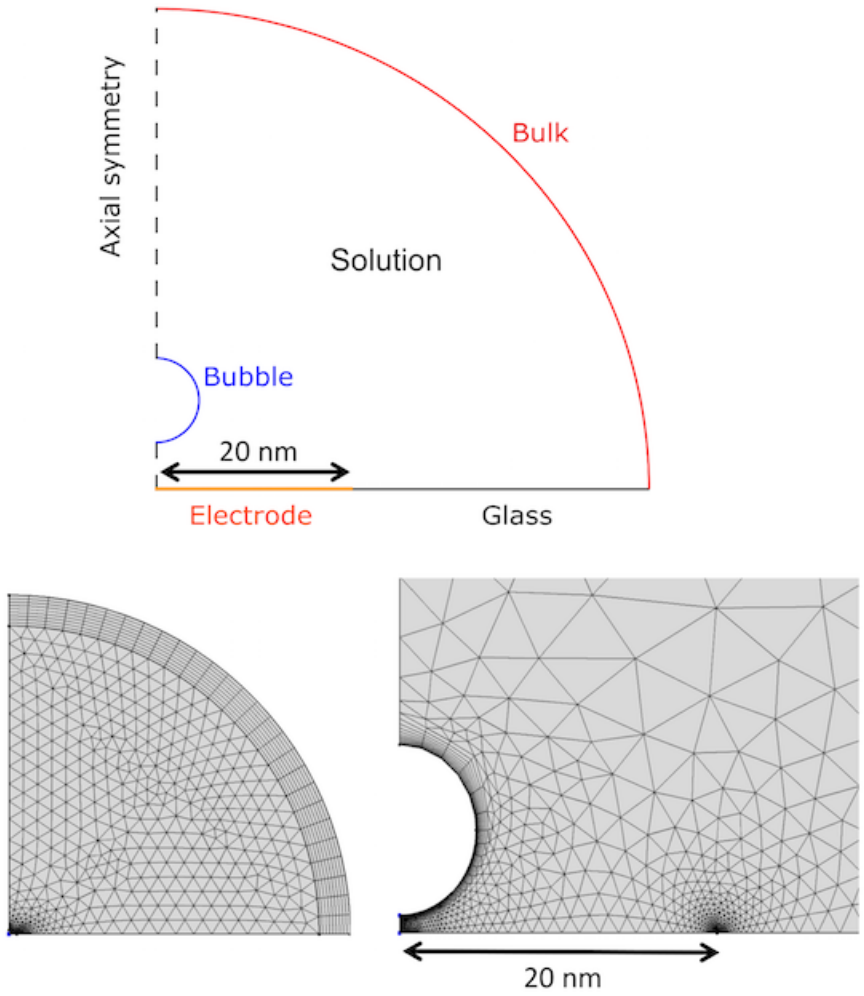

Figure 3.6. Geometry (not to scale) and mesh for finite element simulations of a bubble nucleus above a nanoelectrode.

$$c_{H_2} = k_H\left(P_{Ext} + \frac{2\gamma}{r_{nb}}\right). \tag{3.12}$$

The boundary condition on the electrode was matched to the experimentally determined current (i_{nb}^{p} = 16.2 nA, for r_{elec} = 20 nm) such that the H_2 flux is distributed evenly across the electrode surface, which is a reasonable assumption for a kinetically limited reaction, *i.e.,* at moderate electrode overpotentials.

$$\frac{-i_{nb}^{p}}{2F\pi a^2} = D_{H_2}\nabla c \cdot \vec{n} \tag{3.13}$$

Solution of eqn (3.9) was achieved using the commercial finite element package COMSOL Multiphysics (version 5.2). The mesh, which was heavily refined on the boundary between the glass and the Pt and the bubble surface, is shown in Figure 3.6.

The "infinite elements" coordinate transform was used to map the outer region (quadrilateral mesh in Figure 3.6) to infinity to rule out any influence of a finitely sized domain of simulation.

3.5.2 Calculation of parameters for critical nuclei

Table 3.2 lists diffusion coefficients for H_2, N_2, and O_2 in water from different literature reports. In evaluation of C_{crit} from the i_{nb}^{p} *vs. a* slopes in Figure 3.3, the diffusion coefficients for each gas were averaged and the extrema were used to estimate the uncertainty in *D*.

The ideal values in Table 3.1 in the main text are calculated using straightforward classical thermodynamic relationships (see main text). Henry's Law is the most well studied reference point for gas solubility. At 25°C and 1 atm, K_{H} is 0.78, 0.69, and 1.39 mM for H_2, N_2, and O_2 in pure water, respectively.[32,41,42] However, calculation of the

Table 3.2. List of diffusion coefficients found in the literature for each gas type.

	H_2	**N_2**	**O_2**
Diffusivity (10^{-5} cm^2/s) at 25 °C [38]	4.50	1.88	2.10
Diffusivity (10^{-5} cm^2/s) at 20 °C [39]	4.25	2.00	2.30
Diffusivity (10^{-5} cm^2/s) at 20 °C [40]	5.0	2.6	2.3
Average ± extremum (10^{-5} cm^2/s)	4.58 ± 0.33	2.16 ± 0.44	2.23 ± 0.13

values using Henry's Law implicitly assumes that gas solubility increases linearly with increasing pressure. Empirical measurements of gas solubility in pure water at extreme pressures are available in the literature and report significant deviation from the linear approximation.[32,43,44] Figure 3.7 compares the linear approximation with the empirical data. The pressure at which the equilibrium solubility matches our measured C_{crit} is a more accurate partial pressure, which we denote by $P_{gas}(C_{crit})$.

From the data presented in Figure 3.7 we obtain the pressure in equilibrium with the critical concentration for H_2 (C_{crit} = 0.23 M), as $P_{gas}(C_{crit})$ = 310 atm, slightly larger than the ideal value, 290 atm, calculated with the Henry's law (linear) approximation. An additional correction concerns the electrolyte's effect on dissolved gas solubility ("salting out"). As no measurements of this effect are available at high pressure, we assume that the fractional change is the same at all pressures. Thus this is included through multiplying $P_{gas}(C_{crit})$ by the ratio of equilibrium solubility at 1 atm in pure water and with electrolyte present. The corrected value for $\Delta P_{Y\text{-}L}$, which is reported in Table 3.1 as 'corrected', is given by

$$\Delta P_{Y\text{-}L} = P_{gas}(C_{crit})\, K_H(\text{water})/K_H(\text{electrolyte}) - P_{ambient} \qquad (3.14)$$

For instance, the Henry's Law constant for H_2 in 0.5 M H_2SO_4 is 89% of the value in pure water (both at 1 atm); [45] consequently, our measured C_{crit} represents a higher $\Delta P_{Y\text{-}L}$ of 350 atm. Experimental studies of gas solubility in the electrolyte solutions employed in this study would allow us to further refine these approximations

Additionally, it is not expected that the surface tension of a bubble nucleus is equal to that of the air/solution interface at atmospheric pressure. At high pressures, gases are known to adsorb to the gas/solution interface, reducing the surface tension to different

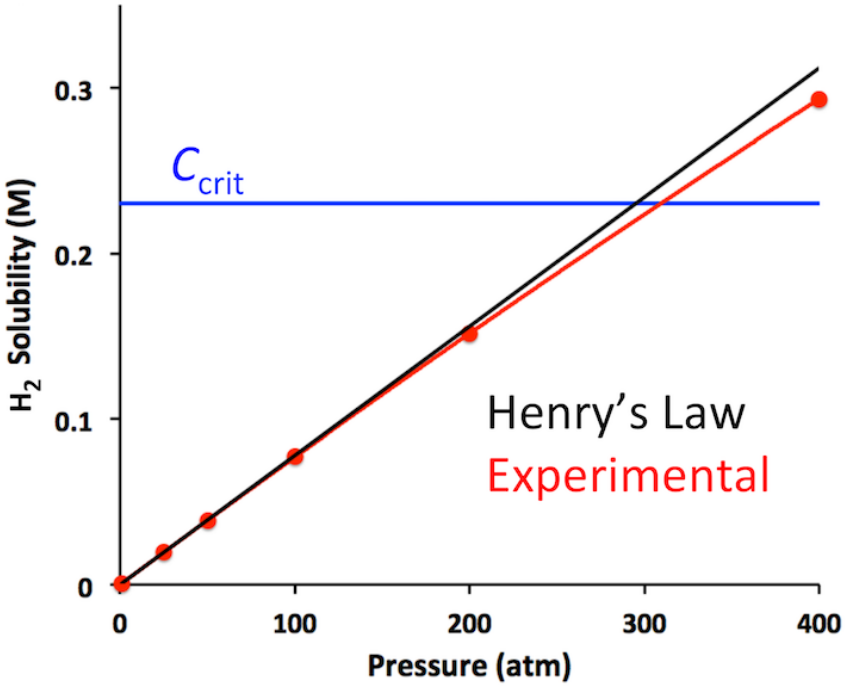

Figure 3.7. Plot of experimental values (red) of H_2 solubility at high pressures from Wiebe et al.[32] Compared with Henry's Law linear approximation.

extents according to their polarizability. Depending on the gas and the pressure within the critical nucleus, the reduction in surface tension can be significant and would proportionally lower the estimated r_{crit}. For the gases in this study, the order of increasing positive gas adsorption to the interface has been empirically measured as $H_2 < O_2 < N_2$.[46]

Measurements of the surface tension of gas/water interfaces were reported up to 80 atm. Polynomial fits to the data are provided in the form $\gamma = \gamma_0 + BP + CP^2$ where γ_0 (dyn/cm) is the surface tension at 1 atm, P is the applied pressure, and B and C are the fit parameters. Values for B and C were reported as -0.0250 and 0, -0.0835 and 0.000194, and -0.0779 and 0.000104 for H_2, N_2, and O_2, respectively. Values of 72 and 73 dyn/cm were used for γ_0 for the H_2SO_4 and N_2H_4 solutions, respectively, [33,47] giving corrected values for γ of 63, 65, and 64 dyn/cm for H_2, N_2, and O_2, respectively. Note, as stated in the main text, as the influence of the surfactant (CTAB) cannot easily be combined with that of the gas altering the surface tension, we used the surface tension at 1 atm in all cases ($\gamma = 37$ dyn/cm).[48] From these surface tensions and the corrected pressure we derived the corrected values of r_{crit} displayed in Table 3.1, from which the number of molecules in the critical nucleus, n_{crit}, were deduced using the ideal gas law (eqn (3.7)), with the corrected pressure.

3.6 References

1 M. Volmer and A. Weber, *Z. Phys. Chem.,* 1926, **119**, 277.

2 R. Becker and W. Doring, *Ann. Phys.*, 1935, **24**, 719.

3 J. Frenkel, *Kinetic Theory of Liquids*, Dover, New York, 1955.

4 Y. B. Zeldovich, *Acta Physicochim. URSS,* 1943, **18**, 1.

5 M. S. Plesset and A. Prosperetti, *Annu. Rev. Fluid Mech*., 1977, **9**, 145.

6 V. K. Shen and P. G. Debenedetti, *J. Chem. Phys.*, 2003, **118**, 768.

7 V. Talanquer and D. W. Oxtoby, *J. Chem. Phys*. 1995, **102**, 2156.

8 S. Goldman, *J. Phys. Chem. B*. 2008, **112**, 16701.

9 M. Blander and J. L. Katz, *AIChE J.* 1975, **21**, 833.

10 C. Ward, A. Balakrishnan, and F. C. Hooper, *Trans. ASME*, 1970, **92**, 695.

11 L. Luo and H. S. White, *Langmuir*, 2013, **29**, 11169.

12 Q. Chen, L. Luo, H. Faraji, S. W. Feldberg, and H. S. White, *J. Phys. Chem. Lett.*, 2014, **5**, 3539.

13 Q. Chen, H. S. Wiedenroth, S. R. German, and H. S. White, *J. Am. Chem. Soc.*, 2015, **137**, 12064.

14 Q. Chen, L. Luo, and H. S. White, *Langmuir*, 2015, **31**, 4573.

15 S. R. German, Q. Chen, M. A. Edwards, and H. S. White, *J. Electrochem. Soc.*, 2016, **163**, 3160.

16 B. Zhang, J. Galusha, P. G. Shiozawa, G. Wang, A. J. Bergren, R. M. Jones, R. J. White, E. N. Ervin, C. C. Cauley, and H.S. White, *Anal. Chem*., 2007, **79**, 4778.

17 A. J. Bard and L. R. Faulkner *Electrochemical Methods: Fundamentals and Applications*, John Wiley and Sons, New York, 2001.

18 T. Kuwana, D. E. Bublitz, and G. Hoh, *J. Am. Chem. Soc*., 1960, **82**, 5811.

19 E. N. Harvey, D. K. Barnes, W. D. McElroy, A. H. Whiteley, D. C. Pease, *J. Am. Chem. Soc*., 1945, **67**, 156.

20 K. V. Dapkus and P. J. Sides, *J. Colloid Interface Sci*., 1986, **111**, 133.

21 M. B. Rubin and R. M. Noyes, *J. Phys. Chem*., 1992, **96**, 993.

22 P. M. Wilt, *J. Colloid Interface Sci*., 1986, **112**, 530.

23 P. G. Bowers, K. Bar-Eli, and R. M. Noyes, *J. Chem. Soc., Faraday Trans*., 1996, **92**, 2843.

24 D. Sette and F. Wanderlingh, *Phys. Rev*., 1962, **125**, 409.

25 Y. Mori, K. Hijikata, and T. Nagatani, *Int. J. Heat Mass Transfer*, 1976, **19**, 1153.

26 M. J. Hey, A. M. Hilton, and R. D. Bee, *Food Chem*., 1994, **51**, 349.

27 E. A. Hemmingsen, *J. Appl. Phys*., 1975, **46**, 213.

28 S. Jones, G. Evans, and K. Galvin, *Adv. Colloid Interface Sci*., 1999, **80**, 27.

29 D. E. Westerheide and J. W. Westwater, *AIChE J.*, 1961, **7**, 357.

30 S. Lubetkin, *Langmuir*, 2003, **19**, 2575.

31 A. J. Bard and L. R. Faulkner *Electrochemical Methods: Fundamentals and Applications*, John Wiley and Sons, New York, 2001.

32 R. Wiebe, V. L. Gaddy, and C. Heins Jr, *Ind. Eng. Chem*., 1932, **24**, 823.

33 R. M. Suggitt, P. M. Aziz and F. Wetmore, *J. Am. Chem. Soc.,* 1949, **71**, 676.

34 R. C. Tolman, *J. Chem. Phys*. 1949, **17**, 333.

35 M. M. Kohonen and H. K. Christenson, *Langmuir*, 2000, **16**, 7285.

36 L. R. Fisher and J. N. Israelachvili, *Nature*, 1979, **277**, 548.

37 C. Jho and A. D. King Jr., *J. Colloid Interface Sci.*, 1979, **69**, 529.

38 E. L. Cussler, *Diffusion: Mass Transfer in Fluid Sustems*, Cambridge University Press, New York, 1997.

39 P. T. H. M. Verhallen, L. J. P. Oomen, A. J. J. M. v. d. Elsen, and J. Kruger, *Chem. Eng. Sci*., 1984, **39**, 1535.

40 D. L. Wise and G. Houghton, *Chem. Eng. Sci*, 1966, **21**, 999.

41 R. Battino, T. R. Rettich and T. Tominaga, *J. Phys. Chem. Ref. Data*, 1983, **12**, 163.

42 R. Battino, T. R. Rettich and T. Tominaga, *J. Phys. Chem. Ref. Data*, 1984, **13**, 563.

43 V. I. Baranenko, V. S. Sysoev, L. N. Falkovskii, V. S. Kirov, I. Piontkovskii, and A. N. Musienko, *At. Energy*, 1990, **68**, 162.

44 M. Geng and Z. Duan, *Geochim. Cosmochim. Acta*, 2010, **74**, 5631.

45 P. Ruetschi and R. F. Amlie, *J. Phys. Chem*. 1966, **70**, 718.

46 R. Massoudi and A. D. King Jr, *J. Phys. Chem.*, 1974, **78**, 2262.

47 N. B. Baker and E. C. Gilbert, *J. Am. Chem. Soc.*, 1940, **62**, 2479.

48 Z. Adamczyk, G. Para, and P. Warszynski, *Langmuir*, 1999, **15**, 8383.

CHAPTER 4

LAPLACE PRESSURE OF INDIVIDUAL H_2 NANOBUBBLES FROM PRESSURE-ADDITION ELECTROCHEMISTRY

Adapted with permission from

German, S. R.; Edwards, M. A.; Chen, Q.; White, H. S.

Nano Lett., 2016, 16, 6691-6694

4.1 Introduction

The Young-Laplace equation is central to the thermodynamic description of liquids with highly curved interfaces, e.g., nanoscale droplets and their inverse, nanoscale bubbles. The equation relates the pressure difference across an interface to its surface tension and radius of curvature, but the validity in using the macroscopic surface tension for describing curved interfaces with radii smaller than tens of nanometers has been questioned. Here we present electrochemical measurement of Laplace pressures within single H_2 bubbles between 7 and 200 nm radius (corresponding, respectively, to between 200 and 7 atmospheres). Our results demonstrate a linear relationship between a bubble's Laplace pressure and its reciprocal radius, verifying the classical thermodynamic description of H_2

nanobubbles as small as ~10 nm.

The pressure difference across a curved liquid interface with surface tension, γ, and radius of curvature, R, is described by the well-known Young-Laplace equation, $\Delta P = 2\gamma/R$. This equation was first introduced more than 200 years ago to explain meniscus rise in capillaries, and has become the basis of classical nucleation theory,[1] Ostwald ripening,[2] capillary adhesion,[3] and capillary condensation.[4]

Classical thermodynamics treats an interface as a mathematical surface with no mass or volume and the density change across it as a step function. The molecular view of an interface is one of a density gradient, or thickness, of the interfacial layer. The insensitivity of surface tension with respect to curvature holds only so long as the thickness of the inhomogeneous layer is small compared with the radius of curvature.[5] There is no widespread agreement on the length scale at which the effect of curvature on surface tension becomes important. The problem has been addressed by simulation and thermodynamic interpretations with different authors placing the critical radius at widely differing values spanning a few Ångströms to tens of nanometers.[5-10] Measurements made at atmospheric pressures of the negative interfacial curvature of water and cyclohexane droplets suspended between mica surfaces suggest that the Kelvin equation holds for liquid droplets with radii between 5-50 nm.[11,12] Spherical gas bubbles with interfacial curvature in this same spatial domain, however, are predicted to have extraordinarly high internal pressures (tens to hundreds of atmospheres), and their thermodynamic properties have not been directly probed by experiment. Herein, we report an electrochemical experiment that allows for the direct determination of the Laplace pressure and surface tension of individual H_2 nanobubbles as small as 7 nm radius. Our results suggest that the Young-Laplace

equation provides a remarkably accurate description of the high internal pressures of very small bubbles.

4.2 Experimental Methods

4.2.1 Electrode fabrication

Quartz capillaries O.D. 1 mm I.D. 0.3 mm (Sutter Instrument #Q100-30-7.5) and 25 μm diameter Pt wire (Alfa Aesar) were rinsed in acetone followed by water and dried in a 100 °C oven. A ~1 inch length of Pt wire was placed in the center of the quartz capillary and the capillary was placed in a P-2000 Laser Puller (Sutter Instrument). Clamps were placed to prevent puller movement during heating cycles and vacuum was applied to both ends of the capillary for 5 minutes prior to heating. Three 45-second heating cycles were performed with puller parameters HEAT 690 FILAMENT 4 found to be above the quartz melting temperature and below the Pt melting temperature. This step serves to seal the quartz to the Pt wire. For the pulling step, clamps were removed from puller arms and the vacuum tubing was removed. Puller parameters were set to HEAT 710 FILAMENT 1 VELOCITY 45 DELAY 128 PULL 220. This step serves to melt the quartz and pull the quartz-platinum composite thinning it until it separates into two conical, quartz-encased Pt wires that terminate with nanometer dimensions. Inspection of each quartz-Pt assembly was then performed with light microscopy to ensure the platinum wire was continuous with no breaks. Approximately half of the assemblies did not pass this inspection. Electrical contact was made with the Pt wire by painting one end of a 0.010 inch diameter tungsten rod (A-M Systems) with silver epoxy (Alfa Aesar) and inserting it into the open end of the quartz capillary and curing in an oven at 100°C for ~1 hour.

Pt nanodisk electrodes were then exposed using focused ion beam milling (FIB). First, the assemblies were coated in a 20 nm thick layer of carbon using a Denton Discovery 18. The assemblies were then mounted vertically with conductive carbon tape, such that the tungsten rod was touching the grounded stage of the Helios Nanolab 650. FIB milling was performed using a gallium ion beam perpendicular to the capillary axis to expose a circular cross section of platinum at the center of the quartz shank. The electrode was then imaged *in situ* by scanning electron microscopy (SEM). The Pt wire was continuous and exhibited electrochemistry at the Pt nanodisk in approximately 10% of the milled electrodes while the rest likely were discontinuous due to microscopic breaks in the Pt wire that were not visualized by light microscopy inspection.

4.2.2 Electrode characterization

In the process of handling the electrodes, the Pt disk becomes recessed below the planar quartz surface. The depth of this recession, d, was calculated by measuring the steady-state diffusion-limited current for the oxidation of 5 mM ferrocene dissolved in acetonitrile containing 0.1 M tetrabutylammonium hexafluorophosphate ($TBAPF_6$). The radius of the opening at the quartz surface, a, and the half cone angle, θ, of the quartz shank are known from SEM images (θ is approximately 1° for all electrodes in this study). Thus we can use the equation for the limiting current at disk electrode in a conical pore (eq 4.1),[13] to solve for the unknown depth of recession.

$$i_{lim} = 4nFDaC^* [(1 + (d/a) \tan \theta)/(4d/a\pi + (1 + (d/a) \tan \theta))] \quad (4.1)$$

In this equation, n is the number of electrons transferred per molecule (= 1 for ferrocene), F is Faraday's constant (96485 C/mol), D is the diffusion coefficient of ferrocene (2.5 x

10^{-5} cm^2/s),[14] and C^* is the bulk concentration of ferrocene.

4.2.3 *i-V* measurements

Electrochemical measurements were performed using a Chem-Clamp potentiostat (Dagan corporation). A Pine RDE4 was used as the waveform generator and the current and voltage were recorded using a data acquisition card (National Instruments PCI-6251). Data were filtered at 1 kHz and recorded at a 5 kHz sampling rate. In all experiments, a silver wire chloridized in bleach was used as a pseudo-reference/counter electrode.

4.3 Results and Discussion

4.3.1 Description of nanobubble steady state

Figure 4.1(a) shows a series of cyclic voltammograms recorded at a 125 nm radius Pt electrode immersed in an aqueous solution containing 0.5 M H_2SO_4 and 50 mM KCl. The electrochemical cell is contained inside a custom pressure chamber in which the pressure, P_{ext}, is controlled by connecting the chamber to a high-pressure N_2 gas tank. For each *i-V* curve, the electrode potential is scanned negatively at 0.5 V/s starting from 0.0 V vs Ag/AgCl. The approximately exponentially increasing current beginning at ~-0.2 V vs Ag/AgCl reflects the reduction of H^+ resulting in the formation of dissolved H_2. Upon reaching a peak current, i_{nb}^{p}, of ~25 nA, H_2 generation decreases abruptly to a low residual level, i_{nb}^{r}. This waveshape is characteristic of a phase transition and corresponds to the formation of a single nanobubble[15-20] that hinders transport of protons to the electrode surface, as illustrated in Figure 4.1(b). For a single experiment, i_{nb}^{r} is nearly independent

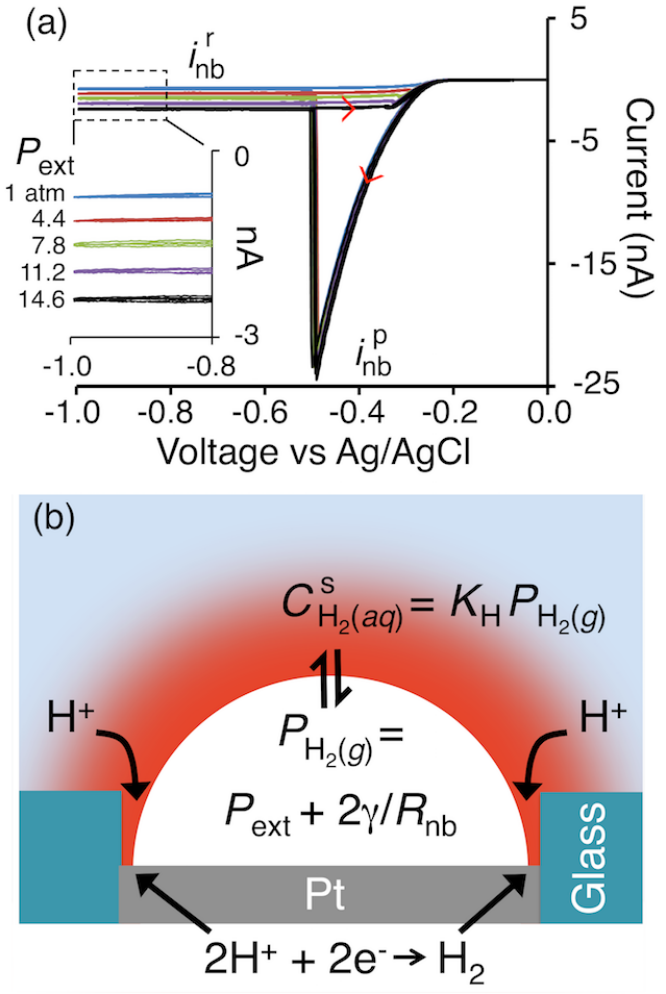

Figure 4.1. (a) A series of *i-V* responses corresponding to H_2 nanobubble formation at a 125 nm radius Pt electrode immersed in 0.5 M H_2SO_4 and 50 mM KCl as a function of P_{ext}. Scan rate 0.5 V/s. (b) Illustration of the steady-state dynamics of an electrochemically-generated nanobubble mathematically described by eqs 4.2 – 4.5. The steady state arises from H_2 dissolution through the bubble/solution interface, which occurs over the majority of the bubble surface, and is balanced by influx of H_2 electrogenerated via reduction of H^+ at the circumference of Pt exposed to solution at the base of the bubble.

of the applied potential and its low value indicates the electrode is nearly entirely covered by the bubble.[15]

The Laplace pressure resulting from the nanobubble's curvature increases the surface concentration driving the outward diffusive flux of H_2[21]; the bubbles formed here are unstable without continued electrogeneration of H_2 to replenish the outwardly diffusing H_2. Influx of gas occurs along the circumference of the gas/solution/electrode interface. It is driven by high local concentrations of dissolved H_2 induced by H^+ reduction at the Pt surface exposed to solution. Growth or shrinkage of the bubble changes the width of the exposed Pt decreasing or increasing, respectively, the rate of gas generation. This negative feedback mechanism is the origin of the bubble's steady state where the electrochemical current i_{nb}^{r} reflects the rate of H_2 electrogeneration, and thus is a direct measure of the bubble dissolution rate.

4.3.2 Current-pressure response

The voltammograms in Figure 4.1(a) were recorded at a series of applied pressures, P_{ext}, between 1 and 14.6 atm. The peak current at which nucleation occurs is not appreciably affected by additional external pressure; however, i_{nb}^{r} increases with increasing P_{ext}.

The dependence of i_{nb}^{r} on P_{ext} can be understood through the illustration in Figure 4.1(b). An increase in P_{ext} raises the bubble's internal pressure, $P_{H_2(g)}$, which is the sum of the external pressure and Laplace pressure. The higher $P_{H_2(g)}$ results in a higher surface concentration of H_2, $C_{H_2(aq)}^{s}$, causing an increased rate of H_2 diffusion from the bubble

surface. The increased rate of dissolution with P_{ext} necessitates an increase in H_2 electrogeneration to maintain the steady state; thus, i_{nb}^{r} increases with P_{ext}.

Note that the illustration in Figure 4.1(b) shows the surface of the Pt electrode below the plane of the surrounding glass surface. This geometry is common among nanoelectrode fabrication methods and is important to the interpretation of our results. Fabrication methods of Pt nanodisk electrodes are well known, as are the difficulties in characterizing their geometry.[22] Here we follow a melt-pull-mill procedure to fabricate the Pt nanoelectrodes (see Appendix).[23]

4.3.3 Mathematical model for dissolution flux

The current, i_{nb}^{r}, required to maintain the steady-state bubble can be expressed in terms of the dissolution flux of H_2. For a sphere cap bubble covering an electrode of radius a, i_{nb}^{r} is given by eq 4.2,[24] where $G(\theta,d)$ is a geometric factor that encompasses the bubble's contact angle, θ, and other factors, e.g., recession depth, d, that dictate the rate of H_2 diffusion from the bubble. The surface concentration of H_2, $C_{H_2(aq)}^{s}$, has an equilibrium value according to Henry's Law (eq 4.3), where the H_2 pressure inside the bubble is the ambient pressure plus the Laplace pressure (eq 4.4).

$$i = G(\theta,d)nFD_{H_2}aC_{H_2(aq)}^{s} \tag{4.2}$$

$$C_{H_2(aq)}^{s} = K_H P_{H_2(g)} \tag{4.3}$$

$$P_{H_2(g)} = P_{ext} + \frac{2\gamma}{R_{nb}} \tag{4.4}$$

Combining eqs 4.2 through 4.4, we arrive at:

$$i_{nb}^{r} = G(\theta,d)nFD_{H_2}aK_H\left(P_{ext} + \frac{2\gamma}{R_{nb}}\right) \quad (4.5)$$

where n is the number of electrons transferred per molecule (= 2 for H_2), F is Faraday's constant (96485 C/mol), D_{H_2} is the diffusion coefficient of H_2 (4.5 x 10^{-5} cm^2/s),[25] K_H is Henry's Law constant (0.78 mM/atm for H_2 at 25 °C),[26] and R_{nb} is the radius of interfacial curvature of the bubble sphere cap. Equation 4.5 indicates that i_{nb}^{r} changes linearly with P_{ext}, as experimentally observed. More importantly, eq 4.5 indicates that a plot of i_{nb}^{r} vs P_{ext} has an extrapolated x-intercept that occurs when P_{ext} is equal and opposite of the nanobubble Laplace pressure, i.e., when $P_{ext} = -2\gamma/R_{nb}$. This measurement is entirely analogous to the analytical technique of "standard additions" where, in this case, subsequent additions of pressure allows $2\gamma/R_{nb}$ to be determined from the $i_{nb}^{r} = 0$ intercept *without knowledge of any constants* in the multiplying prefactor ($G(\theta,d)nFD_{H2}aK_H$) in eq 4.5.

Figure 4.2(a) shows the *i-V* responses of 50 nm and 88 nm radius Pt electrodes in 0.5 M H_2SO_4 and 50 mM KCl as a function of P_{ext} both in the absence and presence of 1 mM Triton X-100, a non-ionic surfactant. SEM images of the electrodes are shown; in these images the bright spot at the center is the Pt disk cross section of a Pt nanowire embedded in quartz. The values of i_{nb}^{r} recorded at -1 V are plotted against P_{ext} and fit by linear least squares regression in Figure 4.2(b). In all cases, the data fit a regression line with an R^2 better than 0.999 indicating the linear model of eq. 4.5 well fits the data. The linearity also suggests that the bubble geometry is not changing appreciably under application of external pressure.

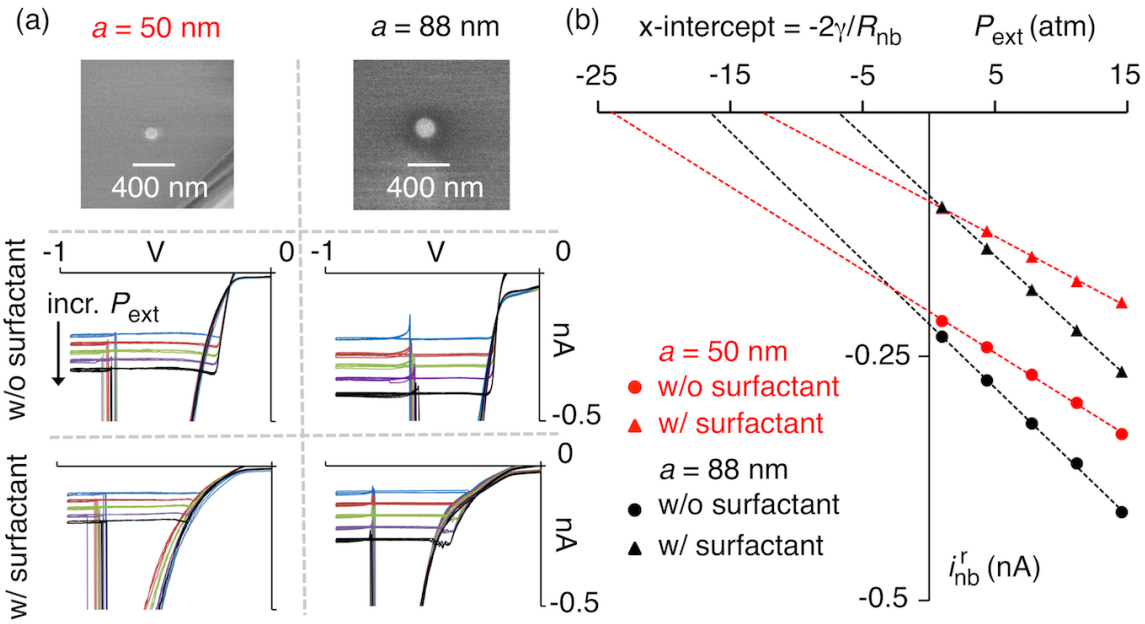

Figure 4.2. (a) SEM images of Pt disk nanoelectrodes measuring 50 nm radius and 88 nm radius immediately after fabrication taken prior to their recession. Their *i*-*V* responses in 0.5 M H_2SO_4 and 50 mM KCl at increasing applied pressures are shown in the absence of a surfactant and with 1 mM Triton X-100 added to solution. The residual current at -1 V is plotted vs applied pressure and fit via linear least squares regression in (b). The absolute value of the x-intercept of the regression line gives the Laplace pressure resulting from the bubble radius of curvature, R_{nb}, and surface tension, γ.

4.3.4 Calculation of Laplace pressure

From eq 4.5, the x-intercept of the regression line gives the negative of the Laplace pressure where P_{ext} cancels the pressure resulting from interfacial curvature, and the H_2 flux is theoretically zero. The Laplace pressures within bubbles formed on the 88 nm radius electrode (black), with and without surfactant, are 6.9 ± 0.2 and 16.4 ± 0.4 atm (95% confidence interval), respectively. The measured Laplace pressure in the presence of surfactant is 42 ± 2% of that without surfactant, in agreement with the ratio of the known surface tensions (45% for γ = 33 mN/m and 73 mN/m in aqueous Triton X-100 and sulfuric acid solutions, respectively).[27,28] Assuming these macroscopic values for the surface tension, we calculate radii of curvature from the Laplace pressures as 92 ± 6 and 87 ± 4 nm for γ = 33 mN/m and 73 mN/m, respectively. Similarly, the Laplace pressures of bubbles generated at the 50 nm radius electrode were measured as 12.7 ± 0.3 and 24.9 ± 0.5 atm (95% confidence interval) equating to radii of 51 ± 2 and 58 ± 3 nm for γ = 33 mN/m and 73 mN/m, respectively. These radii of interfacial curvature are remarkably close to the radii of the electrodes as measured by SEM. The match between the electrode radius and bubble radius of curvature signifies the bubbles are very nearly hemispherical. Either a higher or a lower contact angle would increase the bubble's radius of curvature and would require an unrealistically high surface tension to equal the experimentally measured Laplace pressure.

While the Laplace pressure measurement by extrapolation does not require any prior knowledge of the bubble contact angle or electrode radius or geometry, the current magnitude and slope of i_{nb}^{r} -P_{ext} are a reflection of these factors. The geometric factor, $G(\theta,d)$, should be the same for bubbles on a given electrode if the only parameter that

changes is the surface tension. Isolating this factor from the constants in the slope term yields $G(\theta,d)$ = -0.21 ± 0.01 and -0.22 ± 0.01 for the 88 nm radius electrode and $G(\theta,d)$ = -0.21 ± 0.01 and -0.24 ± 0.01 for the 50 nm radius electrode, with and without surfactant, respectively. The nearly 1:1 ratio of the $G(\theta,d)$ factor and the decrease in current magnitude in the presence of surfactant to ~45% (corresponding to the ratio of surface tensions) of that without surfactant further supports the hypothesis that bubble geometry remains constant between experiments.

Figure 4.3(a) shows the experimentally measured Laplace pressures plotted versus the reciprocal electrode radius. The surface tension calculated from the Laplace pressure, using eq. 4.4, is shown in Figure 4.3(b). Bubbles were formed on electrodes ranging in size from 7 to 200 nm radius both in the presence (blue triangles) and absence of surfactant (red squares). The dashed lines indicate macroscopic values of γ from the literature (noted above). It is apparent from the agreement between experiment and theoretical values in the absence of surfactant (data in red) that the bubbles are very nearly hemispherical and that the surface tension is not changing appreciably from the macroscopic value over the size range studied. With surfactant present (data in blue), Laplace pressures match the expected values for radii larger than ~40 nm. The Laplace pressures within bubbles formed on electrodes smaller than ~40 nm with surfactant present are approximately half the expected value for a hemispherical bubble. In this case, the geometric factors for two of the four data points in question are lower in the presence of surfactant – an indication that these bubbles may have a larger radius of curvature. Therefore, we cannot make strong conclusions about the surface tension of surfactant-coated bubbles below 40 nm radius. There could be several reasons for the more complex behavior, e.g., an energy cost of bending a surfactant

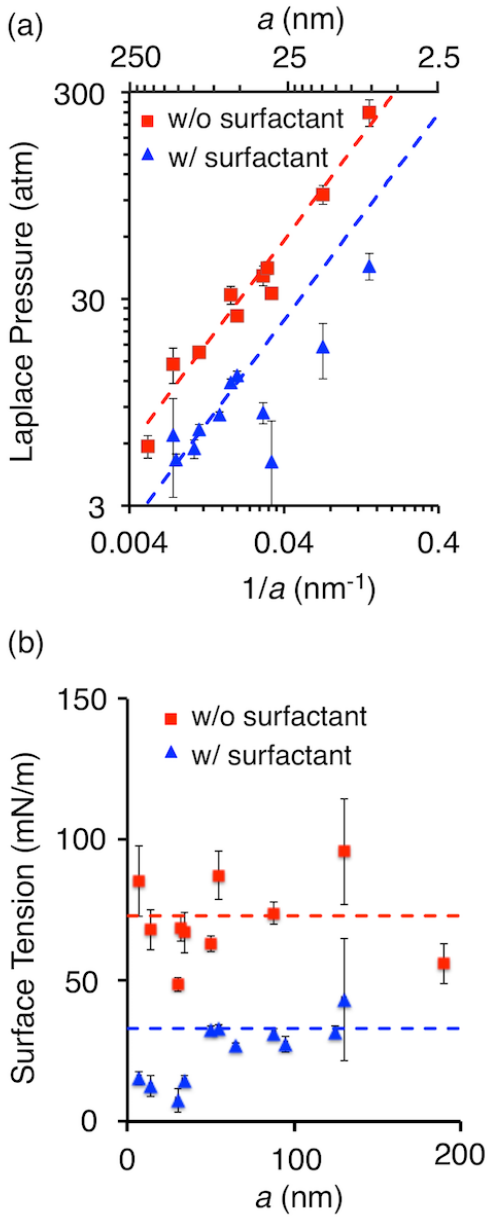

Figure 4.3. (a) Measured Laplace pressures as described in Figure 4.2 resulting from bubble interfacial curvature in the absence of surfactant (red squares) and in the presence of 1 mM Triton X-100 (blue triangles) versus reciprocal electrode radius. Dashed lines are $2\gamma/a$ assuming macroscopic values for the surface tension with (blue) and without (red) surfactant. Data plotted on log scales. (b) Surface tension values calculated from the Laplace pressures in (a) assuming bubbles are hemispherical (radius of curvature equals the electrode radius). Dashed lines are the macroscopic surface tensions with (blue) and without (red) surfactant. Error bars represent a 95% confidence interval.

layer with a preferred curvature, or perhaps the increasingly shorter three-phase contact line for the smallest of bubbles cannot support high enough rates of gas generation in the presence of surfactant. Nevertheless, the interface in the absence of surfactant does not suffer these drawbacks for the smallest bubbles studied.

4.4 Conclusions

The electrochemical pressure-addition measurements presented here demonstrate the immense forces at nanoscale interfaces and validate the classical thermodynamic description of liquid interfaces as small as ~10 nm. Our results may contribute to the development of new technologies that exploit the thermodynamics of highly curved gaseous interfaces, including plasmonic nanobubble therapies,[29] underwater adhesives based on Gecko feet,[30] and nanobubble desalination technology.[31]

4.5 Appendix

4.5.1 Finite element simulations

Simulations of H_2 diffusion were performed to calculate the expected current response as a function of bubble/electrode geometry and pressure. Mass transport was described by the steady-state diffusion equation (eq 4.6) within the axially symmetric domain shown in Figure 4.4A.

$$0 = D_{H_2} \nabla^2 C_{H_2} \tag{4.6}$$

where D_{H_2} (4.5×10^{-5} cm^2/s)[25] is the diffusion coefficient of dissolved H_2 and C_{H_2} its concentration.

The concentration at the bulk boundary far from the bubble was set to zero and the

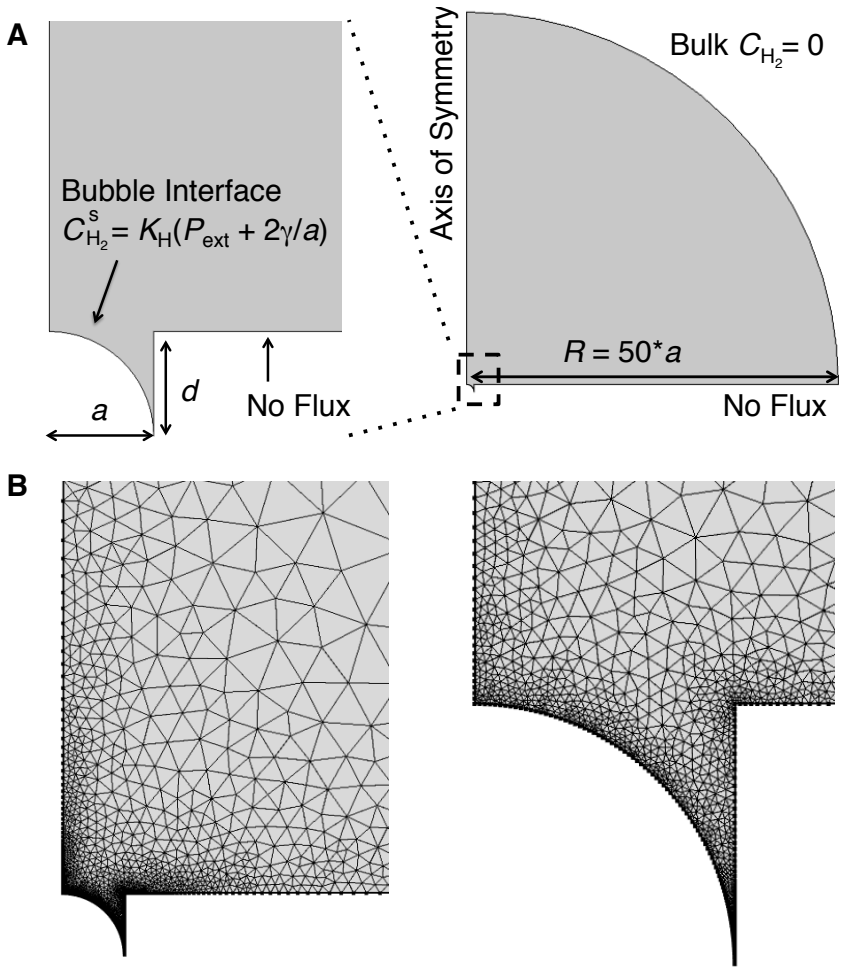

Figure 4.4. Finite element simulation of nanobubbles. (A) Geometry, boundary conditions and (B) mesh for finite element simulation of a hemispherical bubble of radius, *a*, recessed below the glass support by depth, *d*, described in detail above.

absence of H_2 flux into the quartz surface was described by

$$0 = D_{H_2} \nabla C_{H_2} \cdot \vec{n} \tag{4.7}$$

where $\vec{n}$ is the inward pointing unit normal to the surface.

In these simulations, we assumed the rate of gas transfer across the bubble interface to be infinitely fast and the concentration of dissolved H_2 at the bubble-solution interface was held at the equilibrium value for the bubble's internal pressure (determined by its radius of curvature, R_{nb}, and surface tension, γ, through the Young-Laplace equation) according to Henry's Law via eq. 4.8.

$$C^{\mathrm{s}}_{\mathrm{H}_2(aq)} = K_{\mathrm{H}} \left(P_{\mathrm{ext}} + \frac{2\gamma}{R_{\mathrm{nb}}} \right) \tag{4.8}$$

The net transport of H_2 from the bubble was calculated by integration of the flux over the bubble-solution interface and converted to a current by noting that 2 electrons are used to form every molecule of H_2.

$$i = -2FD_{\mathrm{H}_2} \int_{\mathrm{bubble}} \nabla C_{\mathrm{H}_2} \cdot \vec{n} \tag{4.9}$$

The equations were solved using the commercial finite element package COMSOL Multiphysics 5.2. Discretization of the equations was performed using a mesh as shown in Fig 4.4B, which was made fine enough such that any further size reduction produced no change in the simulation results.

4.5.2 Deviation from Henry's law

Making use of linear regression to calculate the Laplace pressure makes the assumption that Henry's Law obtains, i.e., H_2 solubility is linear over the range of pressures studied. While H_2 solubility at increasing pressures is not perfectly linear, this deviation is

minor in the ranges of pressures we studied, as can be seen in Figure 4.5A, which plots experimental measurements of H_2 solubility vs pressure from Wiebe *et al*.[26] alongside those predicted by Henry's law. Importantly, the impact of any deviations on the measured Laplace pressures is also negligible. This can be seen in Figure 4.5B which shows results for finite element simulation of the currents associated with the diffusion-limited flux of H_2 from a 7 nm radius bubble at zero recession depth under increasing applied pressures assuming Henry's Law (black) or using the experimentally measured values of Wiebe *et al.* (red). The choice of a 7 nm radius bubble represents the worst-case scenario in our experiments. Yet, even in this case, the Laplace pressures derived from intercepts of linear least squares differ by less than 3% (211 atm vs 206 atm for experimental and Henry's law, respectively). Thus we can conclude that the assumption that Henry's law obtains is reasonable and does not lead to significant errors.

4.5.3 Imaging electrode recession

SEM images of electrodes immediately after FIB milling suggest the Pt nanodisk is coplanar with the quartz surface. However, the electrodes become recessed during their use, even while taking precautions as suggested by Nioradze *et al.* to minimize electrostatic discharge.[23] Figure 4.6 shows the same electrode (left) immediately after fabrication and (center) after recession occurs. Remilling ~500 nm of quartz off the end of the damaged electrode exposes the Pt wire once again, as is shown in the right-hand panel of the figure. The mechanism of this damage is not fully understood. The depth of the recession is characterized as described above. Figure 4.7 shows reasonable agreement between experimental and simulated values of the residual current from H_2 bubbles at various

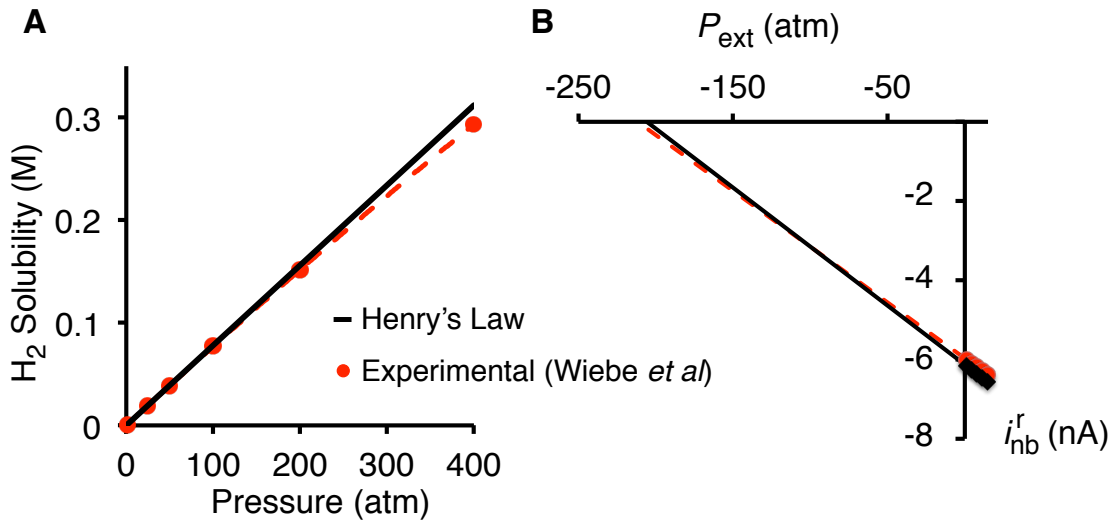

Figure 4.5. Validity of Henry's Law at high pressure. (A) Comparison of (red) experimental values of H_2 solubility vs pressure reported by Wiebe *et al*. with (black) those predicted by Henry's Law (B) Simulated currents from a 7 nm radius bubble at zero recession depth vs P_{ext} using each solubility-pressure relation to define the surface concentration. Intercepts from the linear regression give Laplace pressures of 211 atm (Wiebe *et al.*) and 206 atm (Henry's law) representing a difference of less than 3%.

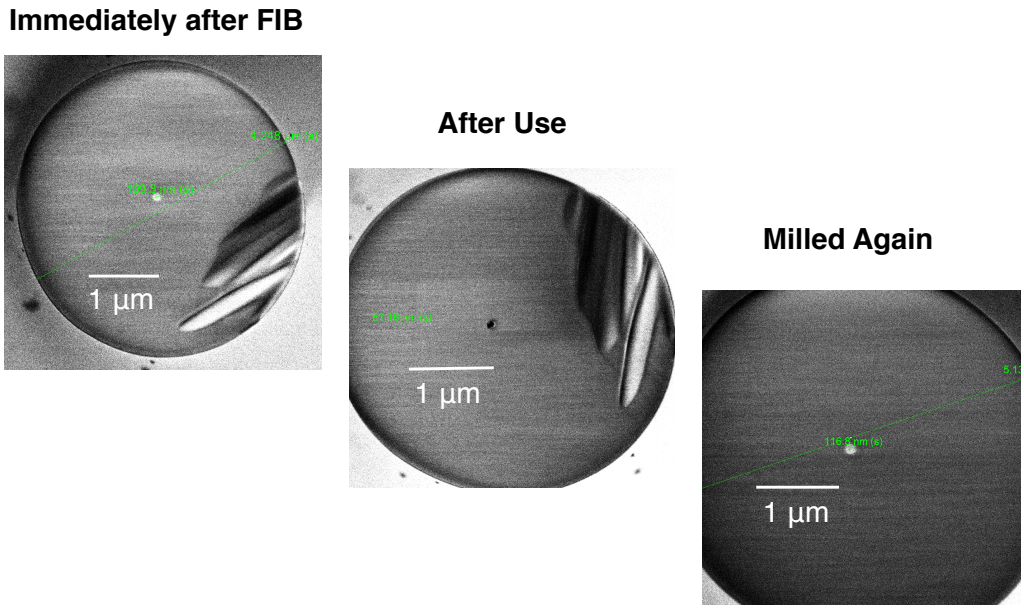

Figure 4.6. Recession of nanoelectrodes. SEM images of a single 55 nm radius Pt nanodisk electrode: (left) immediately after FIB milling, (center) after use in an electrochemical circuit outside of the SEM, and (right) after further FIB milling of ~500 nm off the end of the quartz shank. It is apparent that the electrode became recessed while outside of the SEM and was re-exposed after further milling, providing further evidence that the recession depth is only a few electrode radii.

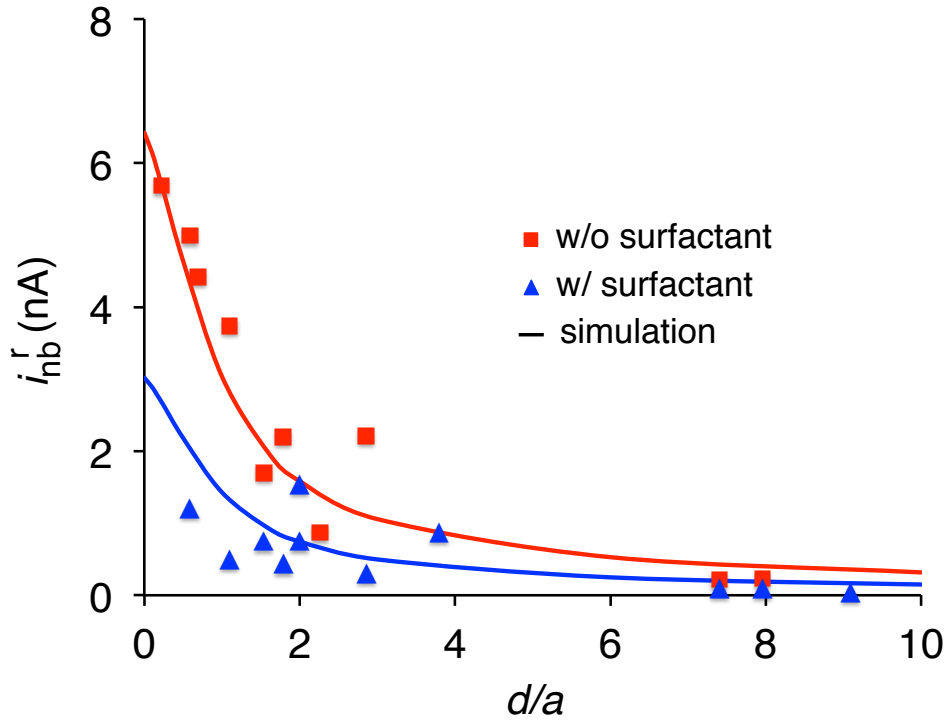

Figure 4.7. Comparison of simulation and experiment. **(**Points) Experimentally measured residual currents after bubble formation without surfactant (red) and with surfactant (blue) versus the ratio of the depth of recession, *d*, to the electrode radius, *a*. Lines are the result of finite element simulations calculating the integrated H_2 flux from a 50 nm radius hemispherical bubble at varying recession depths.

recession depths.

4.5.4 Geometric factor

Determination of the Laplace pressure from the i_{nb}^{r} -P_{ext} response does not require any knowledge of the multiplying prefactor ($G(\theta,d)nFD_{H2}aK_H$) in eq. 4.5. As such, no errors are introduced in the reported values of $2\gamma/R_{nb}$ from uncertainties in the bubble and electrode geometries, diffusion coefficients, and H_2 solubility. Likewise, the only uncertainty in gamma is introduced by the error in the bubble radius. The following paragraphs discuss our assertion that $R_{nb} = a$ in our experiments.

To estimate R_{nb}, first, we observe that the low residual current observed upon formation of a bubble indicates that it covers the majority of the underlying electrode. We also observe that for a given circular contact area a maximum in Laplace pressure occurs when the contact angle is 90°, i.e., when the bubble is hemispherical. Combined, these two observations imply that the minimal R_{nb}, corresponding to the maximal Laplace pressure, is equal to the radius of the electrode, a.

For the larger electrodes (bubbles) the surface tension is expected to obtain its macroscopic value. For these bubbles, the measured Laplace pressure is in good agreement with this maximal Laplace pressure (dashed lines, Figure 4.3(a)), i.e., these bubbles are (very nearly) hemispherical and $R_{nb} \approx a$. For the smaller electrodes, in the absence of surfactant, this agreement is maintained, suggesting no significant change in either the surface tension or the contact angle for the range of bubble sizes investigated.

For the smallest electrodes in the presence of surfactant, the measured Laplace pressure differs significantly from that predicted assuming $R_{nb} = a$ and the surface tension

is equal to the macroscopic value, indicating these bubbles behave differently from those on the same electrodes in the absence of surfactant. Inspection of eq 4.4 shows that in principle, the different effects of changing γ and R_{nb} should be identifiable from i_{nb}^{r} -P_{ext} responses measured with and without surfactant. If the addition of surfactant solely reduced the surface tension while leaving the geometry unchanged, then the i_{nb}^{r} -P_{ext} slope with surfactant should be identical to that without surfactant and the ratio of the current values at the y-intercept equal to the ratio of the surface tensions. Comparison of simulations for 50 nm radius nanobubbles on a 50 nm radius electrode recessed by 100 nm at various surface tensions (Figure 4.8) shows this to be the case. The red, blue, and green three parallel lines correspond to without surfactant (73 mN/m), with surfactant causing the surface tension lower to the macroscopic level (33 mN/m), and with surfactant but a surface tension below its macroscopic level (13 mN/m). The dashed line is the result of simulations with the bubble's radius of curvature increased to 70 nm (base radius of 50 nm, height of 20 nm) with the surface tension at its macroscopic value in the presence of surfactant (33 mN/m). As predicted, the different geometry gives rise to a different gradient, yet the slight differences in the i_{nb}^{r} -P_{ext} response shown by the green and dashed lines (R_{nb} = 50 nm & γ =33 mN/m and R_{nb} = 70 nm γ =13 mN/m, respectively) highlight the difficulty of making strong claims from experimental i_{nb}^{r} -P_{ext} measurements without independent confirmation of bubble geometry.

With the different effects of γ and R_{nb} in mind, we can examine the experimental i_{nb}^{r} -P_{ext} responses from bubbles formed with and without surfactant present on the same electrode shown in Figure 4.9A. Figure 4.9B plots the ratio of the gradients with and

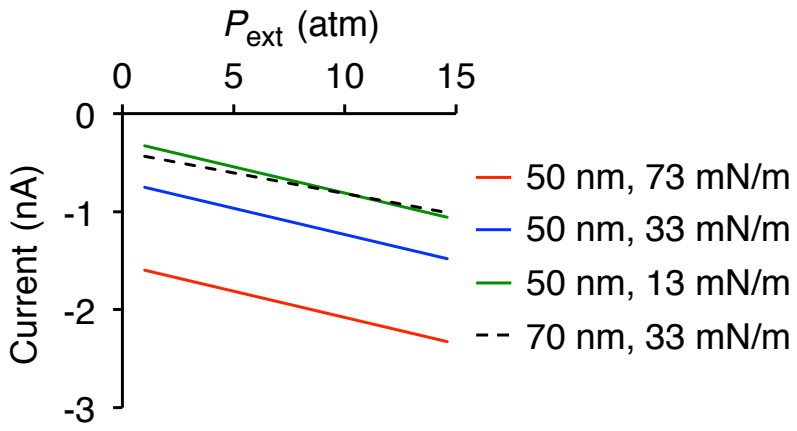

Figure 4.8. Simulated current-pressure response. Finite element simulations of the current equivalent to the diffusion limited flux of H_2 away from a steady-state bubble as a function of applied pressure. The simulations were performed with an electrode recession depth of 100 nm and an electrode radius of 50 nm. The bubble radius of curvature and the surface tension for each simulation is indicated in the legend.

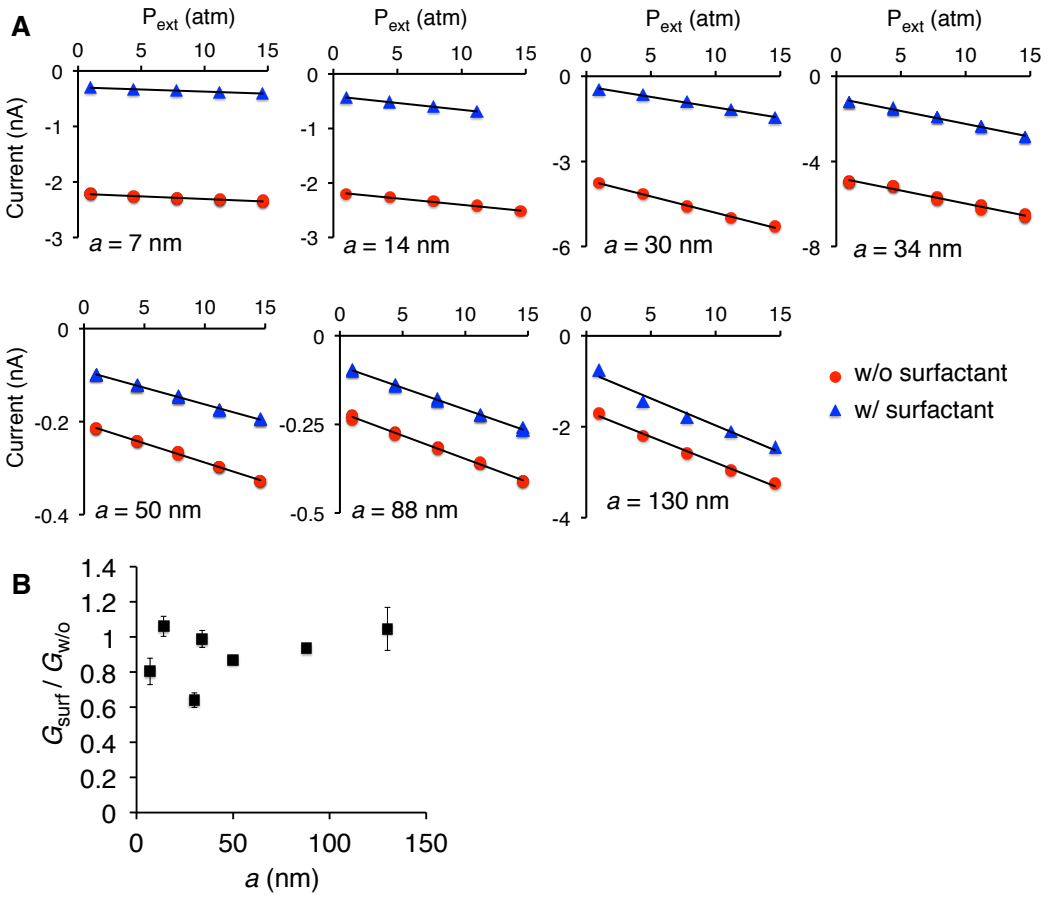

Figure 4.9. Examining the current-pressure response. (A) experimental i_{nb}^{r} -P_{ext} responses for steady-state H_2 bubbles on Pt electrodes of different radii, a (indicated on individual plots) in a solution of 0.5 M H_2SO_4 and 50 mM KCl with (blue) and without surfactant (red). (B) The ratio of the $G(\theta,d)$ factors calculated from the slope of the i_{nb}^{r} - P_{ext} responses with and without surfactant in (A).

without surfactant for each electrode in Figure 4.9A, which due to cancellation of factors is equivalent to the ratio of $G(\theta,d)$ with and without surfactant. Several of the $G(\theta,d)$ ratios are ~1, indicating no difference in the geometry between the two cases. However, at the small sizes, the ratio is inconsistent, indicating variation of the bubble geometry between the two cases. For these cases, we are unable to deconvolute the two effects accurately and errors are introduced if we convert Laplace pressures to surface tensions using the assumption that $R_{nb} = a$.

Contact angles of bubbles on surfaces exhibit anomalous behavior in a number of ways. Unlike oil droplets,[32] the contact angle of nanobubbles tend to be significantly smaller (as measured through the air) than macrobubbles.[33] AFM images also indicate that nanobubbles have a constant interfacial curvature suggesting distance-dependent surface forces do not induce any pressure gradient at varying separations along the sphere cap.[34] Different research groups report contrasting results that nanobubble contact angles do[35] and do not[36] vary as a function of size as expected for either an effect of surface forces or line tension. We suspect that the nanobubbles in our study sustained by gas evolution are far from their equilibrium contact angle and instead take on a 90° contact angle because they are limited from further growth by influences of the geometry and wettability of the quartz walls in the electrode recession well. Furthermore, the linearity of the i_{nb}^{r}-P_{ext} response also suggests that the bubble geometry is not changing appreciably under application of external pressure, which can be understood by considering that H_2 generation is likely not kinetically limited at the i_{nb}^{r}. Rather, i_{nb}^{r} is a steep function of the bubble's contact angle and the width of Pt exposed at the 3-phase contact line where the replenishing rate can easily match the increased dissolution rate with miniscule change in geometry.

4.6 References

1. Blander, M.; Katz, J. L. *AIChE J.* **1975**, *21*, 833–848.

2. Lifshitz, I. M.; Slyozov, V. V. *J. Phys. Chem. Solids* **1961**, *19*, 35-50.

3. Butt, H.-J.; Kappl, M. *Adv. Colloid Interface Sci*. **2009**, *146*, 48–60.

4. Evans, R.; Marconi, U. M. B.; Tarazona, P. *J. Chem. Soc., Faraday Trans 2* **1986**, *82*, 1763-1787.

5. Guggenheim, E. A. *Trans. Faraday Soc.* **1940**, *35*, 397-412.

6. Tolman, R. C. *J. Chem. Phys*. **1949**, *17*, 333-337.

7. Fujikawa, S.; Yano, T.; Watanabe, M. *Vapor Liquid Interfaces, Bubbles and Droplets. Fundamentals and Applications*; Springer-Verlag: Berlin, 2011.

8. Kalikmanov, V. I. *J. Chem. Phys*. **2008**, *129*, 044510.

9. Moody, M.; Attard, P. *Phys. Rev. Lett*. **2003**, *91*, 056104.

10. Factorovich, M. H.; Molinero, V.; Scherlis, D. A. *J. Am. Chem. Soc*. **2014**, *136*, 4508–4514.

11. Fisher, L. R.; Israelachvili, J. N. *Nature* **1979**, *277*, 548-549.

12. Kohonen, M. M.; Christenson, H. K. *Langmuir* **2000**, *16*, 7285–7288.

13. Zhang, B.; Zhang, Y.; White, H. S. *Anal. Chem*. **2006**, *78*, 477–483

14. Cussler, E. L. *Diffusion: Mass Transfer in Fluid Systems,* 2nd ed.; Cambridge University Press: New York, 1997.

15. Luo, L.; White, H. S. *Langmuir* **2013**, *29*, 11169–11175.

16. Chen, Q.; Luo, L.; Faraji, H.; Feldberg, S. W.; White, H. S. *J. Phys. Chem. Lett*. **2014**, *5*, 3539–3544.

17. Chen, Q.; Wiedenroth, H. S.; German, S. R.; White, H. S. *J. Am. Chem. Soc*. **2015**, *137*, 12064–12069.

18. Chen, Q.; Luo, L.; White, H. S. *Langmuir* **2015**, *31*, 4573–4581.

19. German, S. R.; Chen, Q.; Edwards, M. A.; White, H. S. *J. Electrochem. Soc*. **2016**, *163*, H3160–H3166.

20. German, S. R.; Edwards, M. A.; Chen, Q.; Luo, L.; White, H. S. *Faraday Discuss.* **2016**, doi:10.1039/C6FD00099A.

21. Ljunggren, S.; Eriksson, J. C. *Colloid Surf., A* **1997**, *129-130*, 151–155.

22. Oja, S. M.; Fan, Y.; Armstrong, C. M.; Defnet, P.; Zhang, B. *Anal. Chem*. **2016**, *88*, 414–430.

23. Nioradze, N.; Chen, R.; Kim, J.; Shen, M.; Santosh, P.; Amemiya, S. *Anal. Chem*.**2013**, *85*, 6198–6202.

24. Alfred, L.; Oldham, K. B. *J. Phys. Chem*. **1996**, *100*, 2170-2177.

25. Mazarei, A. F.; Sandall, O. C. *AIChE J*. **1980**, *26*, 154−157.

26. Wiebe, R.; Gaddy, V. L.; Heins, Jr., C. *Ind. Eng. Chem.* **1932**, *24*, 823-825.

27. Makievski, A. V.; Fainerman, V. B.; Joos, P. *J. Colloid Interface Sci.* **1994**, *166*, 6-13.

28. Suggitt, R. M.; Aziz, P. M.; Wetmore, F. E. W. *J. Am. Chem. Soc.* **1949**, *71*, 676-678.

29. Lukianova-Hleb, E. Y.; Kim, Y.-S.; Belatsarkouski, I.; Gillenwater, A. M.; O'Neill, B. E.; Lapotko, D. O. *Nature Nanotech.* **2016**, *11*, 525–532.

30. Stark, A. Y.; Badge, I.; Wucinich, N. A.; Sullivan, T. W.; Niewiarowski, P. H.; Dhinojwala, A. *Proc. Natl. Acad. Sci.* **2013**, *110*, 6340-6345.

31. Lee, J.; Laoui, T.; Karnik, R. *Nature Nanotech.* **2014**, *9*, 317-323.

32. Zhang, X.; Ducker, W. *Langmuir* **2008**, *24*,110-115.

33. Song, B.; Walczyk, W.; Schönherr, H. *Langmuir* **2011**, *27*, 8223–8232.

34. Borkent, B.; de Beer, S.; Mugele, F.; Lohse, D. *Langmuir* **2010**, *26*, 260-268.

35. Yang, J.; Duan, J.; Fornasiero, D.; Ralston, J. *J. Phys. Chem. B*, **2003**, *107*, 6139-6147.

36. An, H.; Liu, G.; Craig, V. S. J. *Adv. Colloid Interface Sci*. **2015**, *222*, 9–17.

CHAPTER 5

CONCLUSIONS AND FUTURE DIRECTIONS

5.1 Summary

5.1.1 Context

Atomic force microscope images have shown that incomplete wetting of surfaces results in long-lived interfacial nanobubbles despite well-known theoretical considerations suggesting they should dissolve in less than a millisecond. While AFM offers remarkable resolution for imaging, it has limited utility in elucidating the underlying mechanisms of dynamic systems. Questions about the observed stability of interfacial nanobubbles have puzzled researchers for two decades. Vincent Craig, a leader in the field, voiced his consternation saying, "We are left with two possible conclusions. Either nanobubbles are closed systems that don't communicate with their surroundings, or there exists a dynamic equilibrium whereby the gas that dissolves out of them is recycled back into the bubbles to keep them stable. Neither of which is tolerable."[1] The community of researchers working on nanobubbles has been actively seeking new techniques to unveil the dynamic nature of nanobubbles.

Application of nanoelectrochemical methods to the study of nanobubbles as pioneered in the White laboratory has allowed such dynamic studies for the first time.

Nanoelectrochemistry provides means for direct measurement and control of fluxes of dissolved gas with high temporal and spatial resolution. Luo et al.[2] laid the groundwork for these voltammetric studies in 2013 showing the characteristic waveshape with a peak and residual current. It was proposed that these features correspond to the nucleation and steady state, respectively, of a single nanobubble. Investigating these processes is the focus of the work in this dissertation.

5.1.2 Initial scientific questions

The most notable behavior of nanobubbles as discussed in the literature is their surprising stability. Hence, measurement of the lifetimes of electrochemically generated nanobubbles was an important goal from the outset. The ability to perform repeated voltammetric cycles in which each new scan indicated formation of a bubble was an indication that the bubbles must dissolve between scans. Chapter 2 details the analytical method we developed to measure nanobubble lifetimes. Our approach was simply to reduce the time that gas generation was "turned off" between formation of a bubble and the attempt to reform another bubble. Indeed, at short time intervals, as set by the scan rate, the characteristic peak corresponding to nucleation of a new bubble was absent on the second voltage scan, indicating the bubble survived the time duration over which gas generation was stopped. Increasing the time interval with slower scan rates allowed the bubble to dissolve and the fastest scan rate at which the bubble dissolved was used to calculate the lifetime. The measured lifetimes (on the order of tens of milliseconds) are the shortest reported for nanobubbles in the literature, and yet are still 2 to 3 orders of magnitude longer than diffusion limited theories predict.[3] To account for the discrepancy, we proposed a

kinetic limitation on the rate of gas transfer across the gas/water interface.

Calculation of the rate limitation, however, is highly dependent upon accurate knowledge of the geometry of the bubble and electrode. Attempts to image electrodes and bubbles via AFM revealed that our nanoelectrodes were of a recessed geometry. Since electrode recession increases mass transport resistance, it was an indication that our method of electrode sizing based upon a diffusion limited current had underestimated the electrode and, therefore, bubble sizes as well. Furthermore, recession serves to slow the diffusive flux away from the bubble during lifetime measurements and thus doubly affects the calculated kinetic limitation.

In considering the ramifications of electrode recession on our work, we concluded that there are cases where the electrode geometry strongly affects results and cases where it does not. Experiments in which we report measurements of the surface concentration of generated species are unaffected by electrode geometry. Because we characterize electrodes via the diffusion limited current of ferrocene, i_{lim}, the apparent electrode radius, a, from this measurement acts as a geometric factor and accounts for deviation from ideal nanodisk geometry. In the calculation of surface concentration of dissolved gas, only the ratio of diffusion coefficients scaled by the current affects the outcome. All other variables cancel out.

$$C_{gas}^{surf} = \frac{i_{gas} 4nFD_{Fc} a C_{Fc}^{bulk}}{i_{lim} 4nFD_{gas} a} \quad (1)$$

The actual electrode size then is slightly larger than the calculated apparent size, but the subsequent calculation of surface concentration is correct despite incomplete knowledge of geometry. Calculations in which bubble and electrode geometries are assumed to assess bubble dynamics are affected by an unknown recession. Thus, while the method for

measurement of bubble lifetimes is sound, the calculated rate constant could be made more accurate with highly characterized electrodes.

In subsequent work, laser pulled and focused ion beam milled electrodes were employed. This method does not avoid recession, but it allows determination of the electrode radius independently via scanning electron microscopy. Measurement of a diffusion limited current for ferrocene then allows calculation of the depth of recession. This is detailed in section 4.2.2.

Sizing electrodes accurately in this fashion enabled the measurement of Laplace pressures reported in Chapter 4. Here, we demonstrated that the residual current after bubble formation could be modulated through application of external pressure which acts to increase the dissolved gas solubility at the bubble surface. In a means analogous to standard additions, extrapolation of the current-pressure response allows calculation of the unknown internal pressure. These extrapolated pressures agree very well with the expected values using the macroscopic surface tension and the electrode radius as imaged by SEM. Our measurements, therefore, confirm the classical thermodynamic description of gas/liquid interfaces for radii of curvature as small as ~10 nm.

There had been real doubt whether interfacial nanobubbles on hydrophobic surfaces were truly highly pressurized as classically expected. A proposed explanation for their longevity was that surface contaminants might coat nanobubbles and drive their surface tension to zero as they "jam" together upon bubble shrinkage.[4] With no surface tension, there would be no difference in chemical potential between the gas inside the bubble and the dissolved gas in solution and the bubble would be at equilibrium. Based upon our measurements of Laplace pressures, contamination does not appear to affect surface

tension in our experiments.

In these studies, electrode size and recession depth were measured independently. Thus, we were able to compare experimental values for the residual current with finite element simulations of the gas dissolution flux from bubbles on electrodes with comparable geometry. These results are shown in Figure 4.7. For these simulations, it was assumed that gas transfer at the bubble-solution interface occurs infinitely fast and that flux is solely limited by diffusion. As the i_{nb}^{r} we measure from bubbles at various recession depths match closely enough to the simulated values assuming infinitely fast gas transfer, our experiments suggests that any kinetic limitation that may be present should occur at a rate greater than $k_f = 10^{-6}$ mol N^{-1} s^{-1}. We list this value for k_f because placing this limitation on flux across the bubble interface reduces the simulated current by ~50% for bubbles recessed by $d/a < 4$ and such a rate limitation would be noticeable.

Chapter 3 presents measurements of the critical concentration, C^{crit}, at which bubble nucleation occurs quickly relative to the timescale of the voltammetric experiment. Bubble nucleation is a steep function of the concentration of dissolved gas which in turn increases exponentially as a function of voltage. The result is a threshold phenomenon such that the probability of bubble formation changes from essentially zero to 1 over a span of ~30 mV. The electrode surface concentration of dissolved H_2 at the instant prior to bubble formation is the reported C^{crit}. The critical nucleus that spontaneously forms at this concentration is in metastable equilibrium with the dissolved gas according to classical nucleation theory, and therefore, has an internal pressure, P_{bubble}, equal to the partial pressure of dissolved H_2 given by Henry's Law, $C_{crit} = P_{bubble}K_H$. This pressure is directly related to the radius of curvature, r_{crit}, of the critical nucleus by the Laplace-Young equation, $P_{bubble} - P_{ambient} =$

$2\gamma/r_{crit}$, using the macroscopic value of the solution surface tension, γ. Whether nucleation in these experiments occurs homogeneously or heterogeneously does not change this radius.

The exact rate of a kinetic limitation has no bearing on the measurement of the critical radius of bubble-forming nuclei. Any interfacial gas transfer kinetics must necessarily agree with Henry's law and thus should satisfy $k_f/k_b = K_H$. At equilibrium, the rate of gas exiting and entering the bubble is equal, which can be written as a rearrangement of Henry's Law by $J = 0 = P_{bubble}*k_f - C*k_b$. Thus, as it should be, the thermodynamic and kinetic descriptions agree on the equilibrium configuration. Our measurement of a kinetic limitation for a dissolving bubble does not change the value of Henry's Law. Defining a rate of k_f simply means there is a corresponding k_b that satisfies Henry's Law at equilibrium. A consequence of the kinetic limitation is that the rate of growth and dissolution would not be diffusion limited, but the radius at which there is a transition between the two regimes is unchanged.

In the experiments reported in this dissertation, electrochemically generated nanobubbles exhibit markedly different behaviors compared with the interfacial nanobubbles on hydrophobic surfaces reported in the literature. The nanobubbles studied in this dissertation behave quite classically in regards to their dissolution and internal pressures. These results suggest that the mechanism granting interfacial nanobubbles peculiar properties likely has its origin in the bubble's interface with the hydrophobic surface. This is in line with recent reports on interfacial bubbles suggesting that pinning of the three phase contact line allows stability.

5.1.3 Limitations of this work

The strength of the conclusions in this dissertation could in general be improved by direct imaging of electrodes and bubbles to confirm the pictorial representations presented. Also, we do not explicitly control or measure the surface roughness or exposed crystal facet of the electrodes. These are expected, in part, to determine the surface energy of bubble nuclei and affect nucleation. At this time, we do not know if bubble formation occurs at a specific nucleation site on each electrode or if there are many sites. Additionally, experimental measurement of surface tensions and gas solubility at the pressure and in the solutions employed could improve precision of calculations.

5.2 Future Directions

5.2.1 Imaging techniques

Imaging a nanobubble by AFM is a delicate task, but there is a rich literature describing that it is possible. Great care must be taken in choosing an AFM probe and tuning its oscillation in liquid to ensure the forces exerted by the cantilever are minimized. Also the sharpened tip must be rigorously cleaned by plasma treatment such that the bubble does not wet the probe and lift off the surface. If the issues surrounding electrode recession can be overcome, then combining AFM imaging with electrochemical measurements should be possible.

Dynamic transmission electron microscopy is an emerging tool able to directly visualize nanoscale phenomena in liquids with remarkable resolution. It has recently been employed to image nanobubbles nucleated in solution by electron beam irradiation.[5] With a compatible electrochemical cell and low beam energies, high spatially and temporally

resolved images could be captured.

5.2.2 Nucleation rates

Quantitative investigations of the nucleation kinetics of nanobubbles should be made to determine factors that lead to the phase-transition electrode overpotential. Experiments in this dissertation have shown that at moderate scan rates (<2 V/s), the critical current preceding nucleation of a H_2 bubble corresponds to a gas supersaturation ratio of ~300, independent of electrode size. However, at increasingly fast scan, rates both higher overpotentials and larger peak currents are required for bubble formation. This behavior hints at a kinetic limitation for the nucleation step, consistent with theoretical expectations.

Experimental study of this nucleation rate is intrinsically difficult. The nucleation rate is a very sensitive function of the surface concentration of dissolved gas, $[H_2]_{surf}$. The rate of nucleus formation is expected to increase by many orders of magnitude over a small range of $[H_2]_{surf}$ thus making it difficult to examine this interesting region. Drifting potentials resulting from imperfect reference electrodes prohibits the fine control required over $[H_2]_{surf}$. Instead of voltage control to study nucleation, experimentally, constant current mode could be preferable. Currents can realistically be controlled within ten picoamperes allowing exquisite control over $[H_2]_{surf}$. This exacting control would allow accurate determination of nucleation rates by performing repeated experiments holding the surface concentration constant and measuring with high temporal precision how long on average it takes for a bubble to form.

5.2.3 Other phase transitions

The voltammetric techniques demonstrated in this dissertation for studying are likely not limited to dissolved gas to bubble phase transitions. Nucleation of droplets and solid crystals should also be feasible. An intriguing possibility would be the study of nucleation and steady-state systems for iodine crystals and bromine droplets.

5.3 References

(1) Personal communication

(2) Luo, L.; White, H. S. Electrogeneration of Single Nanobubbles at Sub-50-Nm-Radius Platinum Nanodisk Electrodes. *Langmuir* **2013**, *29*, 11169–11175.

(3) Epstein, P. S.; Plesset, M. S. On the Stability of Gas Bubbles in Liquid-Gas Solutions. *J Chem Phys* **1950**, *18*, 1505–1509.

(4) Zhang, X. H.; Quinn, A.; Ducker, W. A. Nanobubbles at the Interface Between Water and a Hydrophobic Solid. *Langmuir* **2008**, *24*, 4756–4764.

(5) Grogan, J. M.; Schneider, N. M.; Ross, F. M.; Bau, H. H. Bubble and Pattern Formation in Liquid Induced by an Electron Beam. *Nano Letters* **2014**, *14*, 359–364.